Dissertation Agreement

In presenting this thesis or dissertation as a partial fulfillment of the requirements for an advanced degree from Emory University, I hereby grant to Emory University and its agents the non-exclusive license to archive, make accessible, and display my thesis or dissertation in whole or in part in all forms of media, now and hereafter known, including display on the world wide web. I understand that I may select some access restrictions as part of the online submission of this thesis or dissertation. I retain all ownership rights to the copyright of the thesis or dissertation. I also retain the right to use future works (such as articles or books) all or part of this thesis or dissertation.

Signature:

_____ _____

Emily I. Bartle **Date**

The role of desmosome order, organization, and dynamics in adhesive function

By

Emily I. Bartle
Doctor of Philosophy

Graduate Division of Biological and Biomedical Sciences
Biochemistry, Cell, and Developmental Biology

_____

Alexa L. Mattheyses, Ph.D
Advisor

_____

Gary Bassell, Ph.D
Committee Member

_____

Andrew Kowalczyk, Ph.D
Committee Member

_____

Eric Ortlund, Ph.D
Committee Member

_____

Khalid Salaita, Ph.D
Committee Member

Accepted:

_____

Lisa A. Tedesco, Ph.D
Dean of the Graduate School

_____

Date

The role of desmosome order, organization, and dynamics in adhesive function

By

Emily I. Bartle
B.S., University of Richmond, 2012

Advisor: Alexa L. Mattheyses, Ph.D

An abstract for a dissertation submitted to the Faculty of the
James T. Laney School of Graduate Studies of Emory University
in partial fulfillment of the requirements for the degree of Doctor of Philosophy
Graduate Division of Biological and Biomedical Science Biochemistry, Cell and Developmental Biology

2019

Abstract

The role of desmosome order, organization, and dynamics in adhesive function

By: Emily I. Bartle

Macromolecular complexes are intricate structures that combine many different protein components to achieve a biological function. The relationship between complex architecture and function if often difficult to study because it requires bridging resolution scales between proteins, cells, and tissues. In the case of the cell-cell junction the desmosome, the complex is essential for adhering neighboring cells and maintaining tissue integrity in response to mechanical stress. Desmosomes can adopt two distinct adhesive states: calcium-dependent and calcium-independent adhesion, or hyperadhesion. Studying the relationship between desmosome organization and adhesive strength requires utilizing techniques with both molecular specificity and nanoscale resolution. To bridge this resolution gap, I utilized super-resolution microscopy to study the organization of the desmosome.

To investigate desmosomal plaque organization, I applied direct stochastic reconstruction microscopy (dSTORM) to determine the nanoscale structure of the desmosomal plaques. Desmosome architecture was altered in hyperadhesion induced by plakophilin-1 overexpression, which suggested a role for desmosome organization in determining adhesive strength. Another component of desmosome architecture is protein order, defined by a repeating array of proteins. I developed and applied fluorescence polarization microscopy (FPM) for measuring the order of the desmosomal cadherin desmoglein 3 (Dsg3) in living cells. While Dsg3 was ordered in calcium dependent desmosomes, inducing disassembly by removing exogenous calcium resulted in rapid disordering and suggested the importance of cadherin order for adhesion. Together these results suggested a role for the order and organization of desmosomes for controlling adhesive strength.

To further investigate this structure-function relationship, I measured the physical properties of desmosomes in both adhesive states. I induced hyperadhesion with a PKCα inhibitor, since the signaling mechanism for PKCα induced hyperadhesion has been previously characterized. Using dSTORM and FPM to measure order and organization in hyperadhesive desmosomes, I determined no difference in architecture between adhesive states. To explain the difference in functional states, I next investigated the role of protein dynamics. Desmosome proteins exhibited significantly decreased mobility in hyperadhesion, compared to calcium-dependent desmosomes. Ultimately, I concluded that loss of protein exchange is the mechanism of hyperadhesion. Together this dissertation highlights the roles of desmosome order, organization, and dynamics in controlling adhesive function.

The role of desmosome order, organization, and dynamics in adhesive function

By

Emily I. Bartle
B.S., University of Richmond, 2012

Advisor: Alexa L. Mattheyses, Ph.D

A dissertation submitted to the Faculty of the
James T. Laney School of Graduate Studies of Emory University
in partial fulfillment of the requirements for the degree of Doctor of Philosophy
Graduate Division of Biological and Biomedical Science Biochemistry, Cell and Developmental Biology

2019

Table of Contents

List of Tables and Figures

Chapter 1

Dissertation Overview

Macromolecular complexes are intricate arrangements of multiple proteins assembled for the purpose of achieving a biological function, such as protein trafficking, controlling cell division, distributing forces, or maintaining cell architecture. Cell-cell junctions are one type of macromolecular complex critical for cell adhesion, barrier formation, and cell communication. Of the cell junctions found in epithelial tissues, desmosomes contribute to cell adhesion and allow tissues to resist mechanical stress by integrating the intermediate filament cytoskeleton between neighboring cells. In Chapter 2 of this dissertation, the structure and function of the desmosome is reviewed. Each desmosome component including the transmembrane cadherins, intracellular plaque proteins, and keratin cytoskeleton are covered, as well as their contributions to the complex as a whole.

While macromolecular complex structure is important for function, the size and complexity of cell junctions makes this difficult to study. Using super-resolution microscopy modalities such as structured illumination microscopy (SIM), direct stochastic optical reconstruction microscopy (dSTORM), or fluorescence polarization microscopy (FPM) can overcome many of the challenges of studying desmosomes and other cell junctions. Chapter 3 provides an overview of several types of super-resolution microscopy and discusses the advantages that these methods can provide for studying cell junctions. Each method highlighted in this chapter provides nanoscale resolution with molecular specificity and has unique applications.

The power of single molecule localization microscopy is highlighted in Chapter 4, where dSTORM was used to measure the nanoscale organization of the desmosome. The ultrastructure of the desmosome has been characterized by electron microscopy (EM) and found to consist of linear plaques with mirror symmetry across the plasma membrane. Determining the distribution

of proteins within these plaques has been an ongoing challenge, since it requires molecular specificity at the nanoscale which is lacking in conventional EM. While immunogold EM achieves both of these requirements, it lacks the coverage provided by super-resolution fluorescence microscopy. I utilized dSTORM to determine the proteins components of the desmosome have both a specific localization and organization within the plaque. I further discovered that this organization is robust and conserved across several cell lines, primary human keratinocytes, and human skin sections. Altering desmosome adhesive strength by over-expressing the desmosome component plakophilin-1 resulted in a change in the desmosome plaque architecture, which suggested that desmosome organization may play an important role in adhesive function.

Another aspect of protein organization in macromolecular complexes is order, which is defined as the repeated array of individual protein components. Chapter 5 discusses the development and application of FPM to study the order of the desmosomal cadherin Desmoglein-3 (Dsg3). While cryo-electron tomography has previously demonstrated the cadherins fit within an ordered array in the extracellular space, these results are dependent upon fixed cells and cannot address the dynamics of order over time. To address this gap, we used FPM to demonstrate cadherins were ordered in living cells. I also disrupted desmosome adhesion and found that this resulted in a loss of Dsg3 order, indicating a role for order in desmosome function.

Together the dSTORM and FPM data suggested roles for order and organization in determining desmosome adhesive function. Therefore, I explored the changes in structure corresponding to increased adhesive strength (hyperadhesion). In Chapter 6, I investigated the physical properties of calcium-dependent and hyperadhesive desmosomes. In this work,

desmosomes were made hyperadhesive by inhibiting protein kinase C- alpha (PKCα). Interestingly, hyperadhesive desmosomes were capable of maintaining adhesion in the absence of order, as measured by FPM. This data indicated that order was not necessary for adhesion, contrary to what I had previously hypothesized. Using dSTORM, I also found that there was no difference in desmosome architecture between adhesive states. To determine the mechanism of hyperadhesion, I next examined changes in protein dynamics by fluorescence recovery after photobleaching (FRAP). I found that in a normal adhesive state, desmosomal proteins exhibit the ability to diffuse in and out of desmosomes. However, when desmosomes were converted to the hyperadhesive state, protein mobility was significantly reduced. I therefore concluded that protein mobility, not order or organization, is the mechanism through which desmosome adhesive state is controlled.

The goal of this dissertation was to develop and apply super-resolution imaging methods to test the hypothesis that the physical properties of the desmosome regulate adhesive function. A summary of this work can be found in Chapter 7, along with discussion of future work based on these results and the implications of these findings for the field of desmosome research. This work has determined the order and organization of normal desmosomes and established super-resolution microcopy as a powerful tool for studying desmosome architecture. This laid the groundwork for additional experiments where I determined the mechanism of desmosome hyperadhesion. In the future these approaches could be applied to both desmosomes and other cell junctions for studying changes in structure and function associated with disease, remodeling during wound healing, or junction assembly. Overall this work significantly impacts our understanding of desmosome structure and function.

Chapter 2

Introduction

2.1 Desmosome function

Desmosomes are cell-cell junctions responsible for maintaining adhesion in tissues that must sustain their structural integrity while being routinely exposed to mechanical stress (Kowalczyk and Green, 2013). Desmosomes provide necessary strength to these tissues and allow cohesive resistance to external forces, which is critical for healthy tissue homeostasis. However, tissues must also maintain plasticity and be able to alter cell adhesion to accommodate coordinated changes in cell number, cell position, or tissue-scale organization (Rubsam et al., 2018). Therefore, regulation of desmosome adhesion is critical in a number of biological processes including embryonic development, tissue differentiation, and wound healing (Garrod et al., 2005; Kimura et al., 2012; Rotzer et al., 2016).

Desmosomes are found in all epithelial tissues and some non-epithelial tissues like the myocardium. The epithelia is one of four types of tissues found in the body and functions to line and protect the other tissues (muscles, nerves, and connective tissue). While desmosomes are found in the simple epithelia of organs like the bladder, kidneys, and lungs, they are more commonly studied in the stratified epithelia of the skin (Holthofer et al., 2007). The skin is the first barrier separating our bodies from the outside world and must bear mechanical stress in order to function. The epidermis is commonly used for studying the desmosome, as keratinocyte cells from the basal epidermis are amenable to culturing, epidermal tissue is readily acquired, and desmosome function is highly important for skin organization and homeostasis.

While desmosomes in the mature epidermis are considered organized and stable structures, during embryonic development desmosomes must be plastic and adapt to accommodate tissue remodeling (Kimura et al., 2012). Furthermore, mature desmosomes must retain the ability to revert to a more plastic state to permit healing after tissue injury. Wound

healing assays in mouse tissue have shown that keratinocytes revert to a more basal phenotype, or weaker adhesive state, to promote cell migration and remodeling (Garrod et al., 2005; Owen et al., 2008). Following wound healing, failure to revert back to a stronger adhesive state results in chronic wound injuries where the skin remains fragile (Loschke et al., 2016). Therefore, desmosome adhesion must be rapidly and precisely tuned to balance tissue strength with plasticity.

2.1.1 Desmosome signaling

Aside from their adhesive function, desmosomes have a role as signaling platforms in the cell. Like other macromolecular complexes that have been shown to act as signaling "depots" (Ray et al., 2007), components of the desmosome can control cellular processes like gene transcription and cell proliferation independent of their role in the junction. Expression of some desmosomal components has been directly linked to activation of pathways like MAPK, Wnt, receptor tyrosine kinases, etc (Johnson et al., 2014a). Controlling the localization of desmosomal components has also been shown to determine adhesive strength and cell differentiation (Kowalczyk and Green, 2013). For instance, it has recently been discovered that DP localization to the nucleus increases cell migration and can aberrantly prevent cells from re-establishing a confluent monolayer following wounding (Wang et al., 2018). Cell proliferation, cell migration, and tissue stratification are all regulated by pathways known to crosstalk with desmosomal proteins, although in many cases direct interactions and effects remain to be elucidated. However, these signaling pathways are emerging targets for controlling desmosome function, especially as adhesion relates to disease states.

2.1.2 Desmosomes in disease

Loss of desmosome adhesion, changes in desmosome plasticity, and subsequent changes in signaling are all associated with human disease states (Broussard et al., 2015; Johnson et al., 2014a; Najor, 2018). The pathologies of desmosome-dependent diseases most commonly present in the skin and heart, though desmosome dysregulation has also been linked to cancers throughout the body.

In the epidermis, disruption of desmosome structure and downregulation of desmosomal proteins often leads to skin fragility and blistering. For instance, Pemphigus vulgaris (PV) is an acquired immunological condition where the body produces auto-antibodies to desmosomal proteins, such as the cadherin desmoglein 3 (Dsg3) (Amagai et al., 1991; Spindler and Waschke, 2018). This results in skin fragility in the basal layer of the epidermis, which causes blistering when the skin experiences mechanical stress. PV can also result in painful lesions of the oral mucosa (Feller et al., 2017). Other skin blistering diseases include pemphigus foliaceus (PF) which is similar to PV but typically targets Dsg1, rather than Dsg3.

Other desmosome-related skin diseases are caused by genetic abnormalities, such as palmoplantar keratoderma (PPK), which is characterized by a thickening and a sloughing off of skin on the palms and soles of the feet (Ishida-Yamamoto et al., 2017). PPK varies in clinical presentation and can result from mutations in either Dsg1, desmoplakin, or keratin 1 that cause a disruption of desmosome adhesion (Whittock et al., 2002). PPK can also occur secondary to other conditions, such as Naxos and Carvajal syndromes that are genetic diseases characterized by comorbidity of cardiomyopathy, wooly hair, and PPK. Naxos has been linked to a truncation of plakoglobin (McKoy et al., 2000), while Carvajal results from truncation of desmoplakin that eliminates the keratin binding domain (Norgett et al., 2000). Another disease, severe dermatitis,

multiple allergies, and metabolic wasting (SAM) syndrome is very rare, but is one of the most severe desmosome-related skin diseases (McAleer et al., 2015). SAM has been linked to defects in Dsg1, as well as desmoplakin (Lewis et al., 2018; McAleer et al., 2015; Samuelov et al., 2013). Among other symptoms, patients with SAM present with a skin barrier defect that commonly leads to systemic infections and sepsis. Treatment options vary between these diseases, but typically involve symptom management such as the use of topical or systemic steroids (Celentano and Cirillo, 2017; Kitajima, 2014; Najor, 2018).

In desmosome diseases of the heart, mutation or truncation of desmosomal proteins has been found to be causative of arrhythmogenic cardiomyopathy (AC) (Basso et al., 2012; Calore et al., 2015; Paul et al., 2012; Rampazzo et al., 2014; Rickelt and Pieperhoff, 2012). Roughly half of AC cases studied could be attributed to mutations in desmosomal proteins, primarily in plakophilin-2 (Pkp-2) (den Haan et al., 2009). AC can be further sub-classified by symptoms, but the defining characteristics of the disease now includes a wide spectrum of genetic and clinical presentations, with as many as 1 in 2000 people affected (Basso et al., 2012; Peters et al., 2004). Patients are at a higher than normal risk for sudden cardiac death, even when asymptomatic, and progression of the disease often leads to heart failure (Calore et al., 2015). Treatment remains limited to symptom management and avoiding cardiac stressors, including caffeine, strenuous exercise, and alcohol (Basso et al., 2012).

The precise role of desmosomes in AC has yet to be elucidated, in part because desmosomes in cardiac tissue are incorporated into complex multi-junction structures called the intercalated disc, which integrates desmosomes with adherens and gap junctions. Recent work found that desmosome dysfunction caused AC by impairing gap junctions and their electrical conduction in the heart (Agullo-Pascual et al., 2014c; Agullo-Pascual et al., 2013a). Other work

implicated adhesive function, when they showed that loss of Dsg2 adhesion can cause AC (Kant et al., 2015a; Schlipp et al., 2014) Interestingly, increased adhesive strength was also recently found to be pathogenic, when a Dsg2 point mutation that exhibited increased trans-binding was identified in a patient with AC (Dieding et al., 2017). The effects of desmosome diseases on cell adhesion are often conflicting or unclear, with no single pathological mechanism.

An active area of research is the role of desmosomes in cancer tumorigenesis and metastasis (Broussard et al., 2015; Dusek and Attardi, 2011). The role of desmosomes in cancer is complex and paradoxical. The most obvious correlation between desmosomes and cancer is that loss of adhesion promotes cell migration and cell migration is integral to cancer progression (Chidgey and Dawson, 2007; Moh and Shen, 2009). However, our technical limitations make it difficult to associate *in vivo* changes in adhesive function with tumorigenesis. Instead, changes in desmosomal protein expression levels have been correlated with disease severity and prognosis. Downregulation of desmosome proteins is associated with some types of cancer, such as those of the bladder (Alroy et al., 1981), stomach (Demirag et al., 2011), prostate (Breuninger et al., 2010), and hormone-linked cancers like cervical (Alazawi et al., 2003) and endometrial cancer (Nei et al., 1996). However in other cases, overexpression of desmosomal proteins correlates with poor patient outcomes, such as in skin, head, and neck cancers (Brennan and Mahoney, 2009; Chen et al., 2007; Kurzen et al., 2003). The variability in protein expression between cancers indicates a complex role for desmosomes in cancer that requires further study.

Attempts to determine the effects of desmosomal protein overexpression or knockdown on cancer progression in both mice and cell culture models have yielded mixed results (Dusek and Attardi, 2011). Overexpression of some desmosomal components resulted in pro-oncogenic phenotypes including inhibited apoptosis, enhanced cell proliferation, and increased cell invasion

(Furukawa et al., 2005; Hakimelahi et al., 2000). For example, Dsg2 promoted tumor development when overexpressed in mouse epidermis (Brennan et al., 2007). In contrast, overexpressing plakoglobin and the desmosomal cadherins in some cancer cell lines suppressed tumor invasion (De Bruin et al., 1999; Rieger-Christ et al., 2005; Simcha et al., 1996; Tselepis et al., 1998). Knock-down of Pkp-2 decreased oncogenic potential by mediating EGFR signaling (Arimoto et al., 2014). The variable effects of up- or down-regulating desmosome components mirrors the effects seen in tumors, when desmosome components are measured as prognostic markers. The consensus remains that desmosomes play a critical role in determining cancer progression.

In addition to the loss of cell adhesion, the signaling role of desmosomal proteins in cancer should not be minimized. For instance, overexpression of plakoglobin has been shown to suppress tumor invasion in cell culture (Rieger-Christ et al., 2005). However, it has also been shown to stimulate the transcriptional regulation of WNT target genes, which has a pro-oncogenic effect (Chidgey and Dawson, 2007; Li et al., 2007). As another example, mislocalization of plakophilins from the cell membrane to the nucleus has been shown to activate pro-oncogenic gene transcription (Chen et al., 2002; Sobolik-Delmaire et al., 2010).

As another layer of complexity, it has also been suggested that the oncogenic effects of loss of desmosomes could be due to the increased fragility of epithelial tissues. Increased fragility could in turn increase susceptibility to cell invasion (Dusek and Attardi, 2011). This also leads to the hypothesis that patients with other desmosome-related diseases would exhibit an increased incidence of epithelial cancers. However, the relative rarity of desmosome diseases involving tissue fragility and the high lethality of these diseases at a young age means there is insufficient literature to support or deny such a comorbidity.

Whether it affects the skin, heart, or other epithelial tissues, desmosome-related diseases are often difficult to treat. The relationship between protein expression, adhesion, and desmosome signaling is highly nuanced and difficult to parse. Studying and treating these diseases is challenging, in part because we do not fully understand the complexities of desmosome adhesive function.

2.1.3 Calcium dependence of adhesive function

To reproducibly study desmosome function, it was important that the field define differences in adhesion consistently. Desmosome adhesive state is now often classified as either calcium-dependent or calcium-independent, also known as "hyperadhesive" (Garrod, 2010; Garrod et al., 2005; Wallis et al., 2000). Calcium-dependent desmosomes represent the population with weaker adhesion, like those found in early development, wound-edges, and in cell culture models. These desmosomes are defined as calcium-dependent because they lose adhesion in response to chelation of calcium from the media. In contrast, calcium-independent desmosomes, like those in mature epidermal tissue, maintain robust adhesion and can resist mechanical agitation in the absence of calcium for an extended period of time (Kimura et al., 2007).

Desmosome adhesive state has been defined by an *in vitro* assay and is dependent upon removal of calcium from the cell media, which makes it difficult to assess adhesive strength *in vivo*. Traditionally, adhesive function has been assessed by a dispase fragmentation assay (Hudson et al., 2004). In this assay confluent cell sheets are mechanically perturbed, and the resulting number of cell sheet fragments is inversely proportional to adhesive strength. Dispase assays used for confirming hyperadhesion are performed after at least 90 minutes in calcium chelated media. The drawbacks to this assay are numerous; most notably, it measures adhesive

strength as an aggregate of many cells, while adhesive strength can vary from cell-to-cell or even, potentially, from desmosome to desmosome. Additionally, it is typically a terminal measurement, so the cells cannot easily be further studied once adhesive strength has been verified. These challenges in measuring adhesive strength indicate the need for better metrics to differentiate between calcium-dependent and hyperadhesive desmosomes.

To develop new methods for measuring adhesive strength, the differences between adhesive states must be better understood. Studying hyperadhesion often involves inducing calcium-independence in cell culture models that would otherwise be calcium-dependent. This can be done in several ways. Allowing cells to reach confluency and continue growing for >6 days, over-expression of plakophilin 1 (Pkp-1), and inhibition of the PKCα signaling pathway all result in calcium-independent desmosomes (Garrod et al., 2005; Tucker et al., 2014). Though Pkp-1 overexpression results in an ~8-fold increase in Pkp-1, the other mechanisms of inducing hyperadhesion involve no significant change in desmosomal protein expression (Kimura et al., 2007). This result indicated that hyperadhesion is acquired through a change in architecture or signaling, not through altered desmosome composition.

Because of its biological significance, work has been done to investigate the structural differences between calcium-dependent and calcium-independent adhesion. Electron microscopy experiments determined that hyperadhesive desmosomes contain a dense midline that is absent in calcium-dependent desmosomes (Garrod et al., 2005). The dense midline has been attributed to the order of the desmosomal cadherins where they undergo trans-binding in the extracellular space (Al-Amoudi et al., 2007). The structural differences between calcium-dependent and hyperadhesive desmosomes by EM are not a high through-put metric for determining adhesive strength and it remains difficult to assess the adhesive strength of desmosomes *in vivo*.

While the distinction between calcium-dependence and hyperadhesion has proven useful, we do not understand the physical changes that occur between adhesive states. This knowledge gap is addressed in-depth in Chapter 6. Determining the nanoscale differences between desmosome adhesive states will allow us to understand the mechanism of hyperadhesion and more precisely regulate desmosome function.

2.2 Desmosome structure

Desmosomes are complex macromolecular structures combining many protein components that are integrated between multiple cells to form a cohesive tissue. Each component of the desmosome acts as a link in the chain and, while their functions are unique, each is of equal importance. Desmosomal proteins will first be discussed individually, before I address how they integrate into the complex. Finally, I conclude this section with the context of how desmosome structure has been investigated previously and how those studies inform adhesive function.

2.2.1 Cadherins

At the adhesive core of the desmosome are the cadherins. These type I single pass transmembrane proteins are similar in structure and function to the classical cadherins, like E-cadherin found in adherens junctions (Harrison et al., 2016). They are composed of five extracellular cadherin domains interspaced with calcium-binding linker regions, a transmembrane domain, and an intracellular tail that interacts with the desmosomal plaque proteins (Fig. 1A). Desmosomal cadherins are composed of two subtypes of cadherins: the desmogleins and the desmocollins. With four members of the desmoglein family (Dsg1-4) and three members of the desmocollin family (Dsc1-3), each protein has a unique sequence,

expression pattern, and function (Delva et al., 2009). However, many of their structural features and the overall function of cell adhesion remain constant.

In the extracellular region, all desmosomal cadherins undergo trans-binding between neighboring cells. A tryptophan residue (W2) in the first extracellular domain (EC1) forms a strand swap with another cadherin through insertion of the W2 into a hydrophobic pocket of the opposing EC1 domain (Haussinger et al., 2004; Overduin et al., 1995; Shapiro et al., 1995). Unlike in classical cadherins, it is unknown if the desmosomal cadherins are capable of forming *cis* interactions with cadherins in the same cell. Some research indirectly supports a role for desmosomal cadherin *cis* binding (Harrison et al., 2016; Lowndes et al., 2014; Shafraz et al., 2018), though structural analysis by cryo-EM has indicated that the cadherins are too far apart to form such a bond (Tariq et al., 2015). This result assumes that the static cryo-EM structure represents the predominant organization and dismisses the potential for transient *cis* interactions that cannot be captured by this method.

The assumption that the extracellular space is static is in part due to the structure of the cadherins themselves. Each cadherin has a rigid tertiary structure that is conveyed by 2 or 3 calcium ions binding in the calcium-binding linker regions between the extracellular domains (Harrison et al., 2016; Sotomayor and Schulten, 2008). Interestingly, recent work has identified that the desmosomal cadherins are in fact more flexible than their classical counterparts (Tariq et al., 2015). This flexibility may in part account for desmosomes increased adhesive strength and ability to resist mechanical stress, compared to adherens junctions.

Inside the cell, the cadherin tail is where the structure of the desmogleins and desmocollins display significant differences (Fig. 1A) (Delva et al., 2009; Garrod and Chidgey, 2008). Immediately adjacent to the transmembrane domain is a conserved intracellular anchor

(IA) domain. Desmocollins have an alternative splice variation where the IA can be followed by an intracellular cadherin- like sequence (ICS) in the “a” isoform, or a truncated version of the domain in the “b” isoform. By comparison, the desmogleins have significantly larger intracellular tails which include a proline-rich linker region (IPL) following the ICS, as well as a repeat unit domain (RUD) and a desmoglein terminal domain (DTD) (Koch et al., 1990). These domains have been minimally studied and not much is known about their structure or function.

Aside from these structural differences, another distinguishing feature between the desmogleins and desmocollins is the expression pattern and localization of the isoforms (Fig. 1B) (Holthofer et al., 2007). Both Dsg2 and Dsc2 are ubiquitously expressed in all desmosome-bearing tissues. In contrast, Dsg3 is found primarily localized to the basal layers of the epidermis, while Dsg1 expression is enriched in the upper layers of the skin. Dsg4 and Dsc1 are expressed in the granular layer of the skin, while Dsc2 and Dsc3 are found in the basal and spinous layers of the epidermis. Because of this macro organization by isotype, the different cadherins are thought to have unique functions. For instance, Dsg2 is generally considered pro-proliferation while Dsg1 is pro-differentiation due to their expression patterns. However, the relationship between expression pattern and function has proven to be more complex. Cancer research has explored these correlations to exploit potential anti-proliferative, anti-tumorigenic effects with mixed results.

One complicating factor in analyzing the function of individual desmoglein or desmocollin isoforms in cells or tissue is interpreting the importance of the individual as opposed to the ratio of cadherin isotypes. Altering the ratio of cadherins may result in aberrant signaling or defects in adhesion, particularly if the hypothesis holds true that heterophilic binding is the predominant type of transbinding. Much research has been done to explore the homophilic

versus heterophilic binding interactions that can occur between cadherin isotypes, resulting in conflicting answers. Heterophilic interactions have been confirmed and have a functional role in mediating desmosome formation (Green and Simpson, 2007; Thomason et al., 2010). However, the evidence regarding homophilic interactions is mixed. A bead aggregation assay supports Dsg-Dsc heterophilic binding, but did not identify any homophilic Dsg-Dsg or Dsc-Dsc binding (Harrison et al., 2016). In contrast, single molecule AFM and protein cross-linking has shown Dsg1-Dsg1, Dsg2-Dsg2, Dsg3-Dsg3, and Dsc3-Dsc3 homophilic binding (Heupel et al., 2008; Nie et al., 2011; Spindler et al., 2009; Syed et al., 2002; Vielmuth et al., 2015).

Though the desmogleins and desmocollins have unique features, their function of adhering neighboring cells through extracellular interactions is conserved. For this binding to result in a functional desmosome, the intracellular tail of the cadherins is then bound by the desmosomal plaque proteins, which will be discussed in the following section.

2.2.2 Plaque proteins

The desmosomal plaque proteins fall under two main classes, the armadillo family proteins (plakoglobin and plakophilins) and the plakins (desmoplakin) (Fig. 1A). Together the plaque proteins integrate the cadherin intracellular tail with the keratin intermediate filament cytoskeleton to convey mechanical integrity. Both plakoglobin (PG) and the plakophilins (Pkp1-3) interact directly with the cadherin tail, while desmoplakin (DP) strongly associates with both plakoglobin and Pkps through its N-terminal domain (Al-Amoudi et al., 2011). The C-terminal domain of DP contains the keratin binding region, which completes the chain of interactions linking the cytoskeletons of neighboring cells. The structure and function of each of these proteins will be explored in more detail next.

PG is composed of an N-terminal globular domain, a central core composed of 12 armadillo repeats, and a C-terminal tail (Kowalczyk and Green, 2013). Of the armadillo family, PG has a unique role because it is capable of interacting with both E-cadherin and the desmosomal cadherins, although it has a much higher affinity for the desmosome (Chitaev et al., 1996). The armadillo repeat domain of PG has been crystalized with the tail of E-cadherin (Choi et al., 2009). This structure indicates the likely interface for PG-desmosomal cadherin binding as well, given the similarities of the PG binding domains across cadherins. Mutations in PG are associated with both heart defects and skin fragility, indicating the importance of PG for adhesive function (Broussard et al., 2015).

The Pkp family of proteins are also armadillo family proteins associated with the desmosome. Pkps contain 9 armadillo repeats, surrounded by N- and C-terminal globular domains (Kowalczyk and Green, 2013). Unlike PG, the Pkps contain an extra region inserted in the middle of the armadillo repeats introducing a bend in the structure. Both Pkp1 and Pkp2 have two splice variants, a shorter “a” form and a slightly longer “b” form. Functionally, Pkps are well known to act as protein scaffolds (Bass-Zubek et al., 2009). In desmosomes, Pkps bind to both the cadherin tails and desmoplakin, as well as containing an essential palmitoylation motif that inserts into the plasma membrane (Roberts et al., 2014). Interestingly, all of the identified binding partners for Pkps thus far interact with the N-terminal globular domain and not the armadillo repeats (Bass-Zubek et al., 2009).

Like the cadherins, the different isotypes of the Pkps are differentially expressed based on tissue type (Delva et al., 2009). Pkp-1 is localized primarily to the suprabasal layers of the skin, while Pkp-2 can be found in the basal layers of the skin, as well as in simple epithelia and non-epithelial tissues. Pkp-3 has uniform expression in the epidermis and is also found in simple

epithelia. The isoforms have distinct functions, with Pkp-2 specifically identified as a key component of early desmosome assembly. Specifically, Pkp-2 acts as a recruitment site for PKCα suggesting a role for Pkp-2 in modulating adhesive strength (Bass-Zubek et al., 2008; Godsel et al., 2005). Overexpression of Pkp-1 has been shown to result in hyperadhesion while also increasing desmosome length significantly (Stahley et al., 2016a). This morphological and functional change is consistent with the size and function of desmosomes in the upper stratified epithelia where Pkp-1 is endogenously expressed. Taken together with the numerous diseases resulting from Pkp mutation or deletion, the importance of Pkps for desmosome function is evident.

The final plaque protein DP acts as a critical linker between the armadillo plaque proteins and the keratin intermediate filament cytoskeleton. DP is composed of a globular N-terminal domain that binds the armadillo proteins, a coiled-coil α-helical rod domain, and a C-terminal globular domain that binds to keratin (Choi et al., 2002; Kouklis et al., 1994). There are two isoforms of DP; the I isoform is the full-length protein, while the II isoform is a shorter version that is missing ~two-thirds of the rod domain, due to an alternative splicing variant.

A key residue of DP, S2849, has been implicated in regulating desmosome adhesive strength (Hobbs and Green, 2012). Phosphorylation at this serine residue by PKCα resulted in a decreased affinity of DP for keratin. Preventing phosphorylation chemically or through mutation of serine to glycine was found to increase adhesive strength (Hobbs and Green, 2012). Further work was done to elucidate the downstream signaling impacts following S2849 phosphorylation. The Green lab determined that S2849 acts as an initiator for GSK-3 and PRMT-1 to further phosphorylate and methylate DP, leading to greater impacts on the DP-keratin association (Albrecht et al., 2015).

DP is a crucial linker in desmosomes, as evidenced by the numerous skin and heart diseases resulting from DP mutations. Arrhythmogenic cardiomyopathies are often the result of DP mutations (Schiavon et al., 2011). Skin diseases resulting from mutation or truncation of DP include PPK and acantholytic epidermolysis bullosa, both of which present with aberrant skin thickening and skin fragility. Furthermore, DP-null mouse models show early embryonic lethality, in part due to a failure for cells to proliferate as normal. Recent work has implicated a mislocalization of DP to the nucleus in promoting aberrant cell proliferation (Wang et al., 2018). This highlights a role for DP in tissue morphogenesis and embryonic development, as well as in cell-cell adhesion.

2.2.3 Keratin

Keratins form a rigid cytoskeleton in epithelial cells that distributes force throughout the cell, allowing it to resist mechanical stress (Windoffer et al., 2011). Keratin fibers are formed by co-polymerization of type I (acidic) and type II (neutral/basic) keratins (Cooper, 2000). Individual keratins form dimers, where the central rod domains coil around each other, that then assemble in an anti-parallel fashion to form tetramers. Tetramers then assemble to form protofilaments, which are the building blocks for the final rope-like keratin fiber.

Epithelial cells can express upwards of ten different types of keratins at any given time, though they have been found to be highly correlated with differentiation programming. For instance, basal keratinocytes in the epidermis typically express the keratin pair K5/K14 (Homberg and Magin, 2014). As basal cells differentiate in the stratified epithelia, K5/K14 converts to predominantly K1/K10. Other keratins important in the epidermis include K6, K16, and K17, which are expressed following injury or wounding at the expense of K1/K10. Because of the challenges in studying the structure and function of the cytoskeleton, the role of keratins in

desmosome adhesion has often been over looked. However, recent literature has begun elucidating the interplay between keratin isotype and adhesive strength. For instance, over-expression of K6 results in a hyper-migratory phenotype that inhibits formation of a mechanically robust cell sheet (Wang et al., 2018). Additional work has been conducted studying desmosome adhesion in keratin-null cells, which resulted in decreased adhesive strength in a signaling dependent manner (Vielmuth et al., 2018).

2.2.4 Complex organization

Integrating all of the described protein components together, desmosomes form a 300-500 nm disk-like structure on the plasma membrane. Both the size and molecular complexity of desmosomes make them challenging to study. Two distinct approaches have primarily been used to study the desmosome—biochemical assays and microscopy. The desmosome was first observed microscopically in the late 1800s by Giulio Bizzozero, which led to them being termed "nodes of Bizzozero". In the 1920s, they were renamed by Josef Schaffer (Delva et al., 2009), when he coined the term desmosome based on the Greek "desmo", which means bond or fastening, and "soma" which means body (Calkins and Setzer, 2007).

Early biochemical approaches led to the discovery that desmosome isolations were enriched with sphingolipids and cholesterol (Skerrow and Matoltsy, 1974). In later years, lipid rafts were discovered (Simons and Ikonen, 1997) and desmosomes were subsequently found to integrate into these microdomains, which clarified the cause of this enrichment. Furthermore, it was determined that the extent of the lipid raft integration is a distinguishing difference between adherens junctions and desmosomes (Resnik et al., 2011; Yap et al., 2015). In the 1980s, individual components of the desmosome were determined by biochemical means. Western blot analysis was used to identify the desmogleins and desmocollins, as well as the plaque proteins

(Cowin and Garrod, 1983; Cowin et al., 1986; Cowin et al., 1984; Gorbsky and Steinberg, 1981; Koulu et al., 1984). Biochemical approaches for separating and identifying desmosome components were, and remain, a key aspect to studying desmosome composition. However, these methods are dependent on studying cell lysates and lack the cellular localization information that can be accessed by microscopy. Thus, much of the ultrastructural information we know about desmosomes has come from microscopy approaches.

2.2.5 Desmosome organization by electron microscopy

Advances in our understanding of desmosome ultrastructure are often predicated on an advancement in imaging capabilities. For instance, electron microscopy revolutionized our view of the desmosome in the 1950s and 1960s, when Porter, Odland, and Kelly made their observations. They identified three distinct morphological features of the desmosome (Kelly, 1966; Odland, 1958; Porter, 1956). The extracellular core, now known to contain the desmogleins and desmocollins; the outer dense plaque, corresponding to the cadherin tail, PG, Pkps and the N-terminal domain of DP; and the inner dense plaque, corresponding to the C-terminal domain of DP and its association with keratin, can all be identified by EM densities (Fig. 2). EM also led to the identification of the dense midline as a structural characteristic distinguishing hyperadhesive desmosomes from their calcium-dependent counterparts. Early lanthanum-fill EM showed a highly ordered array in the extracellular adhesive interface (Rayns et al., 1969). Taken together, these EM structures suggested that the dense midline was likely due to the overlapping domains of a highly ordered array of cadherins in the extracellular space.

In the late 1990s, application of immune-gold labelling EM led to the first mapping of the desmosome ultrastructure with protein specificity by North et al, (North et al., 1999b). Immuno-gold EM pairs the molecular specificity of antibody labeling with the nanoscale resolution of EM

(Sirerol-Piquer et al., 2012). However, due to the process of labeling with nm-scale gold particles, immunogold EM lacks the coverage afforded by fluorescence microscopy, where each protein can be labeled with a fluorophore. Subsequent technical advancement of cryo-EM tomography further illuminated the architecture of the desmosome. By rapidly freezing the sample, morphology is better preserved than by conventional EM fixation techniques and can be measured at near-angstrom resolution (Irobalieva et al., 2016). The ultrastructure of both the extracellular region and the plaque domains of the desmosome have been characterized by cryo-EM (Al-Amoudi et al., 2011; Al-Amoudi et al., 2007; Al-Amoudi et al., 2005; He et al., 2003). These techniques have provided critical insight into the desmosome structure and organization, but unilaterally lack the ability to study the dynamic processes of desmosomes in living cells.

2.2.6 Desmosome organization by fluorescence microscopy

In addition to electron microscopy, desmosomes have been studied by fluorescence microscopy. An advantage provided by fluorescence microscopy is the ability to study desmosomes in live cells and observe changes in localization, morphology, and organization over time. Though desmosomes appear as diffraction limited puncta along the plasma membrane by widefield microscopy, these methods have still provided significant insight into desmosome biology.

For example, the process of desmosome assembly has been extensively studied using fluorescence microscopy. By manipulating the calcium dependence of cells in culture, desmosome assembly can be synchronized by switching cells from a low calcium media (≤0.03 mM) into media containing >1.5 mM calcium (Wilson, 2014). Fluorescently tagging desmosomal proteins allows the assembly process to be monitored in real time. Thus, the time it takes for assembly to occur, the order in which the desmosomal components arrive at the

membrane, and which components traffic together were all determined by fluorescent imaging (Godsel et al., 2005; Lowndes et al., 2014; Yin et al., 2005; Yin and Green, 2004). Another part of the assembly process that has been studied by fluorescence microscopy is the segregation of desmosomes into lipid rafts. Early on during the process of assembly, adherens junction and desmosomal components can be seen as colocalized puncta at the cell membrane (Lowndes et al., 2014; Nekrasova and Green, 2013; Stahley et al., 2014). As desmosomes mature, E-cadherin becomes segregated out from the desmosomal components resulting in a distinct pattern of alternating punctate structures. The mechanism of segregation is not known, but the enrichment of desmosomal proteins and exclusion of E-cadherin in raft isolation assays suggests a role for lipid raft association during this process.

Another dynamic process studied by fluorescence microscopy is the desmosome response to wounding in the epidermis (Beaudry et al., 2010). Wound healing is a dynamically regulated process that requires remodeling of desmosomes to allow cell migration followed by re-establishment of mechanically-resistant structures. Some components of this process, such as the keratin isotype switch (Homberg and Magin, 2014) and the reversion from hyperadhesive to calcium-dependent adhesion (Garrod et al., 2005) have been determined, but much remains to be studied.

The nanoscale densities conveyed by EM and the micron-scale molecular features visualized by widefield fluorescence microscopy have proven informative for understanding desmosome structure and adhesive function. However, we must ultimately study the desmosome with both nanoscale precision and molecular specificity, which conventional approaches lack. Applying super-resolution microscopy methods, such as single molecule localization microscopy and fluorescence polarization microscopy, bridge the gap to discern nanoscale desmosome

architecture *in vivo*. Only through super-resolution techniques can we capture the structural and dynamic relationships between protein, macromolecular complex, and cell scale information.

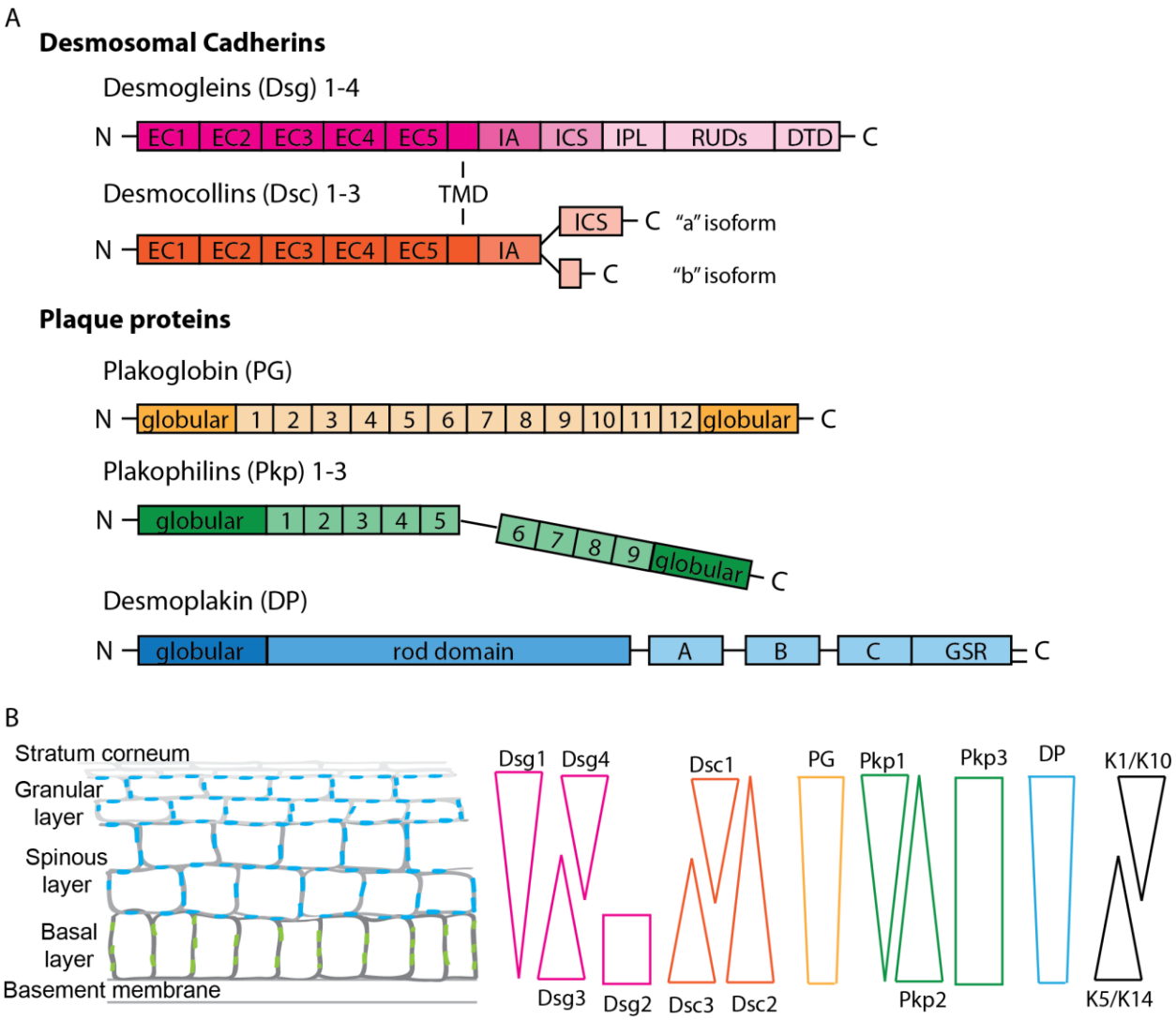

Figure 1. Structure and expression patterns of desmosomal protein components. (A) Desmosomal cadherins (desmogleins and desmocollins) are composed of five extracellular (EC) domains, a transmembrane domain (TMD), and an intracellular anchor (IA). The desmogleins contain a longer intracellular tail, including an intracellular cadherin-like sequence (ICS), an intracellular proline-rich linker (IPL), a variable repeat unit domain (RUD), and a desmoglein terminal domain (DTD). The desmocollins have shorter intracellular tails, with the "a" isoform ending after the ICS domain while the "b" isoform truncates with a partial ICS domain. Plaque protein plakoglobin (PG) contains globular N- and C-terminal domains with 12 armadillo

domain repeats. The plakophilins (Pkp) have a similar structure, but with just 9 armadillo repeats. Pkps have an extra linker domain between the fifth and sixth armadillo repeats, creating a kink in the structure. Desmoplakin (DP) is composed of a globular N-terminal domain, a coiled-coil rod domain, 3 spectrin repeat domains (A-C) and a glysine/serine rich C-terminal tail. (B) Each of the desmosomal protein components has a unique expression profile within the epidermis. The deepest layer of the epidermis is the basal layer of cells that attach to the basement membrane, where desmosomes are newly formed. Dsg3, Dsg2, Dsc2, Dsc3, Pkp2 and the K5/K14 keratins are all localized to this layer. The upper layers of the epidermis include the spinous and granular layers, which are enriched for Dsg1, Dsg4, Dsc1, Pkp1 and the K1/K10 keratins. PG, Pkp3, and DP are all relatively uniformly expressed throughout the layers of the epidermis.

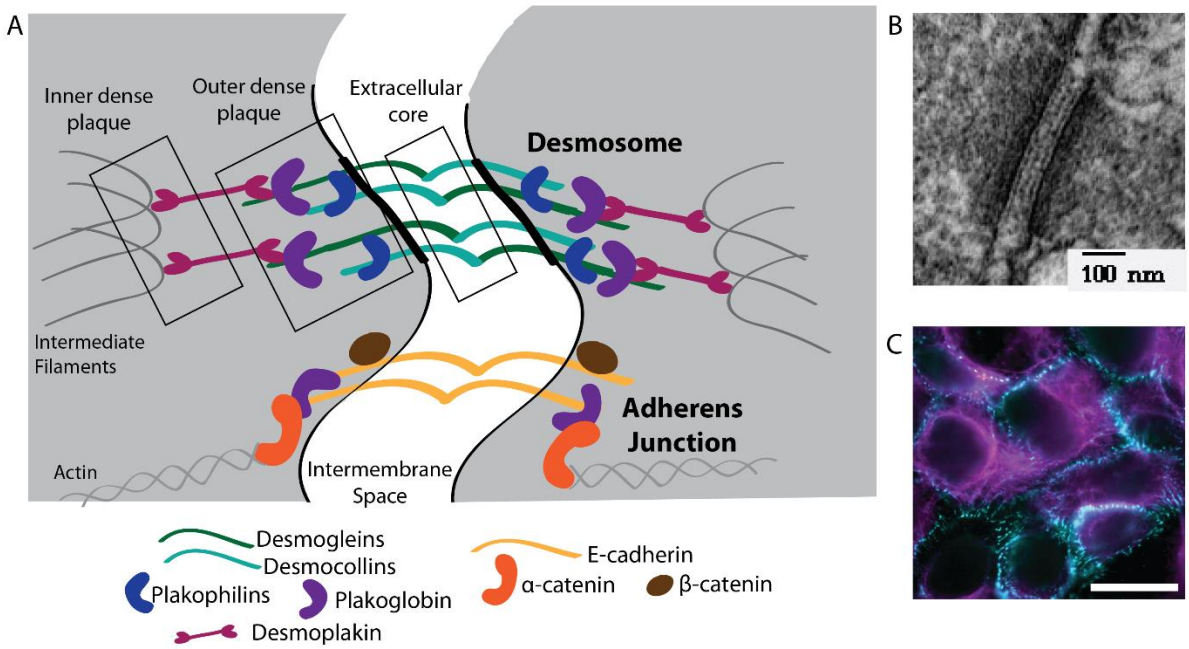

Figure 2. Macromolecular architecture of adhesive cell junctions. (A) Desmosomes are responsible for linking neighboring cells across the intermembrane space to allow tissues to resist mechanical stress. Structurally, they are composed of three distinct regions: the extracellular core, the outer dense plaque, and the inner dense plaque, as identified by EM densities. The extracellular core corresponds to the cadherin binding region in the intermembrane space. Plakoglobin, plakophilins and the N-terminal domain of desmoplakin interact in the outer dense plaque. Unlike adherens junctions that integrate with the actin cytoskeleton, the inner dense plaque corresponds to the location where the C-terminal tail of desmoplakin associates with the intermediate filament cytoskeleton. Additionally, desmosomes have been shown to localize to lipid raft membrane domains, which corresponds to a slightly wider plasma membrane compared to adherens junctions or the surrounding area. (B) Electron micrograph of a desmosome in epithelial tissue. Image licensed for public use. Scale bar= 100 nm. (C) Widefield fluorescence image of HaCaT cells stained for keratin (magenta) and desmoplakin (cyan). Scale bar= 25 μm.

Chapter 3

Super-resolution and advanced imaging of epithelial junctions

This chapter adapted from:

Bartle E.I., T.C. Rao, T.M. Urner, and A.L. Mattheyses. 2018. Bridging the gap: Super resolution microscopy of epithelial cell junctions. *Tissue Barriers*. 6:e1404189.

3.1 Introduction

Cell junctions are complex macromolecular structures with critical roles in many diverse processes including embryonic development, immune function, and wound healing. Epithelial tissues can have several types of cell junctions including tight junctions, adherens junctions, desmosomes, and gap junctions on the lateral membrane physically linking neighboring cells and hemidesmosomes on the basal membrane interacting with the extracellular matrix (Fig. 3). Each of these junctions have highly specialized structures and cellular organization specific to their unique roles in signaling and adhesion (Rübsam et al., 2017), mechanobiology (Xia and Kanchanawong, 2017), and barrier formation (Yano et al., 2017), to name a few. Investigating the structure/function of cell junctions is challenging due to their membrane localization, molecular complexity, and size, which ranges from ~10 nm (gap junctions) to ~500 nm (desmosomes) (Maeda et al., 2009; Tamarin and Sreebny, 1963).

Fluorescence microscopy is a critical tool in the study of cell junctions. The relatively straightforward sample preparation, ease of use, availability, and compatibility with live cell imaging distinguishes fluorescence microscopy. A central feature of fluorescence microscopy is the ability to specifically label and image proteins of interest, providing molecular specificity. Consequently, the spatial organization and dynamics of subcellular assemblies, proteins, or genomic sequence of interest in fixed or living samples can be determined using highly specific fluorescent labeling techniques such as immunocytochemistry, in situ hybridization, or chimeric fluorescent protein tags. However, a major limitation of conventional fluorescence microscopy for studying junction organization is the resolution limit. Resolution defines the smallest distance between two objects at which they can be individually identified. Based on relations defined by Abbe and Rayleigh, the resolution of a conventional widefield or confocal

microscope is limited to approximately 250 nm in the *x*-*y* imaging plane and 600 nm in the axial, or *z* dimension (Abbe, 1882; Rayleigh, 1879). Practically, this means a single protein with a physical size of 3 nm^3 will appear as a 250 x 250 x 600 nm diffraction limited spot in *x*-*y*-*z* when imaged by fluorescence microscopy. A consequence of the resolution limit is that proteins can appear co-localized when in reality their organization is distinct. The sizes of epithelial junctions are close to or below the resolution limit, restricting the utility of conventional widefield or confocal fluorescence microscopy.

Many junctional protein interactions and modifications have been investigated biochemically. While these methods provide molecular specificity, they do not reveal cellular or tissue localizations, and involve loss of population heterogeneity. To access structural information unavailable through biochemical studies, immunogold and tomographic electron microscopy (EM) have been used to study junctions (Al-Amoudi et al., 2011; Al-Amoudi et al., 2004; North et al., 1999a). An advantage of EM is high nanometer scale resolution, however it comes with a tradeoff of limited molecular specificity and requirement of sample fixation. Further, the sample preparation can be time-consuming, labor-intensive, and requires a high level of skill. High-resolution structural techniques such as X-ray crystallography have elucidated the structure of individual proteins or smaller sub-complexes, but cannot be used on whole macromolecular complexes. Between widefield microscopy, biochemical analysis, electron microscopy, and crystallography, no single technique can access dynamics, molecular specificity, and high resolution information simultaneously. This resolution gap makes integrating data obtained from different techniques at different scales a formidable challenge.

Advancements in microscopy have bridged this gap by combining the advantages of fluorescence techniques with nanoscale resolution. Super-resolution microscopy overcomes the

diffraction barrier, allowing imaging of fluorescently labeled samples at resolutions from 120 nm, double the resolution of conventional microscopy, down to 20 nm in the *x-y* plane (Betzig et al., 2006; Hell and Wichmann, 1994; Neil et al., 1997; Rust et al., 2006). These revolutionary techniques allow for the study of nanoscale organization of protein arrangement, order, and dynamics in macromolecular complexes.

With the advent of super resolution microscopy, the complex structure of epithelial junctions is more readily accessible to investigation. Sub-junctional protein arrangement, as well as cell level junction organization, play critical roles in function. On the sub-junctional level, proteins can be clustered either homogenously or heterogeneously (Fig. 4A). By widefield, these types of organization are indistinguishable and both appear colocalized. In contrast, super-resolution can reveal colocalization on the nanoscale and distinguish between homogenous mixing and sub-junctional clustering. In some junctions, proteins are found in multi-layer assemblies parallel to the plasma membrane (Fig. 4B). By widefield, proteins in these layers appear to colocalize and the entire structure is encompassed by a diffraction limited puncta. Super resolution can reveal the relative position of the proteins within the junction, proximal or distal to the membrane. Finally, junctions can associate with each other or the cytoskeleton to form sub-micron clusters (Fig. 4C). These clusters all appear the same by widefield, but super resolution allows more precise identification and measurement of the size, distribution, and composition of junctional clusters.

Here we introduce four families of super-resolution methods capable of providing this increased resolution, all of which are commercially available and accessible to many researchers. We will not discuss super-resolution theory and principles in depth and instead refer the reader to the many excellent reviews (Durisic et al., 2014a; Godin et al., 2014; Hell, 2009; Schermelleh et

al., 2010) and practical comparisons between techniques (Dempsey, 2013; Lambert and Waters, 2017; Sydor et al., 2015; Wegel et al., 2016). We then examine the use of super-resolution microscopy for studying epithelial cell junctions, including a discussion of novel findings from these cutting edge approaches.

3.2 Structured Illumination Microscopy

Structured illumination microscopy (SIM) employs a widefield configuration in which the specimen is illuminated by an excitation pattern of parallel lines which interact with the fluorescent structures in the sample. The illumination pattern is phase-shifted and rotated and a series of images are collected and high frequency information from this image series is reconstructed computationally resulting in a super-resolution image (Gustafsson, 2000; Neil et al., 1997). Reconstruction reveals finer structures in the sample with up to twice the resolution in all three dimensions, 120 nm is the *x*-*y* plane and 300 nm in *z*. Variations of SIM using non-linear excitation or emission have achieved resolutions down to 50 nm (Gustafsson, 2005; Heintzmann, 2003; Heintzmann et al., 2002; Li et al., 2015; Perkovic et al., 2014).

SIM offers many advantages, although it can suffer from artifacts and improper implementation (Demmerle et al., 2017). SIM is compatible with most widely used fluorescent labels including both fluorescent proteins and antibodies. Multiplexing multiple channel acquisition is straightforward and SIM can easily address protein co-localization. These features make SIM widely accessible. Images can be obtained at speeds that are limited only by exposure time and camera sensitivities. This grants compatibility with live cell imaging, assuming the dynamics are slower than the acquisition time (Hirano et al., 2015; Lee et al., 2013; Olshausen et al., 2013; York et al., 2012). Additionally, SIM provides optical sectioning, can resolve

structures many microns deep into a sample, and can be combined with *z*-stacks to achieve super-resolution in 3D (Gustafsson et al., 2008; Schermelleh et al., 2008; Shao et al., 2011).

3.3 Single Molecule Localization Microscopy

Single molecule localization microscopy (SMLM) encompasses several methods including photoactivated localization microscopy (PALM) (Betzig et al., 2006), stochastic optical reconstruction microscopy (STORM) (Rust et al., 2006), and ground state depletion individual molecule return (GSDIM) (Fölling et al., 2008; Heilemann et al., 2008), among others (Dertinger et al., 2009; Jungmann et al., 2010; Lemmer et al., 2008; Sharonov and Hochstrasser, 2006). Each of these methods depends on the use of photoswitchable fluorophores to achieve stochastic activation, such that only a small percentage of fluorophores are in a fluorescent "on" state at a given time. Thousands of images are acquired over time in which fluorophores are stochastically turning "on". By temporally separating the emission, individual fluorophores can be resolved in each image. A reconstruction algorithm determines the localization of individual molecules by Gaussian fitting. The super-resolution image is created when the localizations from all the images in the series are combined. SMLM achieves a 10-fold improvement in resolution over the diffraction limit with an *x*-*y* resolution of ~20 nm (Betzig et al., 2006; Fölling et al., 2008; Heilemann et al., 2008; Moerner et al., 2008; Rust et al., 2006). Improvements in axial resolution are provided by total internal reflection fluorescence (TIRF) illumination or point spread function engineering to achieve *z*-resolutions of 50-100 nm.

SMLM depends on the photophysical properties of the fluorescent label. STORM and dSTORM utilize photoswitchable probes typically consisting of chemical dyes conjugated to antibodies in special imaging buffer, which provide multiple localizations per fluorophore. For example, Alexa 647 has optimal photophysical properties including a high photon yield and low

duty cycle (Dempsey et al., 2011). Alternatively, irreversibly activatable fluorophores provide a single off-on cycle. The typical photoactivatable probes used in PALM are genetically encoded, offer a 1:1 labeling stoichiometry, and can provide density information with each localization representing a single protein (Durisic et al., 2014b). SMLM can accommodate multiplexed imaging with multiple probes, live cell imaging (Deschout et al., 2016; Henriques et al., 2011; Jones et al., 2011; Shroff et al., 2008), and 3D imaging with ~50 nm axial resolution (Huang et al., 2008). SMLM has proven to be a powerful tool in studying nanoscale structures and organization in cells and tissues, and its capabilities continue to evolve.

3.4 Stimulated Emission Depletion Microscopy

Reversible saturable optical fluorescence transitions (RESOLFT) microscopy is a category of methods encompassing stimulated emission depletion microscopy (STED) and ground state depletion (GSD) microscopy. Like all super-resolution techniques, STED relies on measuring only a subset of fluorophores to overcome the diffraction limit (Hell and Wichmann, 1994; Klar et al., 2000; Willig et al., 2006). In most STED microscopes, two overlapping lasers are synchronized, one to excite the sample and the other to drive excited fluorophores to the ground state without emission of a photon, thereby depleting the fluorescence (Harke et al., 2013). Because of the doughnut shape of the depletion beam, only fluorophores in the center of the excitation, in the doughnut hole, emit fluorescence. The excitation and depletion beams are raster-scanned over the sample, as in a laser scanning confocal, to acquire a super-resolution image. An advantage of RESOLFT microscopy is that a super-resolution image is directly acquired, with no reconstruction necessary.

If the size and intensity of the depletion beam is precisely tuned, the resolution of STED is theoretically limitless (Harke et al., 2008). Practically, factors including sample type, laser

intensity, and photobleaching result in a lateral resolution limit of ~10 to 70 nm. Resolutions below 10 nm have been reported in a non-biological sample (Rittweger et al., 2009), while 30-40 nm resolution in the *x-y* plane is generally achieved in biological samples (Hein et al., 2010). Without a 3D depletion beam, the axial resolution of STED remains comparable to widefield microscopy, ~ 600 nm. STED is compatible with multi-color imaging, with fluorophores matched to specific imaging lasers. While STED can be used in live cell experiments, concerns centered on phototoxicity due to high laser powers are raised. STED principles have been combined with other imaging modalities to expand the information learned including AFM and FCS. Recent work combined STED with atomic force microscopy (AFM) (Curry et al., 2017) or fluorescence correlation spectroscopy (FCS) (Bianchini et al., 2014).

3.5 Fluorescence Polarization Microscopy

Fluorescence polarization microscopy (FPM) is an unconventional super-resolution technique that utilizes diffraction-limited imaging to achieve sub-diffraction resolution of protein order. FPM has a long history of being used to study the organization of biological structures (Axelrod, 1979; Kampmann et al., 2011; Vrabioiu and Mitchison, 2006). To measure the order of proteins, FPM capitalizes on an intrinsic feature of fluorescent protein tags, the fluorescent dipole (Inoue et al., 2002). The chromophore within the fluorescent protein has an inherent directionality, or dipole, which is strongly excited and emits light parallel to the dipole moment. Epi-fluorescence imaging uses a non-polarized excitation source, so the sample is excited from many directions simultaneously and the dipole orientation of the fluorescent protein is not reflected in the image. In contrast, FPM utilizes a polarized light source, which allows the order of the fluorescently tagged protein to be measured by the changes in intensity. In an ordered case, the fluorescent dipoles will be aligned with one another in the sample and show a change in

fluorescence intensity corresponding to a change in polarization excitation angle. In a disordered case, the fluorescent dipoles will be randomly oriented and changing polarization excitation angle will have no effect on the fluorescence intensity.

Two types of FPM have been developed and applied to biological systems to determine protein order. In excitation- resolved FPM, order is resolved by changing the orientation of the electric field dipole that the sample is excited by and measuring the intensity of the sample in a series of images (DeMay et al., 2011). By emission-resolved FPM, order is instead resolved by exciting all dipole orientations simultaneously and splitting the emission onto different cameras, or different parts of the same camera (Kim et al., 2017; Ohmachi et al., 2012). Each method has advantages and disadvantages depending upon the type of sample. For instance, emission-resolved FPM can be acquired much more rapidly than excitation-resolved FPM so is the better technique for highly dynamic structures. Regardless of type, FPM is a powerful tool for investigating the order and disorder of proteins in macromolecular complexes including yeast septins (DeMay et al., 2011), nuclear pore complex (Atkinson et al., 2013; Mattheyses et al., 2010), desmosomes (Bartle et al., 2017), and the cytoskeleton (McQuilken et al., 2015; Mehta et al., 2016; Valades Cruz et al., 2016). FPM has proven to be effective for studying order of macromolecular complexes in both fixed and live cells, and its capabilities continue to evolve.

3.6 Fluorescence recovery after photobleaching

While fluorescence recovery after photobleaching (FRAP) is not a super-resolution technique, the ability to measure protein diffusion in and out of macromolecular complexes addresses a physical property not accessible by the super-resolution methods discussed here (Cole et al., 1996; Lippincott-Schwartz et al., 2001; Yoon et al., 2001). Since FRAP is generally conducted on a confocal microscope, this allows a small region of interest to be precisely

bleached by scanning with high laser power only within a specified area (Seiffert and Oppermann, 2005). The region of interest can be as small as a single diffraction-limited junction, but generally consists of 3-5 junctions at the cell-cell border. Measuring fluorescence intensity in this region following a bleaching event allows the user to determine two main characteristics of protein mobility in living cells, specifically the rate and the amount of diffusion. To do so accurately, the intensity images must be corrected for photobleaching, background subtracted, and normalized based on the initial intensity prior to bleaching (Sprague and McNally, 2005). A region outside the cell is typically used for background subtraction, while a non-bleached region within the cell can be used as a reference region to verify the bleaching correction and normalization is not introducing error. The intensity over time following bleaching is fit to an association curve, with the equation:

$$y = y0 + (plateau - y0) * (1 - e^{-kx})$$

In this equation *plateau* is the term that defines the mobile fraction, also referred to as the percent recovery (Day et al., 2012). The rate constant is expressed as the term *k*, where the amount of time for 50% of recovery to occur is defined as the $t_{1/2}$ and calculated by the equation:

$$t_{1/2} = ln2/k$$

Correct analysis of the data including corrections, normalization, and curve fitting are essential for quantitatively determining protein mobility in macromolecular complexes.

A disadvantage of FRAP is the unidirectional analysis of recovery, where only diffusion of protein into the complex is directly measured. While many structures can be assumed to maintain an equilibrium where diffusion out of the complex is proportional to diffusion in to the complex, conventional FRAP cannot directly measure diffusion out of the structure. This limitation can be overcome through the use of a photoconvertible probe such as Dendra2 (Baker

et al., 2010; Zhou and Lin, 2013). With a photoconvertible fluorophore, the laser power used for bleaching must be reduced to switch the state of the fluorophore rather than bleach. Conversion can be done with either a 405 nm or 488 nm laser, which results in an emission shift from green (507 nm) to red (573 nm) (Baker et al., 2010). By converting the emission rather than bleaching the region, both green and red channels can be imaged to simultaneously monitor diffusion of non-converted green Dendra2 into the region and converted red Dendra2 out of the region.

Both photobleaching and photoconversion allow measurement of dynamic protein exchange in macromolecular complexes. Fixed imaging modalities and even many live cell imaging methods cannot capture protein dynamics and disregard the important contribution of protein exchange for the function of complexes. Future work should integrate FRAP analysis of protein dynamics with imaging of complex structures to more accurately develop our understanding of the structure-function relationship of cell junctions and other macromolecular complexes.

3.7 General Imaging Considerations for Super-resolution Microscopy

Each super-resolution technique involves tradeoffs between spatial resolution (Fig. 5), temporal resolution, and ease of sample preparation. Sample preparation is always critical in fluorescence microscopy, and improper handling can result in decreased resolution and obscured data interpretation (Brown, 2007; Galdeen and North, 2011; Lambert and Waters, 2017). When the target resolution is higher and distances being measured are smaller, the negative effects of poor sample preparation are exacerbated. Disruption to the ultrastructure from fixation and processing need to be minimized and the density of fluorescent labels should be high. The sample itself becomes part of the optical system and thus the sample must be prepared with coverslips of optimal thickness (#1.5) and appropriate mounting medium for the approach. The

sample coverslip and objective should both be clean, refractive index-matched immersion oil used, and the correction collar on the objective properly set. Any non-specific background or refractive index variations in the sample will be detrimental to the image quality. The calibration and function of the microscope is also critical, and should be verified routinely with standardized samples.

A daunting challenge is the imaging of thick biological specimens. Distortion from light scattering and optical aberrations decrease image resolution when the structure of interest is located further from the coverslip. In this case it may be beneficial to reorient the sample closer to coverslip to improve imaging resolution, for example by cutting thinner tissue sections, preparing sections directly on coverslips to avoid mounting media between coverslip and sample, or by artificially manipulating protein localization within cells. In particular, SMLM techniques are often used in conjunction with TIRF for improved *z*-resolution, though that limits the excitation field to ~140 nm adjacent to the coverslip. If the junction of interest is not located within the TIRF excitation field, a sub-critical incidence angle (also called inclined plane illumination) can be used to reduce out-of-plane fluorescence. While both cell culture models and thin tissue sections (~5 µm) are suitable for localization-based imaging, the resolution of the resulting image may depend on the proximity of the junction to the coverslip. SIM can typically image up to 20 µm into a sample, with resolution decreasing with depth. STED can image as deep as the objective working distance, but resolution will be best within 20 µm of the coverslip.

When interpreting super resolution microscopy data, it is important to consider the distance between the fluorescent label and the protein of interest. A full-size antibody is approximately 10 nm from end-to-end, resulting in a 20 nm “cloud” of uncertainty around an object labeled with both primary and secondary antibodies. The impact of antibody size has been

documented with imaging of microtubules by EM and STORM (Bates et al., 2007; Weber et al., 1978). Immunolabeling methods that reduce the distance between the protein and the fluorophore can be considered including directly labeling primary antibodies (Pástor, 2009), Fab fragments (Brown et al., 2004), nanobodies (Beghein and Gettemans, 2017), and chromobodies (Rothbauer et al., 2006). The size of a fluorescent protein should be considered, for example GFP is a 4.2 nm long cylinder with a diameter of 2.4 nm. The location of the tag on the protein (i.e. N- or C- terminus) must be considered when measuring protein localization. Super-resolution microscopy will be most successful when attention is given to optimizing labeling and sample preparation methods to avoid susceptibility to artifacts.

3.8 Super-Resolution Microscopy of Epithelial Junctions

Understanding of the complex molecular organization of epithelial junctions is an ideal challenge for nanoscale imaging. Now that we have given an overview of techniques and introduced sample preparation considerations, we turn to the application of super-resolution imaging for studying epithelial junctions. In the following sections, we highlight advances in the understanding of the structure and function of epithelial junctions with super-resolution microscopy.

3.8.1 Tight Junctions

Tight junctions (TJs) are localized just below the apical surface of epithelial cells where they form a barrier between the basolateral and apical membranes, contributing to cell polarity and regulating paracellular flux (Andrea Hartsock, 2008; Zihni et al., 2014). Two classes of TJ transmembrane proteins, claudins and occludins, tightly link neighboring cells (Günzel and Fromm, 2012). These transmembrane proteins, along with intracellular scaffold proteins, link TJs to the actin cytoskeleton and to neighboring adherens junctions (AJs) (Niessen, 2007;

Sluysmans et al., 2017). The size, shape, molecular composition, and distribution of TJs are thought to be important for their function.

The polarized apical location of TJs excludes the use of TIRF illumination, which presents a challenge to SMLM based approaches. One way this was overcome was by utilizing reconstituted tight junction strands, which form claudin-claudin interactions throughout regions of cell contact and can be imaged in TIRF (Kaufmann et al., 2012b). A variant of SMLM, spectral position determination microscopy, showed that claudin-3 and claudin-5 expressed in HEK293 cells formed mesh-like structures. The size and shape of the structures differed by protein type, implying differences in their barrier function. This was a breakthrough in visualizing TJs, however the native context and organization was lost in the reconstituted junctions.

TJ architecture, and changes induced by alcohol, were investigated with STORM (Koval et al., 2016; Schlingmann et al., 2016). In primary alveolar epithelial cells, TJs were found to be discrete punctate structures rather than a complex meshwork. Claudin-5 expression was increased and TJ function was impaired with an increase in paracellular leak following alcohol treatment. STORM revealed a corresponding remodeling of TJ architecture where claudin-18 colocalization with the scaffolding protein zonula occludens 1 (ZO-1) decreased at the same time as claudin-18 and claudin-5 colocalization increased. This suggested a mechanism for the reduced barrier function, where claudin-18 associating with claudin-5 dissociates from ZO-1. The differences noted in cluster size (<500 nm^2) and colocalization would not have been detected without super-resolution microscopy.

While SIM, STED, and SMLM have each contributed to an improved understanding of TJ structure, much remains to be studied (Gehne et al., 2017; Kaufmann et al., 2012b; Koval et

al., 2016; Schlingmann et al., 2016; Siljamäki et al., 2014; Van Itallie et al., 2017). Future applications of super-resolution microscopy will allow exploration of TJ structures as they relate to paracellular flux, barrier deficits, and cell polarity in disease.

3.8.2 Adherens Junctions

AJs serve as cell signaling platforms, sites for transcriptional regulation, and play a central role in cell adhesion and polarity (Ivanov and Naydenov, 2013; Perez-Moreno et al., 2003). AJs comprise transmembrane cadherins associating with the actin cytoskeleton through cytoplasmic catenin proteins. The many functions of AJs are paralleled by the complexity of the molecular architecture of the junction. Understanding the organization of protein-protein interactions in AJs is critical for determining the relationship between structure and function in these junctions (Yap et al., 2015).

SIM has been used to study sub-junctional protein organization in AJs. Two transmembrane proteins responsible for mediating adhesion, E-cadherin and nectin, were found to localize to distinct clusters within AJs (Indra et al., 2013). The size and distribution of clusters differed significantly between the two proteins, suggesting that cluster organization regulates adhesive function. Live-cell SIM revealed that size and distribution of E-cadherin and nectin clusters were independent of each other. To further study the interactions between clusters, SIM was coupled with a proximity ligation assay (PLA). While SIM alone resolved distinct clusters, SIM-PLA showed that clusters maintain peripheral points of contact. This combination of SIM with *in situ* measurement of protein-protein interactions allowed precise determination of the structural changes impacting adhesion.

3D SMLM has been used to examine E-cadherin clustering in cell culture and in *in vivo* models at higher resolution (Truong Quang et al., 2013; Wu et al., 2015). The apical “band” of

AJs observed by conventional microscopy was found to consist of distinct E-cadherin clusters (Wu et al., 2015). The size and shape of these clusters was similar to those in more lateral junctions. However, the surface distribution varied based on localization, with apical clusters more closely spaced. Interestingly, while size was unchanged, protein density was decreased in non-adherent versus adherent clusters. Furthermore, both F-actin and E-cadherin extracellular domain interactions were shown to regulate cluster size and density. In another study, E-cadherin cluster size was measured in *Drosophila* embryos (Truong Quang et al., 2013). Both endocytosis and association of E-cadherin with actin were found to regulate cluster size, which followed a power law distribution with a maximum size limited to under 60 nm. These two studies highlight the power of 3D SMLM for investigating cluster size and organization in cells and tissue.

The architecture of AJs was mapped using iPALM, a specialized PALM microscope with <20 nm axial resolution (Kanchanawong et al., 2010a; Shtengel et al., 2009). MDCK cells were plated on coverslips micropatterned with cadherins, which allowed AJs to form at the coverslip-cell interface (Bertocchi et al., 2017a). This unique system oriented the AJs so the axial position of proteins in the half-junction corresponded to the distance from the plasma membrane. Protein locations were mapped, identifying two compartments in the AJ molecular organization. A conformational change in vinculin following activation was shown to bridge the compartments while impacting the localization of several actin regulating proteins. This analysis identified a modular architecture and is a critical step toward our understanding of the relationship between structure and mechanical integration in AJs.

3.8.3 Gap Junctions

Gap junctions form channels to transport ions and small molecules through hexameric assemblies of connexins, thereby providing direct communication between neighboring cells

(Goodenough and Paul, 2009). Compared to the other epithelial junctions, gap junctions have a relatively simple molecular architecture. It was in part this simplicity that drove the use of connexin (Cx) 43 in seminal live-cell STED experiments (Hein et al., 2010). STED revealed many small Cx43 clusters previously not reported by confocal microscopy. Questions remain about the organization of connexin isoforms within gap junctions and the distribution of gap junctions along cell membranes.

Given that mutations in Cx26 are the most common genetic cause of childhood hearing loss (Kemperman et al., 2002), the structure and organization of gap junctions is of significant interest. The expression of Cx26 and Cx30 was examined by SIM to determine if junctions in the human cochlea were hetero- or homotypic (Liu et al., 2016). SIM showed that connexins form homotypic rather than heterotypic channels, as previously thought based on colocalization by widefield microscopy (Marziano et al., 2003; Ortolano et al., 2008). The differential distribution of gap junctions based on connexin isoform in the sensory epithelium of the human cochlea was studied by SIM (Liu et al., 2017). Cx26 was found to be weakly expressed and present in small plaques, while Cx30 plaques dominated. Variations in the size of Cx30 plaques were found to be cell type dependent. In some areas of the cochlea, Cx30 formed a large network thought to be important for K^+ signaling. SIM also revealed areas where Cx26 formed small puncta closely associated with the larger Cx30 network, which could not have been resolved by widefield or confocal microscopy. This work suggests that the distribution of Cxs in the cochlea is important for function and indicates that disruption of connexin networks may be a mechanism for hearing loss.

Although not an epithelial tissue, super-resolution microscopy has proven a powerful tool in studying gap junctions in the cardiac intercalated disc. The molecular arrangement of these

complex junctions relates to proper electrical and mechanical function and is disrupted in heart diseases including arrhythmogenic cardiomyopathy (AC) (Agullo-Pascual et al., 2014a; Kant et al., 2015b). SMLM revealed that Cx43 and the "desmosomal" protein plakophilin-2 (Pkp-2) form discrete punctate junctions that physically interact, with Pkp-2 partially localized to the edge of connexin 43 plaques (Agullo-Pascual et al., 2013b; Malkusch et al., 2013). This result is in contrast to prior understanding of the molecular arrangement of these junctions as separate. The identification of nanoscale Cx43-Pkp-2 subdomains by SMLM indicates an interactive hub (a 'connexome') for molecules that traditionally are classified as gap junction or desmosome to come together to control cardiac function.

3.8.4 Desmosomes

Desmosomes are the primary junction responsible for maintaining cell adhesion in epithelial tissues by resisting mechanical stress (Berika and Garrod, 2014; Johnson et al., 2014b; Kowalczyk and Green, 2013). Desmosomes consist of transmembrane cadherins and intracellular plaque proteins that bind to the intermediate filament cytoskeleton (Garrod and Chidgey, 2008). By EM desmosomes appear as a pair of electron dense plaques along the plasma membrane, averaging ~500 nm in length (Odland, 1958; Selby, 1955; Tamarin and Sreebny, 1963). The internal molecular architecture of desmosomes cannot be resolved by widefield or confocal microscopy, because they appear as diffraction limited spots (Stahley et al., 2016a).

The resolution provided by SIM allowed for significant advancements in understanding desmosome dynamics and the pathogenesis of the autoimmune disease Pemphigus Vulgaris (PV). SIM identified co-localization of desmosomal cadherin desmoglein 3 with lipid raft markers in primary human keratinocytes (Stahley et al., 2014). This, combined with biochemistry, helped to identify a role for lipid rafts in desmosome assembly and disassembly

dynamics. In PV patient tissue desmosome size was reduced and Dsg3 was found to be aberrantly clustered and localized in "linear arrays" (Stahley et al., 2016b). The mirror symmetry created by desmosomal plaques was visible in the SIM images, which allowed identification of desmosomes "split" along the adhesive interface at blister sites. Desmosome splitting was recapitulated *in vitro* by exposing cultured keratinocytes to PV IgG and to mechanical stress, demonstrating that mechanical stress can lead to desmosome splitting. SIM contributed insights into how protein organization, trafficking, and function are altered in PV patient tissue.

The increased resolution of dSTORM made it possible not only to resolve the plaque mirror symmetry, but also to quantify the organization of proteins within desmosomes (Stahley et al., 2016a). Plaque localization and length were measured for several core desmosomal proteins in primary keratinocytes, resulting in a molecular map. This revealed that the desmosomal proteins are not arranged completely perpendicular to the plasma membrane but instead splay outward into the cytosol, a level of organization not previously detected. In hyper-adhesive desmosomes, the molecular map revealed changes in desmoplakin orientation, with the C-terminal domain moving closer to the plasma membrane. These changes correlated with those measured in suprabasal vs. basal cells in human skin sections. Together this indicates that desmosome molecular architecture and the organization of plaque proteins is critical for desmosome function.

Super-resolution studies of the intercalated disc in murine cardiomyocytes are also of interest when considering desmosome structure. Defects in desmosomal proteins, including Pkp-2, can result in disruption of the intercalated disc, causing AC. dSTORM revealed a nanoscale retraction of the microtubule plus end from N-cadherin in Pkp-2 deficient mice, suggesting a mechanism for AC that relies on Pkp-2 integrity (Cerrone and Delmar, 2014). Related work

found that, like disruption of Pkp-2, truncation of Cx43 dissociated the microtubule plus end from the junction site and resulted in mislocalization of NaV1.5, the sodium channel protein integral to cardiac function (Agullo-Pascual et al., 2014b). The use of dSTORM in these studies linked electrical coupling, cell adhesion, and excitability in the heart through a common mechanism of microtubule attachment.

Super resolution imaging of desmosomes has thus far explored the ultrastructure of the complex and demonstrated a correlation between structure and function. These approaches will allow quantification of desmosomal structure as it relates to disease, wound healing, and embryogenesis.

3.8.5 Hemidesmosomes

In stratified epithelia, hemidesmosomes anchor basal cells to the underlying basement membrane. Hemidesmosomes are distinct from desmosomes in their protein composition, but derive their name from their association with the intermediate filament cytoskeleton and a similar “spot-weld” like appearance as seen by EM. The molecular organization of hemidesmosomes has been challenging to study due to the limited resolution of conventional microscopy.

Multi-color GSDIM revealed that the hemidesmosome integrin β4 was distributed alongside and not directly under the keratin fibers in cultured primary keratinocytes (Nahidiazar et al., 2015). Association with the linker protein plectin regulated the distance between β4 and keratin. Quantification showed that integrin BP180 and β4 co-distributed in characteristic structures along keratin filaments. Interestingly, a zone at the cell periphery contained β4 but not BP180, indicating recruitment of plaque protein BP180 only to mature hemidesmosomes. BP180 and BP230 were found to be organized in distinct concentric structures. Quantification of the

architecture in cultured keratinocytes and human skin sections were consistent. These results suggest a complex interdependence of hemidesmosome structure and protein function. Prior to this work, very little was known about the architecture of hemidesmosomes or how they associate with the keratin intermediate filament cytoskeleton. The resolution of GSDIM was critical for the determination of the molecular organization of the hemidesmosome, which could provide the building blocks for future work studying different functional states and possible disease mechanisms.

3.9 Conclusion

In the past decade, our ability to observe protein organization at the nanoscale has vastly improved. A variety of approaches have broken the diffraction barrier and enabled us to visualize structures in their cellular context as was previously accessible only by EM. Development in optics, reconstruction algorithms, labeling methods, and fluorescent probes, will continue to advance super-resolution microscopy. Combining super-resolution microscopy with other advanced imaging modalities can also provide access to novel information. Examples of this combinatorial approach include correlative super-resolution and electron microscopy (CLEM) (Johnson and Kaufmann, 2017), confocal (Soeller et al., 2017), fluorescence polarization (Valades Cruz et al., 2016), fluorescence correlation spectroscopy (FCS) (Sarangi et al., 2016), fluorescence lifetime imaging (FLIM) (Vicidomini et al., 2015), or atomic force microscopy (AFM) (Bondia et al., 2017).

Super-resolution microscopy has allowed a more detailed visualization and quantification of the 3D molecular architecture of cell junctions in living or fixed cells and tissues. These techniques are highly suitable for studying macromolecular complexes and enable the investigation of novel questions about junction architecture and how complex structure relates to

function.

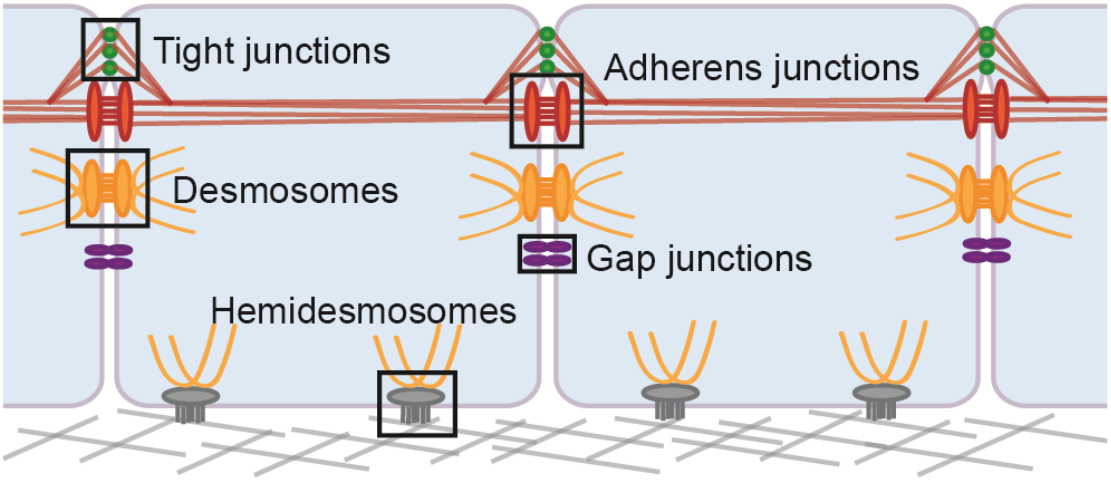

Figure 3. Epithelial cell junctions. Tight junctions are localized apically on the lateral membrane of epithelial cells. They interact with the neighboring adherens junctions, and both junctions integrate with the actin cytoskeleton, shown in red. Desmosomes are located throughout the lateral membrane, below the adherens junctions, and associate with the intermediate filament cytoskeleton, shown in yellow. Gap junctions are also distributed throughout the lateral cell membrane where they form channels that allows passage of ions and small molecules between the two cells. In stratified epithelia, hemidesmosomes are localized to the basal membrane where they promote adhesion to the underlying substrate and integrate with intermediate filaments.

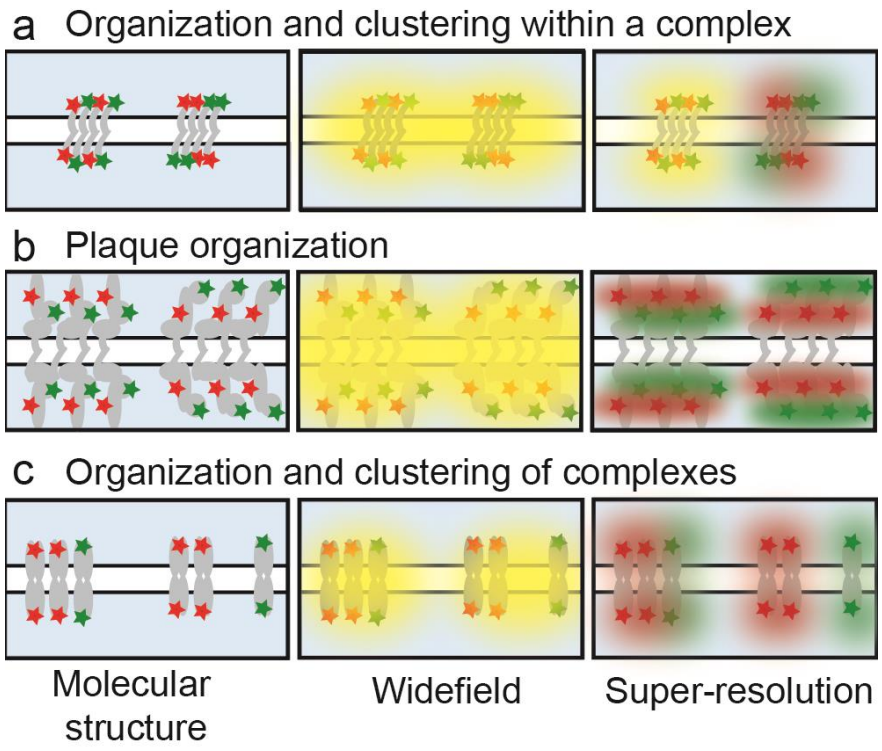

Figure 4. Protein organization in epithelial junctions. Illustration of different junctional molecular structures within the diffraction limit that cannot be distinguished by widefield microscopy, but are distinct by super-resolution. (a) Junctions can contain a homogenous mix of proteins (left) or distinct clusters (right). (b) Junctional plaque proteins are organized in layers parallel to the plasma membrane, with the red protein more distal (left) or proximal (right) to the membrane. (c) Junctions can have higher-order organization within the cell membrane with clusters of mixed junctions (left) or segregation of like junctions into distinct structures (right).

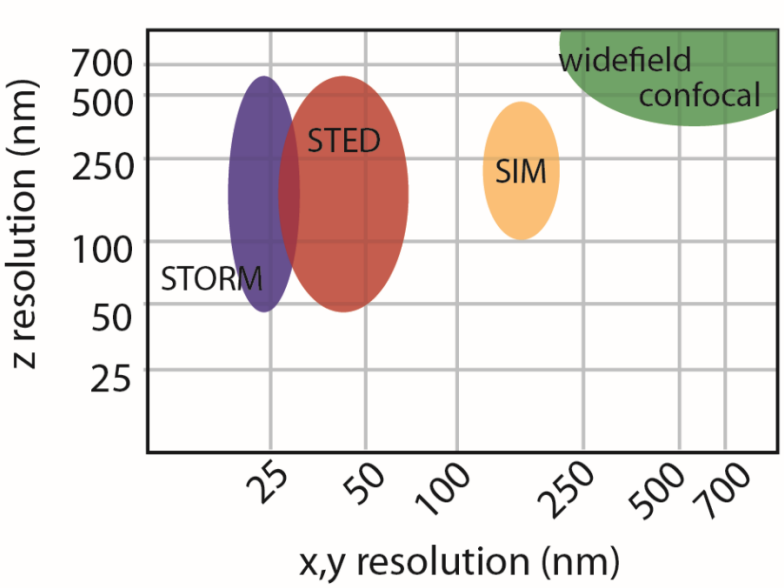

Figure 5. Spatial resolution. The resolution of widefield or confocal microscopy is determined by the numerical aperture of the objective and wavelength of the excitation light and is ~250 nm in *x-y* and 600 nm in *z*. SIM doubles the resolution in all three dimensions achieving ~125 nm lateral resolution and ~300 nm axial resolution. STED and STORM can achieve a range of axial resolutions, depending on the use of TIRF or 3D imaging modalities. In general STORM achieves a slightly better *x-y* resolution of ~20 nm, as opposed to ~40 nm by STED. These resolutions are approximations based on commercially available systems. Variations in the resolution of each method depend on the properties and quality of the sample, as well as the particular optical setup.

Chapter 4

Molecular organization of the desmosome by super-resolution microscopy

This chapter is adapted from:

Stahley, S.N., **E.I. Bartle**, C.E. Atkinson, A.P. Kowalczyk, and A.L. Mattheyses. 2016. Molecular organization of the desmosome as revealed by direct stochastic optical reconstruction microscopy. *J. Cell Sci.* 129:2897-2904.

My contribution to this work was in the form of experimental design, conducting experiments, editing the manuscript, and intellectual discussion. I stained and/or imaged ~50% of the samples and conceptualized and created Figure 7, panel G.

4.1 Introduction

Desmosomes are intercellular junctions abundant in tissues that experience considerable mechanical stress, such as the heart and skin (Kowalczyk and Green, 2013). The importance of desmosome-mediated adhesion is evidenced by the numerous human diseases that result when desmosomes are compromised, manifesting in epidermal fragility, cardiomyopathies, and cancers (Broussard et al., 2015; Stahley and Kowalczyk, 2015).

The desmosome is a macromolecular complex that forms a 'spot-weld' of strong intercellular adhesion and is comprised of transmembrane cadherins and cytoplasmic plaque proteins (Berika and Garrod, 2014; Saito et al., 2012). The desmosomal cadherins (desmogleins and desmocollins) link neighboring cells through extracellular adhesive interactions while armadillo protein family members plakoglobin (PG) and plakophilin, and plakin family member desmoplakin (DP) contribute to the intracellular plaque (Fig. 6A). Plaque ultrastructure is characterized by two electron-dense regions: the plasma membrane proximal outer dense plaque and the inner dense plaque (Desai et al., 2009; Farquhar and Palade, 1963; Stokes, 2007). The cadherin cytoplasmic tails bind to proteins in the outer dense plaque while the C-terminus of DP binds to intermediate filaments in the inner dense plaque. This tethers the desmosome to the intermediate filament cytoskeleton, establishing an integrated adhesive network (Bornslaeger et al., 1996; Harmon and Green, 2013).

Many desmosomal protein interactions have been characterized by biochemical studies (Bass-Zubek and Green, 2007; Green and Simpson, 2007; Thomason et al., 2010), while desmosomal ultrastructure has been studied by immunogold and tomographic electron microscopy (Al-Amoudi et al., 2011; Al-Amoudi and Frangakis, 2008; North et al., 1999a; Owen et al., 2008; Stokes, 2007). Yet, studying desmosomes on a molecular level remains challenging

due to their size, insolubility, and molecular complexity. Measuring desmosomal protein organization requires a technique with high resolution coupled with minimal sample manipulation to minimize structural artifacts and preserve physiological relevance. Super-resolution microscopy has revealed sub-resolution protein organization in numerous macromolecular complexes including: nuclear pore, ciliary transition zone, kinetochore, neuronal synapse, focal adhesion, and hemidesmosome (Chatel et al., 2012; Loschberger et al., 2014; Loschberger et al., 2012; Nahidiazar et al., 2015; Ribeiro et al., 2010; van Hoorn et al., 2014; Yang et al., 2015; Zhong, 2015). Here, we use direct stochastic optical reconstruction microscopy (dSTORM) (Rust et al., 2006) to elucidate protein organization within the desmosome at the molecular level both *in vitro* and *in vivo*.

4.2 Results and Discussion

4.2.1 Desmosome plaques resolved by dSTORM

Two proteins, inner dense plaque protein DP and outer dense plaque protein PG, were utilized to establish dSTORM for studying desmosome organization. Primary human keratinocytes were pre-extracted prior to fixation and the desmosomal pool of proteins(Palka and Green, 1997) was immunostained with primary antibodies against DP C-terminus or PG N-terminus. The same cell-cell border was then imaged by widefield, structured illumination microscopy (SIM), and dSTORM.

In widefield, DP fluorescence is punctate and pixilated with no discernable structural features. In contrast, two distinct DP plaques, one contributed by each cell, are resolved by SIM as previously shown (Fig. 6B,C) (Stahley et al., 2015). Likewise, two individual DP plaques are resolved by dSTORM, but with a more distinct separation (Fig. 6C). To analyze the difference in spatial resolution between the imaging techniques, fluorescence intensity was plotted as a

function of distance along the desmosome axis, perpendicular to the plasma membrane. While there is only a single intensity peak from the widefield image, two individual peaks, corresponding to the two plaques, are resolved from SIM and dSTORM images (Fig. 6D).

PG-labeled desmosomes imaged by widefield have a punctate appearance, similar to DP (Fig. 6E,F). Similarly, PG fluorescence by SIM is punctate with no evident internal structure. In contrast, dSTORM revealed two individual PG plaques (Fig. 6F). This is also shown in the plot of fluorescence intensity along the desmosome axis (Fig. 6G).

To confirm dSTORM resolves individual desmosomes consisting of plaques contributed by two different cells, keratinocytes were dual-labeled for the extracellular domain of Desmoglein 3 (Dsg3) and the C-terminus of DP. dSTORM revealed a distinct separation, with the Dsg3 extracellular domain sandwiched between two DP plaques (Fig. 6H). In our experiments the localization precision of Alexa488 (~19.5nm) was less than that of Alexa647 (~5.8nm), similar to that reported by others (Dempsey et al., 2011; Tam et al., 2014). Therefore, Alexa647 was used for quantitative measurements unless otherwise indicated. Image resolution is also impacted by the primary and secondary antibody labels, which increases the apparent size of structures (Bates et al., 2007).

In summary, these results demonstrate that dSTORM can resolve proteins in both the outer and inner dense plaques in individual desmosomes.

4.2.2 Molecular map of the desmosome by dSTORM

Next, we systematically quantified the molecular arrangement of proteins in the desmosome. In keratinocytes, proteins were labeled with domain-specific antibodies: Dsg3 N-term (Alexa488), PG N-term, Dsg3 C-term, DP N-term, DP rod, and DP C-term (Fig. 7A and Supplemental Table 1) and their distributions along the desmosomal axis were determined using

dSTORM. The mirror symmetry of desmosomal plaques allowed us to identify individual desmosomes, and only those with their axes in the *x-y* focal plane were analyzed (Fig. 7B and Supplemental Fig. 1). A linescan of fluorescence intensity along the desmosome axis was created for each desmosome (Fig. 7C). The axial distribution of proteins was automatically measured as the distance between peaks from the linescans. This plaque-to-plaque distance was measured from multiple individual desmosomes labeled for each protein domain (Fig. 7D). There was a progressive increase in the average plaque-to-plaque distance with PG N-term closest to the plasma membrane and DP C-term furthest (Supplemental Table 2). All plaque-to-plaque distances were significantly different from one another with the exception of PG N-term and Dsg3 C-term, and PG N-term and DP N-term (Fig. 7E). This is consistent with PG interacting with both the cytoplasmic tail of Dsg3 and the N-term of DP (Delva et al., 2009).

The length of the desmosome, parallel to the plasma membrane, was also determined for each protein domain (Fig. 7F). There was a trend of increasing length with increasing distance from the plasma membrane. This trend was also reflected at the protein domain level: the DP C-term length was significantly longer than that either DP N-term or DP rod (Supplemental Table 2). A composite molecular map includes protein localizations and desmosome length, illustrating the possible arrangement of proteins splaying out from the membrane (Fig. 7G).

We next sought to determine whether the arrangement of proteins measured in primary human keratinocytes was conserved among the immortalized human keratinocyte cell line HaCaT and the human epidermoid carcinoma cell line A431. Individual DP rod- and PG N-term-labeled desmosomes were imaged in all cell types and there were no significant differences in plaque-to-plaque distances (Supplemental Fig. 2). This suggests the general organization of

proteins in desmosomes is conserved across primary keratinocytes and human cell lines derived from skin.

Desmosome protein organization has been previously studied with electron microscopy approaches, measured as distance from the plasma membrane. For comparison, dSTORM plaque-to-plaque measurements were converted into a plasma membrane reference system by subtracting the width of the intercellular space (~34 nm); (Al-Amoudi et al., 2004), subtracting two times the plasma membrane thickness (~4-6 nm), and finally dividing by two (see Fig. 7G for reference). The dSTORM distributions of Dsg3 C-term and PG N-term overlap with the corresponding distributions of gold labels in immuno-EM studies (North et al., 1999a) and the dSTORM PG N-term distribution overlaps with the PG layer identified by cryoelectron tomography (Al-Amoudi et al., 2011). In contrast to immunogold studies, dSTORM indicates that DP is localized further from the plasma membrane.

While desmosome length has been previously measured with electron microscopy, dSTORM uniquely allows for protein domain-specific analysis. The corresponding increase in plaque length and plaque-to-plaque distance indicates that the desmosome splays out as it extends from the plasma membrane into the cell. DP has two isoforms, DPI and DPII, each with globular N- and C- termini separated by a central rod domain. The average N- to C-term length of DPI is 162nm and DPII is 63nm (O'Keefe et al., 1989). The distance between DP N- to C-term measured perpendicular to the plasma membrane by dSTORM is 54±4nm, on par with previous measurements (North et al., 1999a) while the length of the DP C-term plaque extends 77±13nm beyond the DP N-term plaque. This suggests DP is oriented with its long axis at an angle in the plaque, not perpendicular to the plasma membrane. The minimum length that will fit this model is 94nm, significantly less than the length of DPI. The DPII rod domain could span

the 54nm, but at a smaller angle. While we cannot rule out an additional disorganized or kinked conformation of the rod, our data strongly suggests that DP is oriented at an angle in the plaque.

4.2.3 Reorganization of plaque proteins in PKP-1-mediated hyperadhesive desmosomes

Desmosomes can exist in a weaker calcium-dependent state and a stronger calcium-independent, or hyperadhesive state (Garrod et al., 2005; Kimura et al., 2007). Plakophilin 1 (PKP-1) promotes desmosome formation by recruiting and clustering desmosomal proteins, and overexpression of PKP-1 has been shown to induce hyperadhesion in cultured keratinocytes (Bornslaeger et al., 2001; Hatzfeld et al., 2000; Tucker et al., 2014). To test if plaque organization changes with adhesive state, adenoviral PKP-1.myc overexpression was used to shift desmosomes to a hyperadhesive state. With PKP-1.myc overexpression an approximate 8-fold increase in PKP-1 protein level was observed compared to empty vector control (Supplemental Fig. 3). Keratinocytes were labeled with antibodies against PG N-term, Dsg3 C-term, DP N-term, DP rod, and DP C-term (Fig. 8A). Cells were also labeled with anti-myc, and PKP-1.myc expression was confirmed by widefield co-localization. Plaque-to-plaque distance was measured from multiple individual desmosomes for each protein domain (Fig. 8B). A significant decrease in plaque-to-plaque distance was measured for Dsg3 C-term, DP rod, and DP C-term. In contrast, the distribution of PG and DP N-term did not significantly change (Fig. 8C; Supplemental Table 3). An increase in desmosome length was observed with PKP-1.myc overexpression similar to previous studies (Fig. 8D; Supplemental Table 4) (Tucker et al., 2014).

Our data show that the plaque-to-plaque distance for some, but not all, protein domains decreases in PKP-1-induced hyperadhesion. Notably, DP N-term plaque-to-plaque distance does not change with PKP-1.myc overexpression compared to control, while both DP rod and C-term decrease. The N-term plakin domain of DP has an “L” conformation consisting of two

perpendicular lobes separated by a flexible elbow with a flexible linker connecting the N-term to the rod domain (Al-Jassar et al., 2011; Grum et al., 1999). Our data supports previously proposed models in which a conformational change within the plakin domain elbow or the flexible linker allows for motion of the rod and C-term within the plaque, while the N-term is stationary (Al-Jassar et al., 2011). PKP-1 has also been shown to interfere with PG-DP binding (Bornslaeger et al., 2001) and thus it is possible the proposed conformational change also reflects a change in binding partner.

The difference in ultrastructure measured with dSTORM could contribute to the increased adhesive strength and mechanism of desmosome maturation. Interestingly, knockdown of PKP-3 in SCC9 cells has been shown to weaken cell adhesion and increase desmosome width (Todorovic et al., 2014). That result, along with those presented here, support the hypothesis that changes in protein organization within the desmosomal plaque correlate with changes in adhesive strength.

4.2.4 Desmosome molecular organization is conserved in skin

To investigate if desmosomal plaques could be identified *in vivo*, human skin sections labeled with antibodies against the DP rod domain were imaged by dSTORM. The epidermis is a stratified epithelium and imaging the DP rod domain revealed pairs of individual plaques in basal cells adjacent to the basement membrane and suprabasal cells in the spinous and granular layers (Fig. 9A).

To quantify the protein arrangement in skin, PG N-term, DP rod, or DP C-term were labeled and imaged by dSTORM. The plaque-to-plaque distances reveal that the overall axial arrangement of protein domains was similar in skin and cell culture. Next, we wanted to see if the arrangement was the same in basal and suprabasal cells. Plaque-to-plaque distances

compared between basal and suprabasal desmosomes for PG N-term or DP rod were not significantly different. However, for DP C-term, the plaque-to-plaque distance decreased significantly by 65±11nm (Fig. 9C; Supplemental Table 5).

Expression levels of desmosomal proteins change with keratinocyte differentiation in the epidermis (Delva et al., 2009). PKP-1 expression is increased in suprabasal compared to basal cells, and the decrease in DP C-term plaque-to-plaque distance in these desmosomes agrees with our PKP-1.myc overexpression results in cell culture. However, DP rod plaque-to-plaque distance was unchanged between basal and suprabasal desmosomes, which could reflect variations in plaque re-organization due to protein overexpression verses epithelial differentiation.

In summary, our results demonstrate the ability of dSTORM to investigate the nanoscale arrangement of proteins within intact desmosomal plaques, in cell culture and human tissue. Desmosomes are dynamic, exist in different adhesive states, and can be disrupted by disease, and this resolution will likely prove powerful in understanding the relationship between molecular organization and desmosomal adhesive state (Garrod et al., 2005; Getsios et al., 2004; Green et al., 2010; Kitajima, 2014). The approach developed here is applicable to many aspects of desmosome biology including their interaction with intermediate filaments, the impact of intracellular signaling on plaque organization, and disruption in disease. With relatively straightforward sample preparation, compatibility with cells and tissues, and single desmosome resolution, this approach is poised to integrate functional and structural analysis of desmosomes.

4.3 Materials and Methods

Cell Culture.

Human epidermal keratinocytes were isolated from neonatal foreskin as previously described (Calkins et al., 2006) and cultured in supplemented KBM-Gold (Lonza, Walkersville, MD). Keratinocytes, passage 2-3, were seeded onto 8-well #1.5 coverslip bottom microslides (Ibidi GmbH, Planegg-Martinsried, Germany). Media was increased to 550μM calcium 16–20 hours before fixation. Where indicated, keratinocytes were infected with empty or PKP-1.myc adenovirus (Tucker et al., 2014) 36 hours before fixation. HaCaT and A431 cells were cultured in DMEM (Corning, Tewksbury, MA) supplemented with 10% FBS and 1% Pen/Strep.

Antibodies.

Antibodies used: Anti-Dsg3 AK15 (Tsunoda et al., 2003) (gift from Dr. Masayuki Amagai, Keio University); anti-Dsg3 G194 (Progen Biotechnik GmbH, Heidelberg); anti-γ-catenin (Santa Cruz Biotechnology, Santa Cruz, CA); anti-desmoplakin I/II (Fitzgerald, Acton, MA); desmoplakin antibodies NW6 and NW161 (gift from Dr. Kathleen Green, Northwestern University) and anti-myc (Bethyl Labs, Montgomery, TX). Additional information in Table S1. Secondary antibodies (IgG H&L) conjugated to Alexa Fluors (Invitrogen, Grand Island, NY). For western blot: anti-PKP-1 (Sobolik-Delmaire et al., 2006) (gift from Dr. James Wahl III, University of Nebraska) and anti-Actin C2 (Santa Cruz).

Immunofluorescence.

Fixation and labeling protocols were adapted from (Whelan and Bell, 2015). Cells were pre-extracted (60 seconds) with 300mM sucrose and 0.2% Triton-X 100 to remove non-desmosomal proteins. This was followed by fixation (12 minutes, 37°C) with 4% paraformaldehyde prepared fresh from 16% EM grade (Electron Microscopy Sciences, Hatfield, PA). Samples were washed, blocked, and permeabilized (30 minutes) in 3% bovine serum albumin (BSA) and 0.2% Triton-X 100. Samples were incubated with primary (3 hours) and secondary antibodies (1 hour), with

multiple washes in between. Samples were stored light-protected (PBS^+, 4°C) and imaged within 2 weeks.

Human tissue biopsy processing.

Human skin biopsy use was approved by the Emory University Institutional Review Board. 5µm thick sections from OCT-embedded biopsies were mounted onto glass coverslips and processed for immunostaining. Tissue sections were labeled sequentially with primary and secondary antibodies (1 hour) with triple PBS^+ washes between incubations.

Immunoblotting.

Cells were harvested and immunoblotting performed using standard procedures (Stahley et al., 2014).

Microscopy.

SIM images were obtained and reconstructed with a Nikon N-SIM Eclipse Ti-E microscope system (Nikon Instruments, Melleville NY) equipped with a 100×/1.49 NA oil immersion objective, 488nm laser, and EMCCD camera (DU-897, Andor Technology, Belfast, Northern Ireland). dSTORM images were obtained with a Nikon N-STORM microscope equipped with a 100x/1.49 NA oil immersion objective, 488 and 647nm lasers, and an iXon ultra EMCCD camera (Andor). Typically, 60-80,000 frames were collected with inclined sub-critical excitation. Images were reconstructed in Nikon Elements. Widefield images were obtained with low intensity laser excitation on the N-STORM system. Photoswitching imaging buffer included glucose oxidase (Sigma, St. Louis, Missouri), catalase (Roche, Penzberg, Germany), glucose (Sigma), and β-mercaptoethanol (Sigma) (Rust et al., 2006).

Image Analysis.

dSTORM images were exported at 4nm/pixel and analyzed using MATLAB (Mathworks, Natic, MA). Individual desmosomes were manually identified and automatically excised and aligned such that the desmosome axis was horizontal. Intensity was measured along the desmosome axis by averaging all pixels along the desmosome length. Linescans were normalized, smoothed, and the peak finder function in MATLAB (40% intensity peak threshold) identified linescans with two peaks for quantification. For Dsg3 N-term, linescans with one peak were selected.

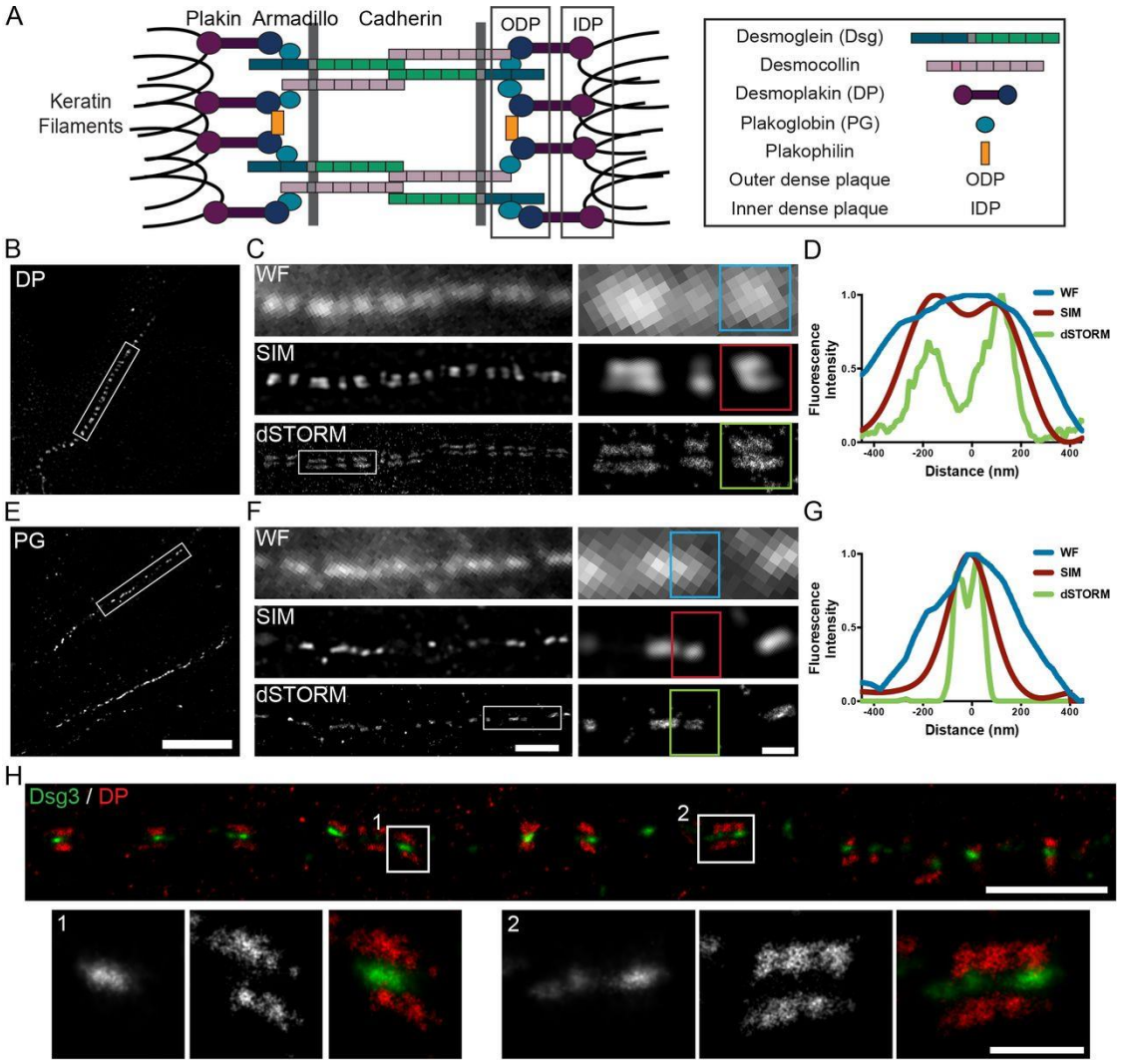

Figure 6. Super-resolution imaging of desmosomes. (A) Desmosome schematic. (B,C,E,F) Cultured human keratinocytes labeled for the desmoplakin (DP) C-terminal domain or plakoglobin (PG) N-terminal domain and imaged by widefield microscopy (WF), SIM and dSTORM. (B) SIM image of desmoplakin cell border. (C) Desmoplakin-labeled region of interest imaged by widefield microscopy, SIM and dSTORM. (D) Linescan across a single desmosome indicated by the colored boxes. (E) SIM image of plakoglobin cell border. (F) Plakoglobin-labeled region of interest imaged by widefield microscopy, SIM and dSTORM. (G) Linescan across a single desmosome indicated by the colored boxes. (H) dSTORM image of keratinocyte cell–cell border labeled for the Dsg3 N-terminal (Alexa Fluor 488, green) and

desmoplakin C-terminal (Alexa Fluor 647, red) domains. Scale bars: 10 μm (B,E); 2 μm (C,F,H); 500 nm (C,F,H, insets).

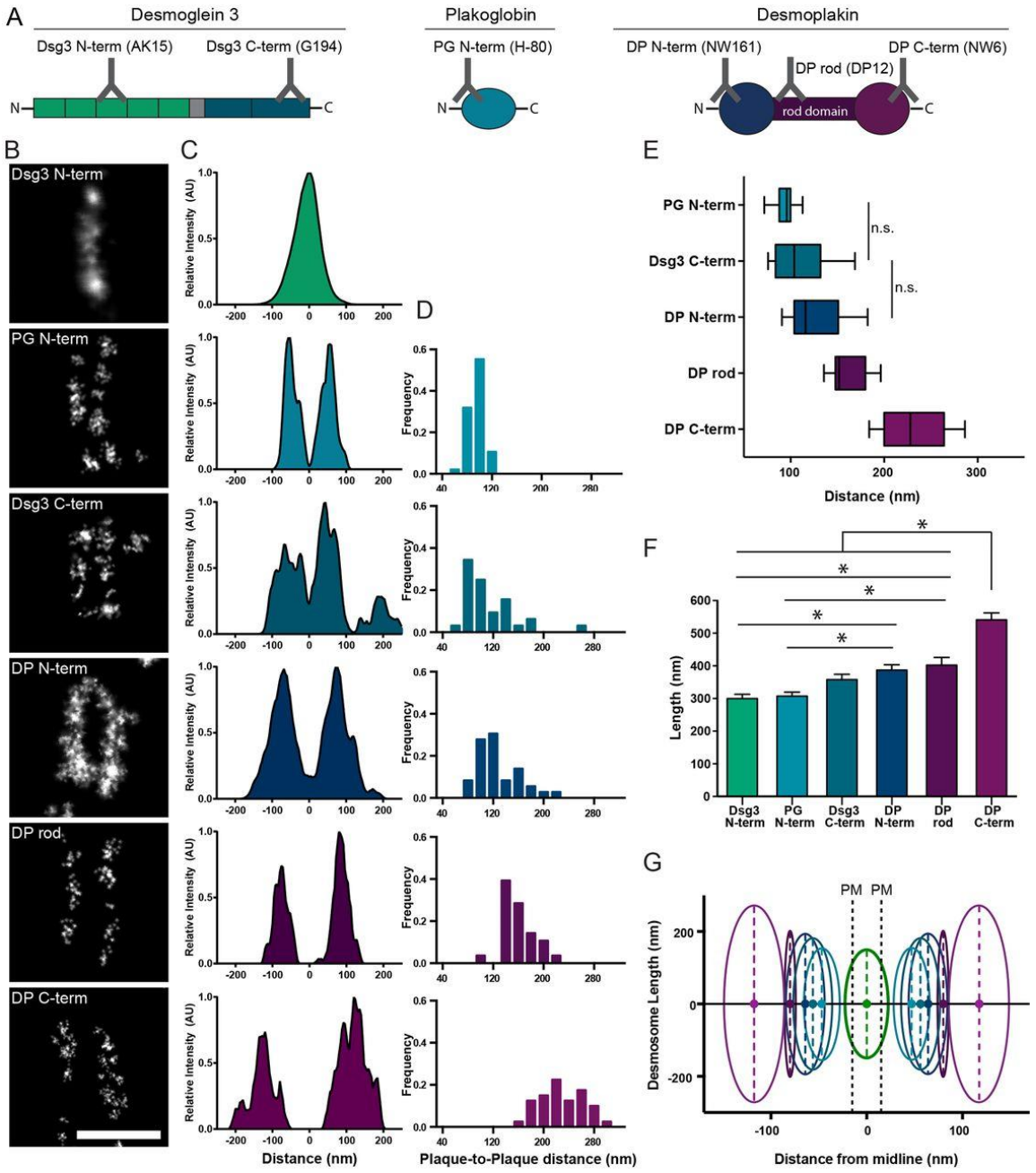

Figure 7. Molecular map of the desmosome as revealed by dSTORM. (A) Approximate binding locations of antibodies used for dSTORM in desmoglein 3 (Dsg3), desmoplakin (DP) or plakoglobin (PG). (B) Representative images of individual desmosomes labeled with the indicated antibodies, from 2–4 preparations. Scale bar: 500 nm. (C) Fluorescence intensity linescan along the desmosomal axis (horizontal through image as shown). (D) Histograms of

plaque-to-plaque distance from all desmosomes analyzed for each protein domain. (E) Box-and-whisker plot of plaque-to-plaque distance. The box represents the 25–75th percentiles, and the median is indicated. The whiskers show the 10–90th percentiles. (F) Desmosome length. Mean±s.e.m. *P<0.05 (one-way ANOVA with Holm-Sidak's multiple comparisons test). For D–F, Dsg3 N-term, n=69; PG N-term, n=47; Dsg3 N-term, n=32; DP N-term, n=36; DP rod, n=28; DP C-term, n=40. (G) Composite dSTORM map where 0 is the midline, distances represent half the mean plaque-to-plaque distance, oval height represents desmosome length, and oval width represents the standard deviation of the peak width. PM, plasma membrane.

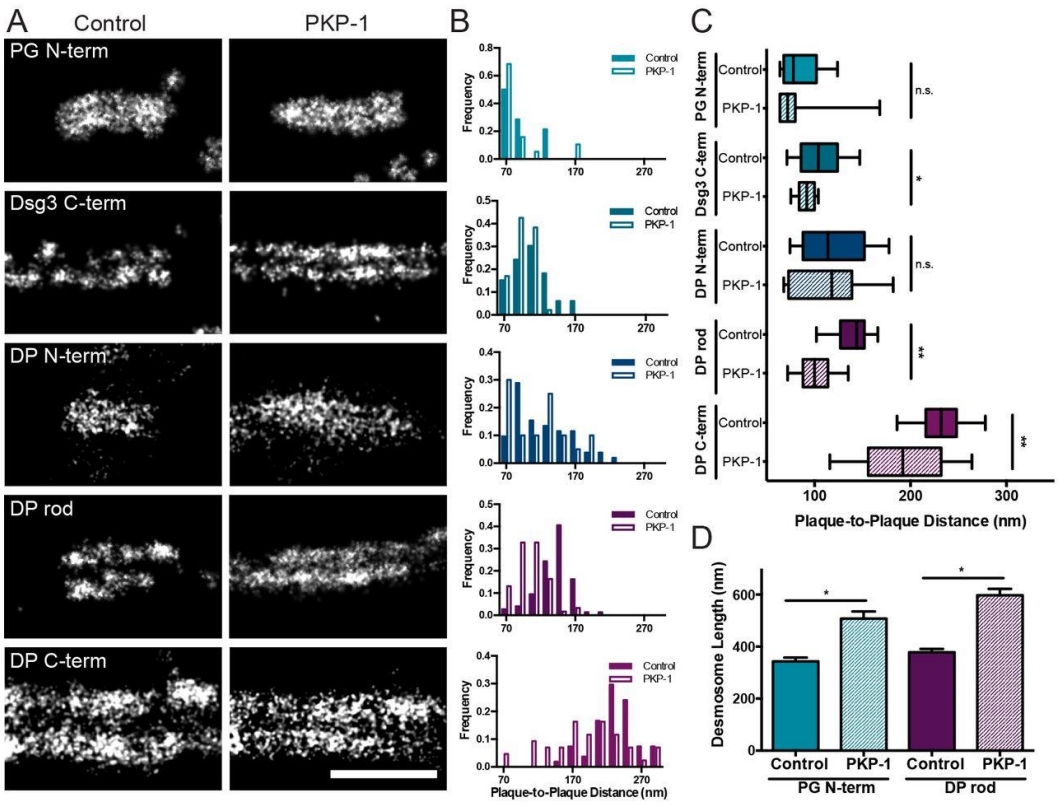

Figure 8. PKP-1-mediated hyperadhesion altered the molecular map of the desmosome. (A) dSTORM images of individual desmosomes from cultured primary keratinocytes transduced with control empty virus or PKP-1–Myc and labeled with indicated antibodies against plakoglobin (PG), Dsg3 or desmoplakin (DP). Images are representative of two experiments. Scale bar: 500 nm. (B) Histograms of the plaque-to-plaque distance measured in control (solid) and PKP-1–Myc (open). (C) Box-and-whisker plot of axial plaque-to-plaque distance of all protein domains analyzed in control (solid) and PKP-1–Myc overexpressing (striped) cells. The box represents the 25–75th percentiles, and the median is indicated. The whiskers show the 10–90th percentiles (for B,C, control: PG N-term, n=14; Dsg3 C-term, n=33; DP N-term, n=50; DP rod, n=74; DP C-term, n=54; for PKP-1–Myc: PG N-term, n=19; Dsg3 C-term n=47; DP N-term n=20; DP rod n=61; DP C-term n=43). *P<0.05, **P<0.0001; n.s., not significant (paired t-tests). (D) Desmosome length (mean±s.e.m., control: PG N-term, n=81; DP rod, n=116. PKP-1–

Myc: PG N-term, n=90; DP rod, n=95) measured for the plakoglobin N-terminal and desmoplakin rod domains in control (solid) and PKP-1–Myc overexpressing (striped) cells. *P<0.05 (paired t-tests).

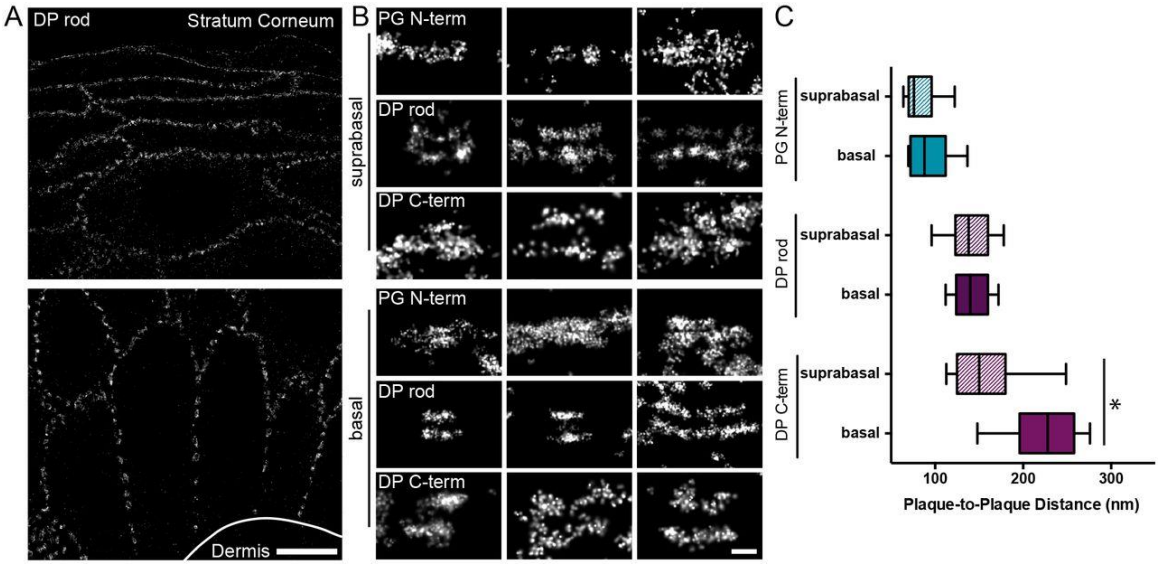

Figure 9. Molecular organization of desmosomes in human skin. (A) Human skin sections labeled for desmoplakin (DP, rod domain) with multiple desmosomes visible throughout the epidermis in basal (bottom) and suprabasal (top) cells. Scale bar: 5 µm. (B) Representative images of individual desmosomes labeled with the indicated antibodies from basal (bottom) and suprabasal (top) cells. PG, plakoglobin. Scale bar: 200 nm. (C) Box-and-whisker plot of plaque-to-plaque distance in basal (solid) and suprabasal (striped) cells. The box represents the 25–75th percentiles, and the median is indicated. The whiskers show the 10–90th percentiles (Basal: PG N-term, n=33; DP rod, n=80; DP C-term, n=29. Suprabasal: PG N-term, n=17; DP rod, n=34; DP C-term, n=12). *P<0.05 (paired t-tests).

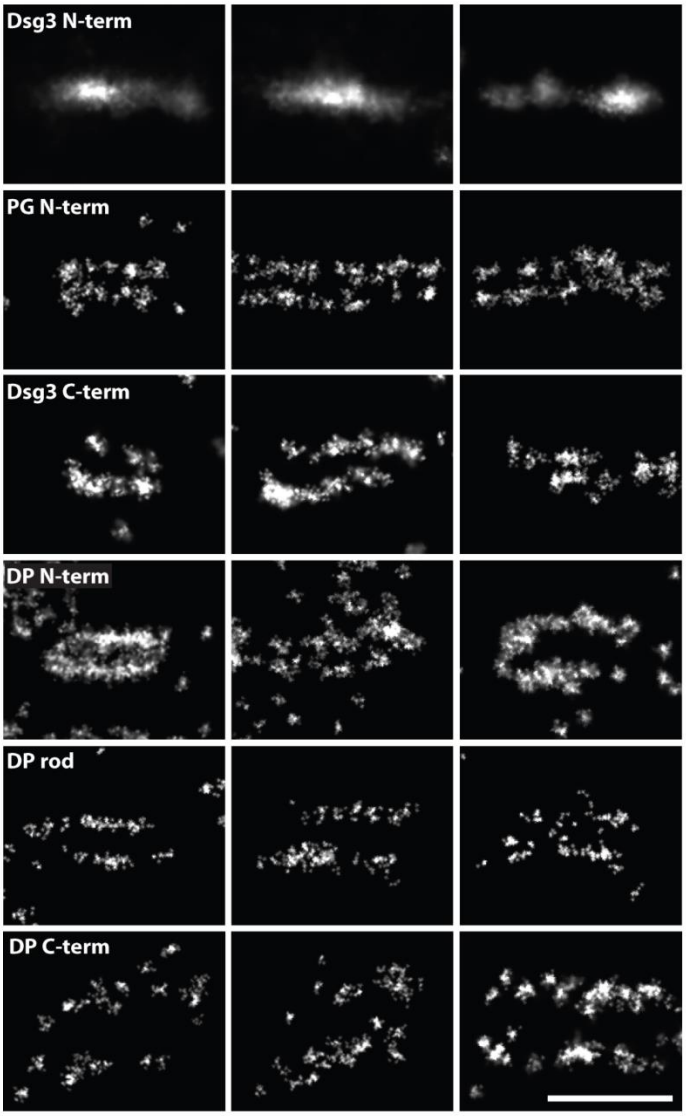

Supplemental Figure 1. Desmosomes imaged by dSTORM. Additional images of individual desmosomes from the population analyzed in Figure 7. Primary human keratinocytes were labeled with antibodies for specific protein domains Dsg3 N-term, PG N-term, Dsg3 C-term, DP N-term, DP rod, and DP C-term and imaged by dSTORM. Scale bar, 500 nm.

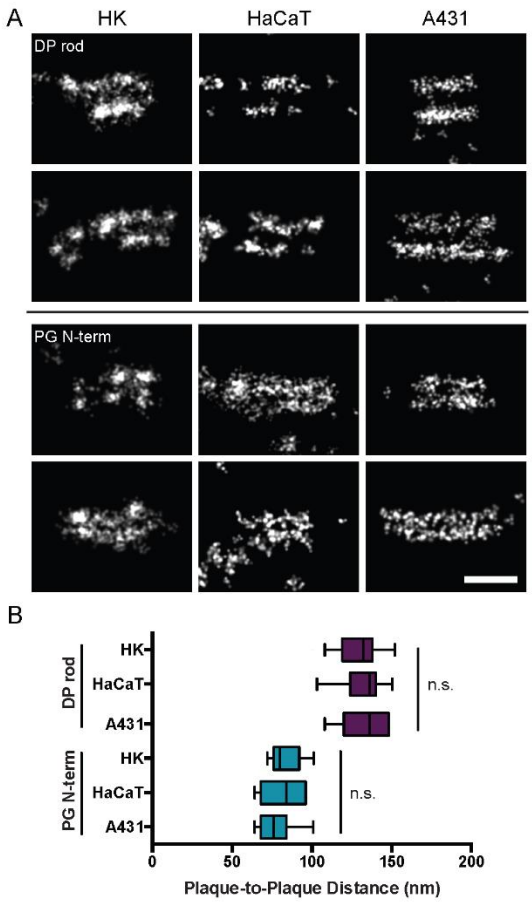

Supplemental Figure 2. Desmosomal plaque arrangement in multiple cell types. Primary human keratinocyte (HK), A431, and HaCaT cells were stained for plakoglobin (PG N-term) or desmoplakin (DP rod) and imaged by dSTORM. A) Examples of individual desmosomes labeled with DP rod (top) and PG N-term (bottom). Scale bar is 200 nm. B) Mean plaque-to-plaque distance (±SEM) for all desmosomes analyzed. There is no significant difference between cell lines for either DP rod or PG N-term as determined by ANOVA and Sidak's multiple comparisons test.

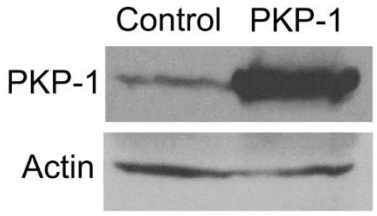

Supplemental Figure 3. PKP-1 protein levels. Primary human keratinocytes were transduced with either empty (control) or PKP-1—Myc adenovirus and PKP-1 and actin were measured by immunoblot. PKP-1 expression increased ~8 fold following viral transduction.

Protein Target	Name	Antibody Name	Species/Type	Dilution	Reference or Source
Desmoglein 3	Dsg3 N-term	AK15	Mouse monoclonal	1:100	(Tsunoda et al., 2003)
	Dsg3 C-term	G194	Mouse monoclonal	neat	Progen Biotechnik GmbH, Heidelberg
Plakoglobin	PG N-term	H-80	Rabbit polyclonal	1:50	Santa Cruz SC-7900
Desmoplakin I and II	DP N-term	NW161	Rabbit polyclonal	1:200	(Bornslaeger et al., 1996)
	DP rod	DP12 Clone 2.15	Mouse monoclonal	1:100	Fitzgerald Industries
	DP C-term	NW6	Rabbit polyclonal	1:250 or 1:1000	(Angst et al., 1990)

Supplemental Table 1. Primary antibodies used in dSTORM imaging.

	Plaque-to-Plaque (nm)			Length (nm)			
Protein Domain	**Mean**	**SD**	**SEM**	**Mean**	**SD**	**SEM**	**n**
Dsg3 N-term	--	--	--	300	111	13	69
PG N-term	94	14	2	307	83	12	47
Dsg3 C-term	112	40	7	358	92	16	32
DP N-term	128	35	6	387	99	17	36
DP rod	160	23	4	402	126	24	28
DP C-term	235	44	7	541	134	21	40

Supplemental Table 2. Plaque-to-plaque distance and desmosome length in primary human keratinocytes.

	Plaque-to-Plaque (nm)				
Protein Domain	**Treatment**	**Mean**	**SD**	**SEM**	**n**
PG N-term	**Control**	86	22	6	14
	PKP-1—Myc	84	33	7	19
Dsg3 C-term	**Control**	106	27	5	33
	PKP-1—Myc	92	12	2	47
DP N-term	**Control**	121	40	6	50
	PKP-1—Myc	114	40	9	20
DP rod	**Control**	139	25	3	74
	PKP-1—Myc	103	21	3	61
DP C-term	**Control**	231	31	4	54
	PKP-1—Myc	187	56	9	43

Supplemental Table 3. Plaque-to-plaque distance in PKP-1—Myc overexpressing compared to control cells.

	Length (nm)				
Protein Domain	**Treatment**	**Mean**	**SD**	**SEM**	**n**
PG N-term	**Control**	344	129	14	81
	PKP-1—Myc	508	258	27	90
DP rod	**Control**	379	138	13	116
	PKP-1—Myc	598	236	24	95

Supplemental Table 4. Desmosome length in PKP-1—Myc overexpressing compared to control cells.

	Plaque-to-Plaque (nm)				
Protein Domain	**Region**	**Mean**	**SD**	**SEM**	**n**
PG N-term	**Suprabasal**	84	20	5	17
	Basal	96	28	5	33
DP rod	**Suprabasal**	138	28	3	34
	Basal	140	26	5	80
DP C-term	**Suprabasal**	160	45	13	12
	Basal	225	48	9	29

Supplemental Table 5. Plaque-to-plaque distance in suprabasal and basal cells in human skin.

Chapter 5

Desmoglein 3 Order and Dynamics in Desmosomes Determined by Fluorescence Polarization Microscopy

This chapter adapted from:

Bartle, E.I., T.M. Urner, S.S. Raju, and A.L. Mattheyses. 2017. Desmoglein 3 Order and Dynamics in Desmosomes Determined by Fluorescence Polarization Microscopy. *Biophysical journal*. 113:2519-2529

5.1 Introduction

Many critical cellular functions including nuclear transport, ATP synthesis, and cell adhesion are orchestrated by large, multi-protein assemblies (Beck and Hurt, 2017; Gumbiner, 1996; Xu et al., 2015). These macromolecular complexes are defined by their protein composition, architecture, and cellular localization. Importantly, how proteins are arranged within each complex confers function. This protein arrangement can be described in two ways: spatial organization, which defines the location of proteins within a complex and orientational organization, which defines the order or particular arrangement of proteins relative to one another. Generation of order and disorder is a mechanism central to the assembly, disassembly, and function of many macromolecular complexes (Atkinson et al., 2013; McQuilken et al., 2015; Mouritsen and Jorgensen, 1994).

Cell junctions are macromolecular complexes that have roles in tissue integrity, communication, and barrier function. Desmosomes are epithelial cell-cell junctions that play a critical role in the skin and heart, where they are essential for maintaining tissue integrity (Garrod and Chidgey, 2008). Disruption of desmosomal function results in a number of human diseases, including skin blistering diseases, cancers, and cardiomyopathies (Brooke et al., 2012; Kowalczyk and Green, 2013). The dynamics of desmosome assembly, disassembly, and the transition between calcium-dependent and independent adhesion play a central role in many processes including keratinocyte migration during wound healing, embryogenesis, disease pathogenesis, and tissue remodeling (Garrod and Chidgey, 2008; Garrod et al., 2005; Green et al., 2010; Merritt et al., 2002; Wallis et al., 2000).

Structurally characterizing desmosomes presents a challenge, due to their biochemical intractability, complex structure spanning two cells, and functional dynamics. The organization

of proteins in the plaque has been determined by electron microscopy (EM) and super-resolution direct stochastic optical reconstruction microscopy (dSTORM) (North et al., 1999a; Stahley et al., 2016a). Through these methods, differences in protein spatial organization have been correlated with changes in adhesion. However, the dynamics of desmosome structure, including protein ordering, as it relates to function are still poorly understood.

The desmosomal adhesive junction is symmetrical across the intermembrane space, with each cell contributing half the complex. Desmosomal cadherins (desmogleins and desmocollins) are single pass transmembrane glycoproteins with extracellular domains that interact to form the adhesive interface (Patel et al., 2003). This adhesion involves trans-binding through a strand swap, where a conserved tryptophan (Trp2) is inserted into a hydrophobic pocket of the opposing cadherin (Lowndes et al., 2014; Sivasankar, 2013). Desmosomal cadherins are characterized by their calcium-dependent structure, with calcium binding sites between cadherin repeat domains. The intracellular plaque proteins create a dense network linking the cadherin cytoplasmic tails to the intermediate filament cytoskeleton (Getsios et al., 2004). Each desmosome contains many copies of each of these proteins, resulting in an overall structure approximately 0.5 μm in diameter (Tamarin and Sreebny, 1963) with the plaque extending between 100-115 nm (Stahley et al., 2016a) into the cytoplasm.

Since cadherins are the proteins responsible for spanning neighboring cells, understanding their structure and organization is central to our understanding of adhesion. The extracellular domain of the desmosomal cadherins has largely been hypothesized to be ordered, based on EM (Al-Amoudi et al., 2007; Garrod et al., 2005; North et al., 1999a) and *in vitro* characterization of individual cadherin structure (Boggon et al., 2002). Evidence for order includes the dense midline seen in EM and the periodicity of electron densities by tomography

(Al-Amoudi et al., 2011; Al-Amoudi et al., 2007; Al-Amoudi et al., 2005; Garrod et al., 2005; Rayns et al., 1969). Taken together this suggests that desmosomes are ordered and that the cadherins are potentially arranged in a crystalline-like manner. However, not all studies reach a similar conclusion and conflicting results describe the cadherins as a disordered "tangled knot" (He et al., 2003).

One drawback to the methods used to study desmosome ultrastructure is that they require the use of fixed and processed cells or tissue, and therefore cannot capture structural dynamics. To address this and characterize order of the adhesive interface in living cells, we turned to fluorescence polarization. Fluorescence polarization has been used to study single molecule dynamics (Boggon et al., 2002; Weber, 1953), diffusion (Weber and Anderson, 1969), binding events (Kierszenbaum et al., 1969; Yin and Stern, 2014) and, when combined with microscopy, organization of biological structures (Axelrod, 1979; Kampmann et al., 2011; Vrabioiu and Mitchison, 2006). Fluorescence polarization is a powerful tool to study the order and disorder of proteins in macromolecular complexes including yeast septins (DeMay et al., 2011), nuclear pore complex (Atkinson et al., 2013; Mattheyses et al., 2010), MHC complex (Kress et al., 2011; Rocheleau et al., 2003), and the cytoskeleton (McQuilken et al., 2015; Mehta et al., 2016; Valades Cruz et al., 2016).

Herein, we present an excitation resolved fluorescence polarization microscopy approach to measure order of the desmosomal cadherin desmoglein 3 (Dsg3) in living cells. First, we introduce the approach we developed to address the question of order vs. disorder in desmosomes and establish the upper and lower bounds on detecting order with simulations. We then show that the extracellular domain of Dsg3 is ordered at the single desmosome, single cell, and population level, in contrast to a series of disordered controls. Finally, we reveal the

dynamics of Dsg3 order loss relative to loss of adhesion, demonstrating a direct relationship between order and function. Our results confirm the relevance of cadherin ordering to desmosome structure and adhesive strength.

5.2 Results

To investigate protein order in the desmosome adhesive interface, we selected a representative cadherin from the seven desmogleins and desmocollins in the family. We focused on Dsg3 because of its high expression level in the lower layers of the skin, where it is critical for keratinocyte adhesion. This function is highlighted by the skin blistering disease Pemphigus Vulgaris, in which adhesion is weakened by autoantibodies targeted to the extracellular domain of Dsg3 (Amagai, 1999; Amagai et al., 1991; Saito et al., 2012).

To create a polarization probe, we needed a fluorophore to report the orientation of the Dsg3 extracellular domain. We chose to replace the most membrane proximal extracellular anchor (EA) domain of Dsg3 with GFP (Dsg3-ΔEA-GFP). We generated a ribbon diagram of the Dsg3-ΔEA-GFP ectodomain based on the crystal structures of GFP (Brejc et al., 1997) and Dsg3 extracellular domains 1-4 (EC1-4) (Harrison et al., 2016), the orientation of the transition dipole moment (μ) within GFP (Rosell and Boxer, 2003), and secondary structure predictions of the linker regions (Fig. 10a). In Dsg3-ΔEA-GFP, GFP is tethered between the EC4 domain and the plasma membrane. This constricted association is essential for the orientation of μ, which will be probed by polarized excitation, to reflect the protein orientation.

To determine whether proteins are ordered, we must first set up a coordinate system as a frame of reference in which to study Dsg3. The orientation of μ is defined by the azimuthal (α) and polar (tilt; β) angles in the microscope coordinate system (Fig. 10b), where the Dsg3 extracellular domain will dictate the orientation of GFP. In a single desmosome there will be

multiple copies of Dsg3-ΔEA-GFP within a point spread function. Protein order within this volume is represented by the average of the transition dipole moments and can be measured using excitation resolved polarized fluorescence microscopy (Oldenbourg, 2013; Valades Cruz et al., 2016). If Dsg3-ΔEA-GFP is ordered in a single desmosome, the fluorescence intensity will be modulated by the excitation polarization (Fig. 10c). In contrast, if Dsg3-ΔEA-GFP is disordered, the intensity will be independent of excitation polarization (Fig. 10d).

5.2.1 Theory of protein order in desmosomes

We established the theoretical capabilities of excitation resolved polarization fluorescence microscopy to distinguish between protein order and disorder in desmosomes. In our approach, images are acquired at four unique excitation polarizations (0°, 45°, 90°, and 135°) (DeMay et al., 2011). To measure order, we calculate the amplitude of intensity modulation as a function of excitation polarization, which we call order factor:

$$Order\ Factor = \sqrt{(I_0^{norm} - I_{90}^{norm})^2 + (I_{45}^{norm} - I_{135}^{norm})^2} \qquad \text{(Eq. 3)}$$

where I_ω^{norm} is the intensity from a single excitation polarization (ω) normalized across all excitation polarizations (see methods). Order factor represents the average dipole orientation within a pixel.

To determine the impact of experimental variables on our ability to measure order, we ran Monte Carlo simulations of raw fluorescence intensity data incorporating photon noise for all possible orientations (α, β) and a range of signal-to-background ratios (S/B) (Fig. 11a). These simulations show that order factor for an ordered system depends heavily on tilt angle (β) and S/B. Order factor at a given S/B was always maximum when the average dipole is entirely in the imaging plane (β=90°). The dipole orientation in the imaging plane (α) has a negligible impact on order factor, and the calculations represent averages over all α (Supplemental Fig. 4). To

determine the impact of noise on our ability to measure order, we examined the distribution of theoretical order factors across simulations for β=90°. At the lowest S/B, where noise is expected to have the biggest impact, the order factor variance was 0.0023 while the range of the distribution was 0.23 (Fig. 11b). Both the range and the variance decreased exponentially as S/B increased. Taken together this data demonstrates the robustness of order factor to photon noise, while illustrating the full range of order factors that can be measured from an ordered system.

Next, we determined the range of order factors likely to be measured from a disordered system, in which intensity does not depend on excitation polarization. We ran Monte Carlo simulations where ($I_0 = I_{45} = I_{90} = I_{135}$) and used our lowest experimentally measured signal levels as inputs to assess the "worst case" signal to noise ratio (Fig. 11c). These simulations were critical to determine the threshold at which order and disorder become indistinguishable. We defined the "disorder threshold" to be two standard deviations above the mean of this distribution. Order factors below this threshold (0.2) cannot be distinguished from a disordered system.

One consideration is that a subset of ordered systems will report an order factor below the disorder threshold (cyan on the order factor heatmap; Fig. 11a) due to the dependence of order factor on dipole orientation and S/B. The percent of (α, β) orientations that have order factors below the disorder threshold is 25% at the lowest S/B and decreases rapidly to less than 1% as S/B increases, regardless of absolute background level (Fig. 11d). This means that the number of false negatives or "undetectable" (α, β) orientations decreases as S/B improves.

From the above simulation results, we set the theoretical upper bound on order factors likely to be measured from an ordered system (red line) and the disorder threshold (blue line)

(Fig 11e). Experimental order factors between the upper bound and the disordered threshold are the result of an ordered system.

5.2.2 Desmoglein 3 extracellular domain is ordered

After establishing order factor as a metric, we applied this approach to measure order in desmosomes. We designed two Dsg3-GFP chimeric proteins: Dsg3-ΔEA-GFP to measure Dsg3 order (Fig. 10a), and Dsg3-link-GFP as a disordered control. In Dsg3-link-GFP, the C-terminus was tagged with a flexible linker followed by GFP, which allows GFP conformational freedom relative to Dsg3 i.e. the orientation of GFP does not reflect the orientation of the Dsg3 ectodomain.

To confirm that Dsg3-ΔEA-GFP and Dsg3-link-GFP localize properly to desmosomes, we transfected the constructs into HaCaT cells, a human keratinocyte cell line. HaCaT cells are an ideal immortalized cell line for the characterization of desmosome structure and function, as they are non-tumorous and are a good model of primary human keratinocytes (Sprenger et al., 2013). The cells were fixed and labeled with antibodies to the endogenous obligate desmosomal protein desmoplakin. To remove soluble, non-desmosomal Dsg3, the cells were pre-extracted prior to fixation (Palka and Green, 1997). Dsg3-ΔEA-GFP and Dsg3-link-GFP both co-localized with desmoplakin in punctate structures at cell-cell borders, indicating proper localization to desmosomes (Supplemental Fig. 5).

To determine if the extracellular domain of Dsg3 is ordered, we imaged HaCaT cells transfected with Dsg3-ΔEA-GFP using fluorescence polarization microscopy (Fig. 12a). As expected for an ordered system, the fluorescence intensity at cell-cell junctions was dependent on the excitation polarization. We developed a custom MATLAB image analysis program to calculate the pixel-by-pixel order factor using Eq. 3 within a binary mask defining desmosomes

(Fig. 12a; Supplemental Fig. 6). We quantified this data by plotting the order factor of every pixel in a cell border region of interest (ROI) as a function of S/B. This revealed that 93% of the pixels fall within the upper and lower bounds for an ordered system. A z-stack analysis showed order factor was not impacted by focal plane or contributions from out of focus light (Supplemental Fig. 7).

Next, we imaged HaCaT cells transfected with the control probe Dsg3-link-GFP (Fig. 12b). Though Dsg3-link-GFP localized to desmosomes, the intensity was not dependent on the excitation polarization angle, as expected for a disordered system. The order factor was below the disorder threshold for the majority of the pixels within the cell border ROI (95%). This indicates that GFP in Dsg3-link-GFP is disordered, and that desmosomal targeting alone is not sufficient to confer order.

To confirm plasma membrane targeting does not result in order, GFP with a palmitoylation motif (mem-GFP) was transfected into HaCaT cells (Fig. 12c). The intensity of mem-GFP was not dependent on the excitation polarization, and the majority of pixels within the ROI fell below the disordered threshold (99%). This demonstrates that plasma membrane targeting is not sufficient to confer order. Finally, for a well-characterized randomly oriented control, GFP was transfected into HaCaT cells (Fig. 12d). There was no dependence of GFP intensity on excitation polarization, and the majority of pixels within the ROI were below the disorder threshold (98%).

We next asked if the single cell order factors were representative of the population. The whole cell average Dsg3-ΔEA-GFP order factors cluster within the theoretical bounds we determined for an ordered system (Fig. 12e). This population contained a mixture of cell borders, the majority between transfected and non-transfected cells (Fig 12a), and some between two

transfected cells (Supplemental Fig. 8). The order factor of borders between two transfected cells fell within the distribution of those measured for single transfected cell borders.

The average order factors for all cells expressing Dsg3-link-GFP, mem-GFP, and GFP fell below the disorder threshold, regardless of S/B. We noted a spread in the distribution of mean order factor within the Dsg3-ΔEA-GFP cell population, as would be expected for an ordered system based on our modeling. This variability can be explained by differences in orientation (α, β) and S/B, however we cannot rule out additional contributions from biological differences between cells.

Importantly, when interrogated with the binary question is the system ordered or disordered, individual cells report the same answer as the population. The Dsg3-ΔEA-GFP order factor, 0.38 ± 0.11 (n=29) was significantly larger than those for the controls Dsg3-link-GFP (0.12 ± 0.025; n=17), mem-GFP (0.097 ± 0.018; n=17), and GFP (0.073 ± 0.020; n=11) by one-way ANOVA (Fig. 12f). Taken together, these data reveal that the extracellular domain of Dsg3 is ordered in desmosomes.

5.2.3 Dsg3 order decreases prior to loss of cell adhesion

Next, we investigated if Dsg3 order is related to adhesive function. Desmosome adhesive strength is calcium-dependent and when calcium is depleted from calcium-dependent keratinocytes adhesion is disrupted (Penn et al., 1987). Therefore, we used a calcium switch assay where the calcium concentration is reduced from normal (~3mM) to low (~0.03mM) to disrupt desmosome function.

To quantify the average desmosome strength for a cell population and the dynamics of loss of adhesion we employed a dispase cell fragmentation assay. Fragmentation of a confluent cell sheet resulting from applied mechanical stress increased with time in low calcium media

(n=8) (Fig. 13a). This fragmentation is inversely proportional to adhesive strength. We quantified the rate of loss of adhesion by fitting the fragment number to an exponential growth with a rate constant of 15.1 min (R^2= 0.97) (Fig. 13b).

We next wanted to establish the baseline dynamics of desmosome order over the 30 min time frame identified in the functional assay. To provide an independent marker for desmosome identification and tracking, desmoplakin-mCherry (DP-mCherry), was co-transfected into HaCaT cells with Dsg3-ΔEA-GFP.

Comparing images from a representative cell at 0 and 30 min revealed that Dsg3-ΔEA-GFP and DP-mCherry co-localization, cell morphology, and order factor were stable when a normal calcium level was maintained (Fig. 14a). Desmosome morphology remained unchanged, and individual co-localized puncta with consistent order factors can be identified and tracked across multiple time points (Fig. 14b). To control for photobleaching which results in a loss of intensity, and thus a change in S/B, we modeled a projected order factor based on the order factor at 0 min, Dsg3-ΔEA-GFP intensity, and background levels throughout the time course. The projected order factor accurately predicted the experimental order factor over the time course, and the two were not significantly different at each time point by two-way ANOVA with Sidak's comparison ($p>0.11$) (Fig. 14c). The accuracy of this prediction shows that projected order factor is robust. Pixel-by-pixel order factor remained above the disorder threshold over the 30 minutes (Fig. 14d).

To measure Dsg3 order during loss of adhesion, Dsg3-ΔEA-GFP and DP-mCherry were transfected into HaCaT cells and imaged before and after a calcium switch. A representative cell shows co-localization of DP-mCherry and Dsg3-ΔEA-GFP both pre (t = 0 min) and post (t = 30 min) calcium switch, indicating co-localization was maintained throughout the experiment (Fig

14e). Morphological changes are apparent when comparing the cell pre- and post-calcium switch, including cell rounding and altered junctions (Fig. 14e; top). Following the calcium switch, Dsg3-ΔEA-GFP shifted from ordered (t=0 min) to disordered (t=30 min) (Fig. 14e; bottom).

To more closely examine the dynamics of this process, we monitored a representative ROI containing a single cell-cell border (Fig. 14f). For the first 10 min post-switch puncta are clearly identifiable at the cell border. In contrast, by 25 min the cell border has a dramatically different morphology, though Dsg3-ΔEA-GFP co-localization with DP-mCherry remains throughout. In this individual border, order factor decreased within the first 2 min post calcium switch, when puncta localization and morphology were not obviously altered. This decrease in order factor was fit to an exponential decay with a rate of 5.5 min ($R^2 = 0.94$) (Fig. 14g).

Desmosomal Dsg3 level can decrease during disassembly due to diffusion of the protein in the plasma membrane or protein recycling through endocytosis, both of which would lead to a decrease in fluorescence intensity and S/B (Calkins et al., 2006; Delva et al., 2008; Garrod and Chidgey, 2008). As expected during disassembly, projected order factor decreased over the time course due to the changes in S/B, however it remained above the disorder threshold (Fig. 14g). The experimental and projected order factors exhibited distinct behaviors, with measured order factor decreasing exponentially and more rapidly than the projected linear decrease, leading us to conclude that there was a decrease in the order of Dsg3-ΔEA-GFP as a result of the calcium switch.

To quantify the transition from ordered to disordered over time, we plotted pixel-by-pixel order factor as a function of S/B for the ROI (time progresses from dark to light blue; Fig. 14h). The percent of individual pixel order factors below the disorder threshold increased over the time

course from 0% (0 min) to 87% disordered (30 min). We further quantified order factor on a single desmosome level. This revealed possible heterogeneity in order dynamics at early time points between the desmosomes from a single cell. Loss of order from individual desmosomes is smooth on the timescale of our experiments (Supplemental Fig. 9).

To confirm that changes in cell and desmosome morphology were not dependent on the construct, we imaged HaCaT cells transfected with Dsg3-link-GFP and DP-mCherry before and after a calcium switch (Supplemental Fig. 10). Dsg3-link-GFP co-localized with DP-mCherry at all time points. Similar morphological changes were observed to those noted in the Dsg3-ΔEA-GFP transfected cell in the calcium switch assay. However, as expected, the average order factor was consistently below the disorder threshold at all time points.

Next, we wanted to determine if order loss followed similar kinetics in the population as in single cells. For the control conditions (Dsg3-ΔEA-GFP in normal calcium media, n=6; and Dsg3-link-GFP in low calcium media, n=4), the average experimental and projected order factors fit a linear regression (Fig. 14i), with no significant difference by two-way ANOVA. These results show that the population order factor was maintained throughout the time course for each control and fit the theoretical model.

In contrast, the average experimental order factor after calcium switch for Dsg3-ΔEA-GFP for a population of cells decreased exponentially (n = 8). These dynamics were significantly different from the average projected order factor at each time point demonstrating that the decrease in order factor reflects a structural change within the desmosome, not declining S/B. Loss of order was rapid, with a significant decrease in order factor between t=0 min and t=2 min ($p=0.0003$, n=8; by two-way ANOVA with Sidak's multiple comparison test). To quantify the rate of Dsg3-ΔEA-GFP loss of order, the time course for the population of cells was fit to an

exponential with a decay rate of 4.5 min (R^2= 0.97). The rate of loss of order is faster than the rate of fragmentation (15.1 min), showing that loss of Dsg3 order is upstream of the loss of adhesion.

5.3 Discussion

Desmosomes play a critical role in the maintenance of tissue integrity and their dysfunction is implicated in human diseases including cardiomyopathies, skin blistering diseases, and cancers (Broussard et al., 2015). Therefore, the relationship between desmosome structure and adhesive function is of much interest. There is debate in the field over how the desmosomal cadherins are organized and if the organization of these proteins is important for adhesive function. Here, we applied fluorescence polarization microscopy to study desmosome structure, and found that the extracellular domain of the cadherin Dsg3 is ordered in living cells. Furthermore, we found that order is a dynamic state: order is lost when calcium is depleted, ultimately resulting in the loss of cell adhesion.

Previous work using EM to study desmosomal cadherins in the extracellular space has conflicting results. Al-Amoudi et al found an ordered structure, and hypothesized the desmosomal cadherins form a repeating array (Al-Amoudi et al., 2007; Al-Amoudi et al., 2005). In contrast, the less ordered “tangled knot” described by Stokes et al fit many cadherin orientations within a single desmosome (He et al., 2003). These differences could be due to several factors including imaging method, sample fixation, tissue type, or adhesive state. In the experiments presented here order is measured in living cells, eliminating any potential artifacts due to fixation. Desmosome adhesive state is well understood to be either calcium-dependent or hyper-adhesive (calcium-independent) (Garrod et al., 2005; Windoffer et al., 2002).

Fluorescence polarization revealed the Dsg3 extracellular domain is ordered in calcium-dependent cells.

Order factor offers a readout for desmosome structural organization, but it does not indicate the ultrastructure conveying the order. A single desmosome is close in size to the diffraction limit and many copies of Dsg3 in a single desmosome contribute to an ensemble average dipole orientation. Complete disorganization of dipoles in the *x-y* plane will result in an order factor below the disordered threshold. If all dipoles possess a single orientation (α, β), order factor is impacted by β (Fig 10c) and to a lesser extent by α (Fig S1). Interestingly, cadherins could adopt multiple orientations in one desmosome, but still form an ordered array. Our approach is currently unable to discriminate between a single cadherin orientation, two or more distinct repeating orientations, or a circularly symmetric order (Beck and Hurt, 2017).

Influences on order factor can be grouped into two categories: experimental and structural. In this work, we modeled the experimental impacts including S/N and background level and showed we can measure order factor with confidence under our experimental conditions. We have also developed methods to distinguish changes in order factor brought on by structural dynamics rather than experimental factors (i.e. decreasing S/B from photobleaching or loss of protein). Several biological factors could introduce variations in cadherin dipole orientations (α, β) in a desmosome. These include, but are not limited to, nanoscale fluctuations in membrane curvature, trans-binding dynamics, protein wobble, and changes in plaque arrangement. These factors would decrease the average dipole and be detected as a decrease in the order factor.

It has been demonstrated that the tertiary structure of Dsg3 relies on calcium binding between the extracellular domains (Harrison et al., 2016) to maintain rigidity, similar to the

classical cadherins. Interestingly, this rigidity may not be essential to maintain adhesion. Molecular dynamics simulations by Sotomayor and Schulten of classical C-cadherin suggest that trans-binding could be maintained in the absence of calcium (Sotomayor and Schulten, 2008). Experimentally, Kim et al used FRET to distinguish two phases of N-cadherin conformational changes, including a "sudden, but partial loss" of binding, after removal of calcium (Kim et al., 2011). While desmosomal cadherins are similar to classical cadherins, the role of calcium in the adhesive function of Dsg3 and the direct impact of its loss on quaternary structure of the complex has been largely unexplored. We showed that order decreases within 2 minutes of removing calcium, indicating that Dsg3 conformation is calcium dependent in desmosomes. Intriguingly, in this time frame Dsg3 adhesive function is not yet lost. This difference in dynamics indicates that loss of order is upstream of loss of adhesion and supports the molecular dynamics showing that trans-binding is not calcium dependent (Sotomayor and Schulten, 2008). Our data shows there is a loss of Dsg3 order while trans-binding is maintained, followed by a loss of adhesive function similar to the two-phase dynamics measure by FRET (Kim et al., 2011). We propose that loss of cadherin order in response to calcium depletion leads to a cascade of events that culminates in the loss of trans-binding and cell adhesion.

Fluorescence polarization microscopy allows us to quantify structural dynamics in living cells. In contrast, previous methods for studying desmosome organization were entirely dependent on static, fixed samples. Implementation of fluorescence polarization involves a straightforward and inexpensive modification to an existing fluorescence microscope. The experimental and analysis methods used here do not depend on the symmetry of the complex or its orientation within a cell and can be easily applied to other cell junctions or macromolecular complexes. We believe this approach to studying desmosome structure will continue to be

invaluable for exploring cadherin order in different functional states and disruption in human disease.

5.4 Materials and Methods

Cell culture

The human immortalized keratinocyte cell line HaCaT (Addex Bio, San Diego CA) was cultured in Dulbecco's modified Eagle's medium (DMEM) supplemented with 2mM L-glutamine, 10% FBS, 100 U/mL Pen/Strep, and 2.5ug/mL Amphotericin B and maintained at 37°C and 5% CO_2. For imaging, cells were seeded into 8-well #1.5 coverslip bottom dishes (Ibidi, Madison, WI), transfected, and imaged in supplemented FluoroBrite DMEM. For fragmentation assays, cells were grown to confluence in 12 well tissue culture plates.

Cloning and constructs

Dsg3-ΔEA-GFP was cloned using PCR and mutagenesis to insert the EGFP sequence between residues K499 and L615 of mouse Dsg3 (Uniprot: O35902). Dsg3-link-GFP was cloned with the same methods, with the flexible linker ID$(GGGGS)^{x5}$TG ligated between the C-terminus of mouse Dsg3 and N-terminus of EGFP. Desmoplakin-GFP was a gift from Kathleen Green (Addgene plasmid #32227). The GFP was replaced with mCherry using PCR, to create DP-mCherry. Mem-GFP is EGFP with the N-terminal palmitolyation motif, LCC. All cloning was performed by the Emory Cloning Core and verified by sequencing.

Dsg3-ΔEA-GFP ribbon diagram

Diagraming of Dsg3-ΔEA-GFP was performed in the software "UCSF Chimera" using Dsg3 (EC1-4) (PDB:5EQX) and GFP (PDB:1EMB) The 18 AA linker (VPDFNENCPSVVLEKMVS) between the end of 5EQX (EC4 of Dsg3) and the start of GFP is

comprised of the EC4-EC5 Dsg3 linker region and the start of 1EMB. The linker secondary structure was predicted using “PredictProtein”, PROFphd method (Yachdav et al., 2014). The C-terminal of 1EMB is linked to the amino acids TGMDELYKAAIGLILLGLLMLLLAPLLLL from Dsg3, where TGMDELYK is part of EC5 structure predicted to be α-helical by the same method used above. AAIGLILLGLLMLLLAPLLLL is the constitutive transmembrane domain of Dsg3 which “PredictProtein” correctly identified with the PHDhtm method.

The orientation of the chimeric protein was determined by embedding the transmembrane domain in a lipid bilayer and orienting EC1 such that it could engage in trans-binding. GFP was constrained by Dsg3, the plasma membrane, and the linker locations.

Transfection

HaCaT cells were transfected at 50% confluent using Lipofectamine 3000 following manufacturer's instructions. DNA concentration was optimized to 70ng per 1 cm^2. Cells were imaged 40-48 hours post-transfection.

Calcium switch

For imaging under low Ca^{2+} conditions, cells were switched from supplemented FluoroBrite DMEM with ~3mM Ca^{2+} to ~0.03mM Ca^{2+} as described by Wilson (Wilson, 2014) while on the microscope stage.

Fluorescence Polarization Microscopy

Fluorescence polarization microscopy was conducted using a Nikon Ti Eclipse microscope, equipped with a motorized stage, stage-top incubator to maintain 37°C and 5% CO_2 (Tokai Hit, INUBG2SF-TIZB) and a 60x 1.49NA objective. The 488 nm laser (Coherent) excitation passed through a cleanup polarizer, half-wave plate, and lens to focus on the back

focal plane (ThorLabs, Newton, NJ). Rotation of the half-wave plate with a motorized mount (PRM1Z8; ThorLabs) controlled the orientation of the excitation polarization. Images were captured with an ORCA-Flash 4.0 v2 CMOS camera (Hamamatsu). The system was controlled with Nikon Elements software. Images were acquired at 0°, 45°, 90°, and 135° excitation polarization.

Cell fixation and antibody staining

Fixation and labeling protocols are described in Stahley et al (Stahley et al., 2016a) with a 1 hr incubation in primary antibody and 30 min incubation in secondary antibody. Primary antibody was anti-desmoplakin (DPI/II clone 2.15; Abcam, Cambridege, UK).

Fragmentation Assay

Confluent, cell sheets were dissociated by incubating with 2U/mL Dispase II (Roche, Indianapolis, IN) in DMEM for 35-45 minutes. The intact monolayers were then transferred to 1.7mL Eppendorf tubes. Media was removed from the cell monolayer and replaced with 500 μL of either normal (~3mM Ca^{2+}) or low (~0.03mM Ca^{2+}) media and incubated for 2-30 minutes before agitation with an orbital shaker at 350 rpm for 2 minutes. The fragments were immediately fixed by adding 500 μL 16% paraformaldehyde and manually counted using a dissection microscope.

Theoretical Model

The probability of excitation of a fluorophore can be expressed as a dot product between the transition dipole moment, described in a spherical coordinate system by the azimuthal angle α and polar angle β, and the polarization of excitation light in the imaging plane (ω). The square of this product is proportional to the intensity of the fluorophore;

$$I_\omega = sin^2(\beta)cos^2(\alpha - \omega) \qquad \text{(Eq. 1)}$$

To determine the order factor, we first normalized the data pixel-by-pixel where I_ω is the intensity from an individual pixel $I_\omega = [I_0, I_{45}, I_{90}, I_{135}]$, as follows:

$$I_\omega^{norm} = \frac{I_\omega - min(I_\omega)}{max(I_\omega) - min(I_\omega)} \quad \text{(Eq. 2)}$$

Using the normalized intensities, we then calculated the amplitude of intensity modulation, which we define as order factor:

$$Order\ Factor = \sqrt{(I_0^{norm} - I_{90}^{norm})^2 + (I_{45}^{norm} - I_{135}^{norm})^2} \quad \text{(Eq. 3)}$$

Data analysis

A custom order factor image analysis program (Polarized Order Detection Software; PODS) was written in MATLAB (Mathworks, Natick, MA). Raw images were first corrected for uneven laser illumination and polarization-dependent intensity changes with the mean of three correction images, obtained by imaging a fluorescent slide at each polarization (Chroma, Bellows Falls, VT). Processed images were then corrected for photobleaching using fluorescence decay constants determined from control experiments with constant excitation polarization (GFP, 0.003; mCherry, 0.06) (DeMay et al., 2011). Next, a binary mask was generated to identify desmosomes. Corrected images were masked automatically using a morphological algorithm that first detects punctate objects with function imopen and a median filter. Next the binary mask is created using the threshold from greythresh followed by bwareaopen. In cases of high background variance the threshold was set manually. Pixel-by-pixel order factor was calculated within the binary mask for corrected images using the theoretical relationships described above in Eq. 1-3.

Computational Modeling

Using the relationships described above, mathematical modeling was performed in MATLAB using Monte Carlo method simulations of Poisson distributed noise with 100 repeats.

To determine relevant S/B range for simulations, intensity from pixels outside of the desmosome binary mask were averaged to calculate background for each image. The resulting pixel signals within the desmosomal region were averaged to obtain a signal estimate for each image. The range of modeled signal levels were taken from the range of experimental values. The three background levels represent average background over all data and one standard deviation above and below the average.

To determine a threshold above which order factor can be interpreted to mean true biological order, we modeled disorder at signal levels taken the lowest signal pixel of each image, which represent the most noise dominated signal values. The maximum calculated order factor from each simulation represents the worst case false positive for order. The threshold for disorder was set at two standard deviations above the mean of the distribution of maximum order factors resulting from a disordered system.

We calculated a projected order factor for the time lapse experiments to verify that the change in measured order factor in low calcium time course experiments was not due to protein loss and decreased S/B. First, simulations were conducted at the average S/B levels of every time point. Next, order factor pixel values from t_0 were matched to a theoretical orientation. In subsequent simulations, order factor values from these orientations and experimental signal and background levels were averaged to determine the theoretical order factor.

Statistics

All statistical analysis was done using Prism (GraphPad, La Jolla, CA). One-way ANOVA was used to test statistical significance across multiple experimental conditions (Fig. 12). Two-way ANOVAs were done on all data comparing two or more experimental conditions across time points (Fig. 14). Two-way ANOVA with Sidak's multiple comparisons was used to

determine the significance between experimental data and projected order at individual time points (Fig 14c). Curve fits were generated using Prism non-linear curve fitting functions for the exponential curves as indicated (Fig. 13, Fig. 14).

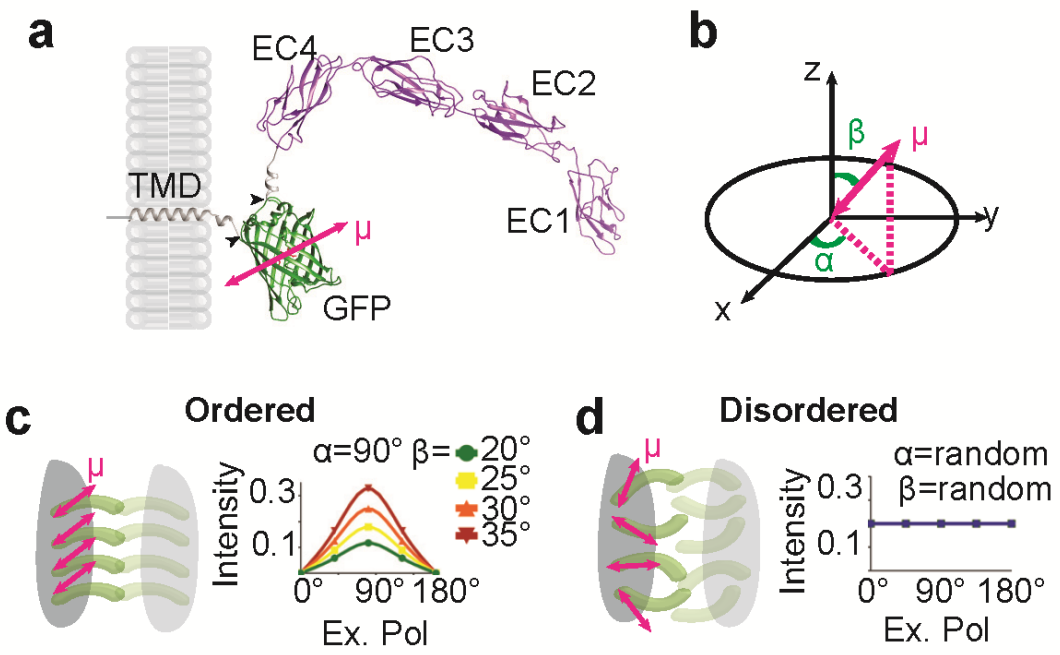

Figure 10. Polarization microscopy to study desmosome protein organization. (**a**) Ribbon diagram of the Dsg3-ΔEA-GFP chimeric protein. Dsg3 extracellular domains EC1-4 (purple) and GFP (green) with the EA domain deletion/GFP insertion sites indicated by black arrowheads and the transition dipole moment (μ) by the red double-headed arrow. (**b**) The fluorophore transition dipole (μ; red arrow) is described by azimuthal (α) and polar (β) angles in a spherical coordinate system where *x*-*y* is the imaging plane and *z* is the optical axis. (**c**) If Dsg3 is ordered, fluorescence intensity will be modulated by the excitation polarization, resulting in a sinusoidal curve with an amplitude dependent on the polar angle as shown for β = 20°, 25°, 30°, and 35°. (**d**) If Dsg3 is disordered, the fluorescence intensity will be constant regardless of the excitation polarization.

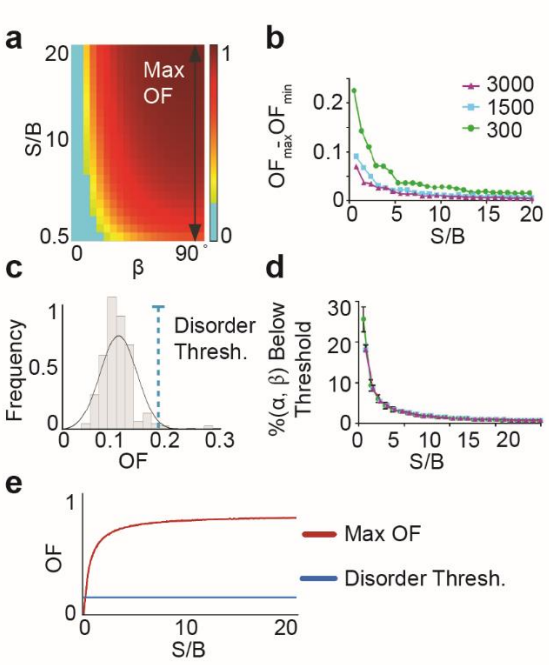

Figure 11. Computational modeling and derivation of order factor. (**a**) Theoretical average order factor calculated from Monte Carlo simulations at different S/B levels and β orientations averaged over all α (background = 1500 photons). The maximum order factor at each S/B occurs when μ is entirely in the imaging place (β = 90°). (**b**) Range of order factor (max-min) as a function of S/B (background = 300, green; 1500, blue; and 3000, purple). (**c**) Histogram of data from Monte Carlo simulations of disorder showing the maximum order factor resulting from experimental signal and background levels. The threshold for distinguishing order from disorder, shown here by the blue dashed line, was set at two standard deviations above the mean of this distribution. Order factors below this threshold are considered disordered and are shown in cyan on the order factor colormap. (**d**) Percent of (α, β) orientations with an order factor less than the disordered threshold as a function of S/B (background = 300, green; 1500, blue; and 3000, purple) (**e**) Theoretically determined maximum order factor as a function of S/B (red) and the disorder threshold (blue).

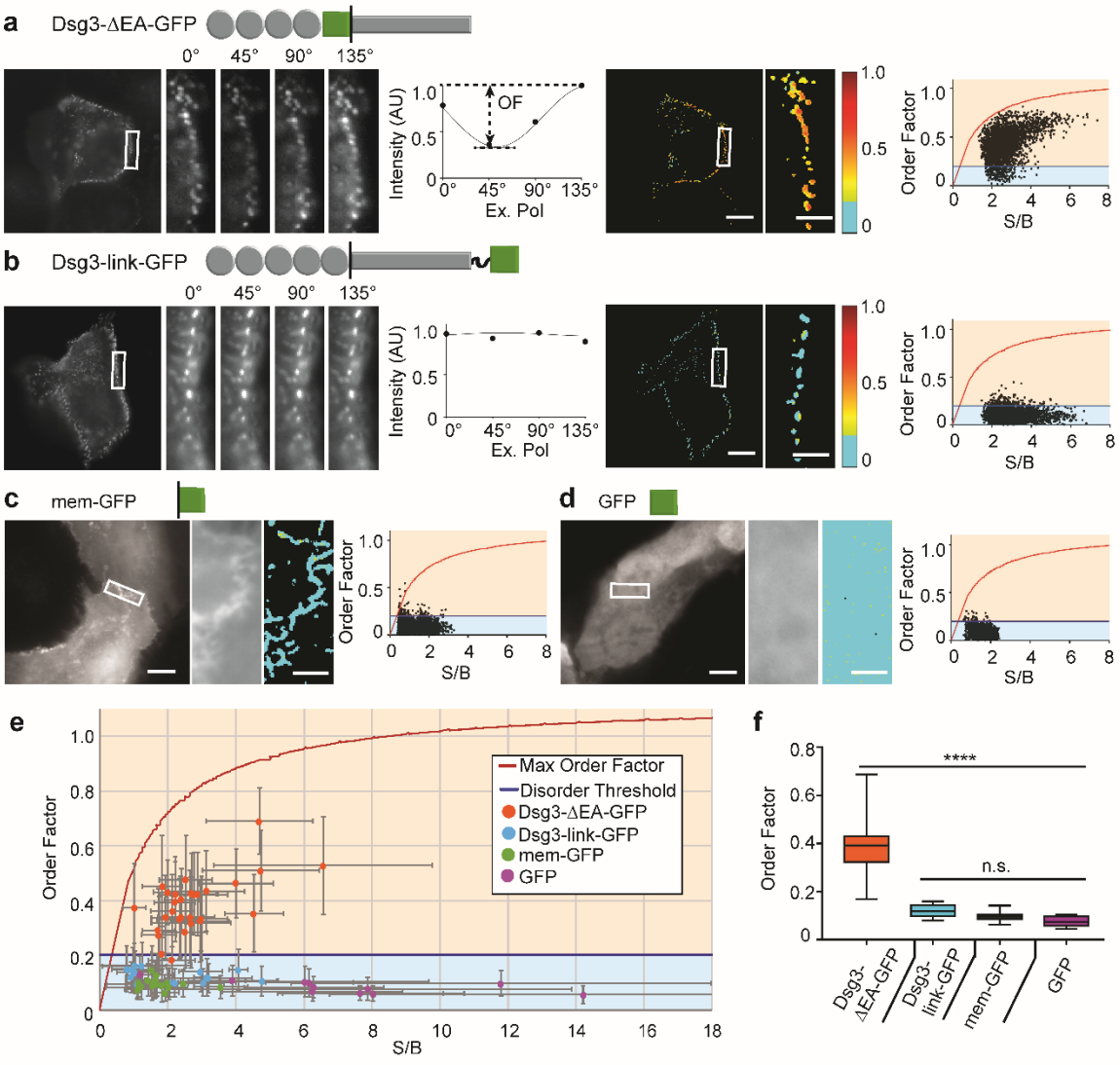

Figure 12. The extracellular domain of Dsg3 is ordered. HaCaT cells expressing (**a**) Dsg3-ΔEA-GFP and (**b**) Dsg3-link-GFP. The average intensity image and individual ROIs (white rectangle) at each excitation polarization are shown. The intensity from a single pixel is plotted as a function of excitation polarization and fit to the sinusoid (Eq 1) from which order factor is determined (solid line). The masked intensity image is pseudo-colored by order factor. Pixel-by-pixel order factor is plotted as a function of signal-to-background ratio (S/B). (**c,d**) Average intensity image of HaCaT cell expressing (**c**) mem-GFP and (**d**) GFP. Average intensity and order factor heatmap shown for the ROI. The pixel-by-pixel order factor is plotted as a function

of S/B. (**a-d**) Scale bar = 10 µm; ROI scale bar= 2 µm. (**e**) Mean order factor as a function of mean S/B for individual cells expressing each construct (error bars: sd) compared to the theoretical max order factor (red line) and disorder threshold (blue line). (**f**) Box plots of the order factor full range (whiskers) with the median (line) and 25-75 percentile range (box). (**** $p<0.0001$; ns= no significance) by one-way ANOVA.

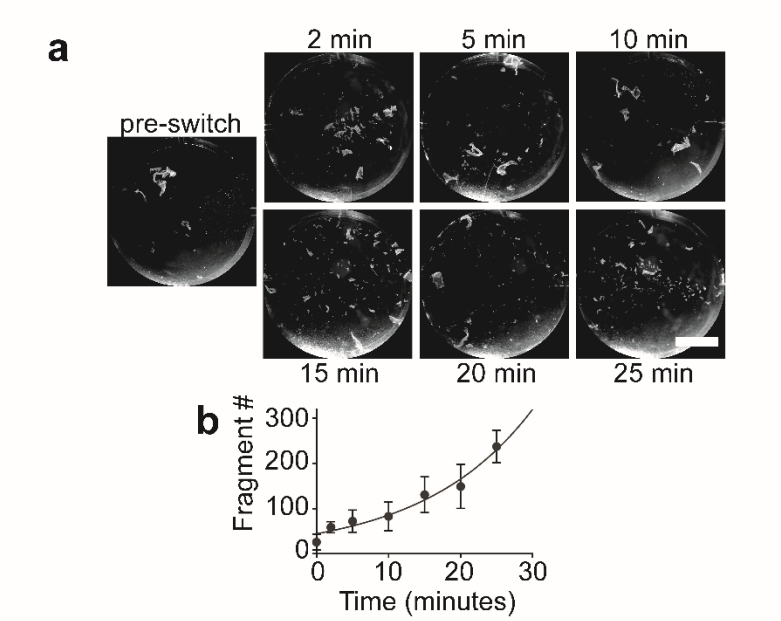

Figure 13. Dynamics of loss of cell adhesion. (**a**) Representative images of HaCaT cell sheets after fragmentation assay at indicated times post-calcium switch. Scale bar = 10mm. (**b**) Plot of the fragment count as a function of time post calcium switch (mean ± sd; n=8). Trendline shows nonlinear (exponential) fit (R^2= 0.97).

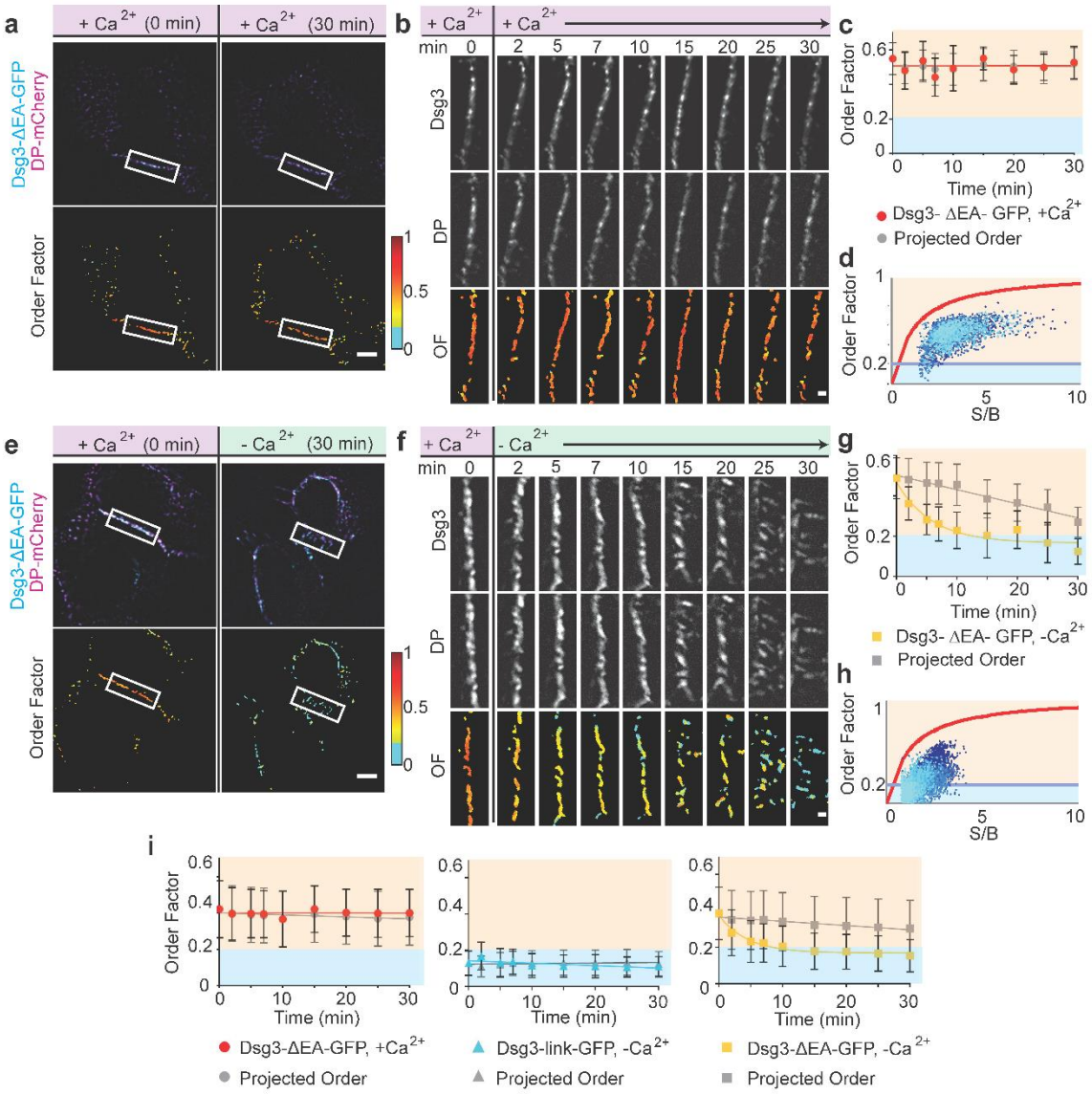

Figure 14. Reduction of Ca^{2+} results in loss of order concurrent with loss of adhesion. (**a**) HaCaT cells were transfected with Dsg3-ΔEA-GFP (cyan) and DP-mCherry (magenta). Cell were imaged pre- (0 min) and post an exchange of normal Ca^{2+} media. Intensity and order factor images for time = 0 and 30 min in normal Ca^{2+}media. Scale bar = 5 μm. (**b**) Time lapse of cell border ROI of Dsg3-ΔEA-GFP, DP-mCherry, and order factor. Scale bar = 1 μm. (**c**) Plot of Dsg3-ΔEA-GFP order factor (red circle; mean ± sd) and the projected order factor (grey circle; mean ± sd) as a function of time. (**d**) Pixel-by-pixel order factor plotted as a function of S/B for

the ROI over the time course (time progresses from dark to light blue). (**e**) HaCaT cells were transfected with Dsg3-ΔEA-GFP (cyan) and DP-mCherry (magenta). Intensity and order factor images are shown for time = 0 and 30 min post switch from normal (~3mM) to low (~0.03mM) Ca^{2+} media. Scale bar = 5 μm (**f**) Time lapse of cell border ROI of Dsg3-ΔEA-GFP, DP-mCherry, and order factor showing dynamics after calcium switch. Scale bar = 1 μm. (**g**) Plot of Dsg3-ΔEA-GFP order factor (yellow square; mean ± sd) and the projected order factor (grey square; mean ± sd) from the ROI as a function of time. Order factor was fit to an exponential decay (solid line) with the equation $y = 0.47e^{5.5^{-t}}$ (R^2=0.94). (**h**) Pixel-by-pixel order factor plotted as a function of S/B for the ROI over the timecourse (time progresses from dark to light blue). (**i**) Population average and projected order factor plotted as a function of time. The average Dsg3-ΔEA-GFP switch to normal calcium (red; n = 6 cells) and average Dsg3-link-GFP switch to low calcium (blue; n = 4 cells) order factors were fit by linear regression (solid lines). The average Dsg3-ΔEA-GFP switch to low Ca^{2+} (n = 8 cells) order factor was fit with an exponential decay $y = 0.38e^{4.5^{-t}}$ (R^2= 0.97).

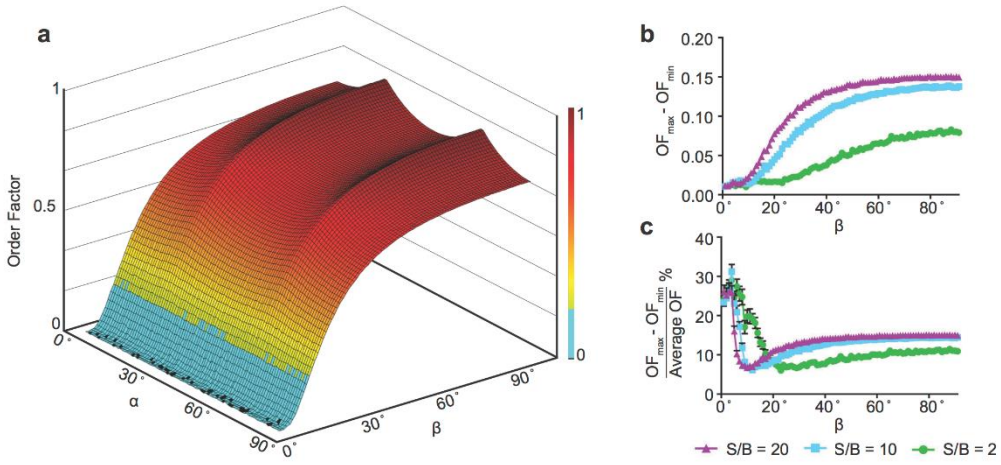

Supplemental Figure 4. α Has a Minimal Impact on Order Factor. a) Simulated average order factor for a range of (α, β) angles. Peaks along α are an artifact resulting from intensity measurements at discrete polarization angles and performing pixel-by-pixel normalization. **b)** Peak-to-trough height of ridges at three different S/B levels plotted over degrees β. **c)** Peak to trough height as a percentage of the order factor (OF) averaged over all a plotted over degrees β at three different S/B levels.

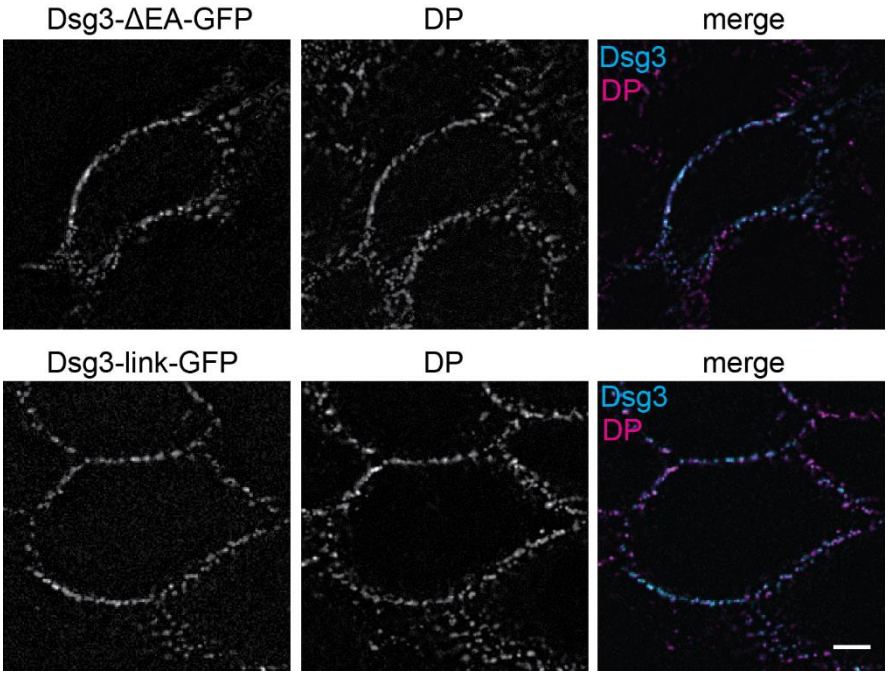

Supplemental Figure 5. Dsg3-GFP constructs colocalize with desmoplakin. HaCaT cells were transfected with Dsg3-ΔEA-GFP or Dsg3-link-GFP. Cells were then pre-extracted, fixed, and stained for desmoplakin (DP). Colocalization between the transfected constructs and the DP staining is seen in the merged images. Scale bar= 10 μm

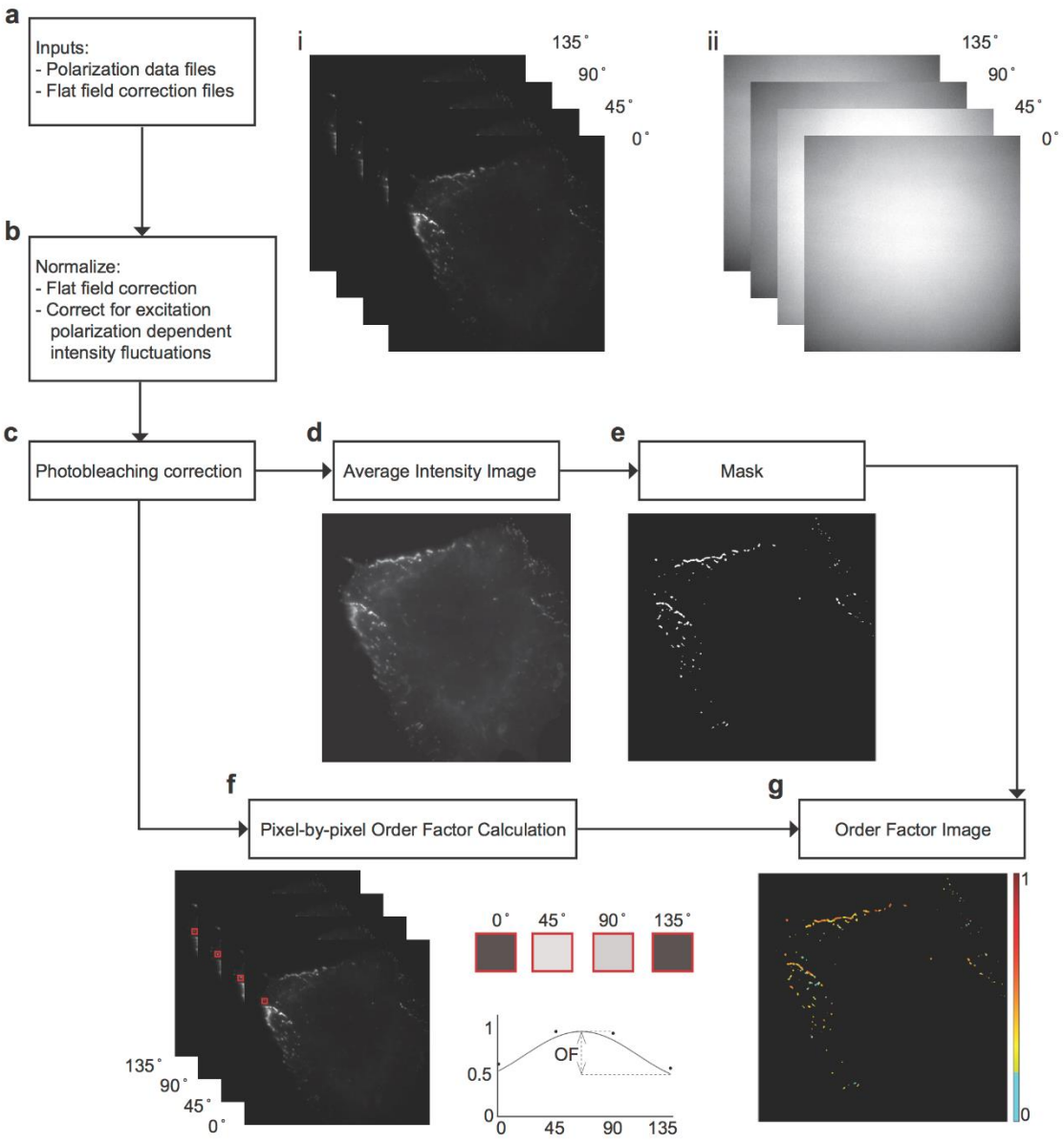

Supplemental Figure 6. Data Analysis Workflow a) The inputs to the analysis program are (i) a set of polarization images of a sample taken at 0°, 45°, 90°, 135° excitation polarization (ii) and a set of images of a fluorescent slide taken at the same excitation polarization angles to determine the beam profile over each excitation polarization. **b)** A correction for fluctuations in intensity as a function of polarization and a flat field correction are performed simultaneously. **c)** Images are corrected for photobleaching based on a calibration dataset. **d)** All four images are averaged

together and **e)** a morphological masking algorithm creates a binary image. **f)** After each pixel is normalized to one across the image set, a pixel-by-pixel order factor calculation is performed by determining the height of the sinusoidal fit to intensity modulation over excitation polarization. **g)** The order factor corresponding to each pixel of the original image is displayed as an order factor heatmap, with pixels falling under the disorder threshold displayed in cyan.

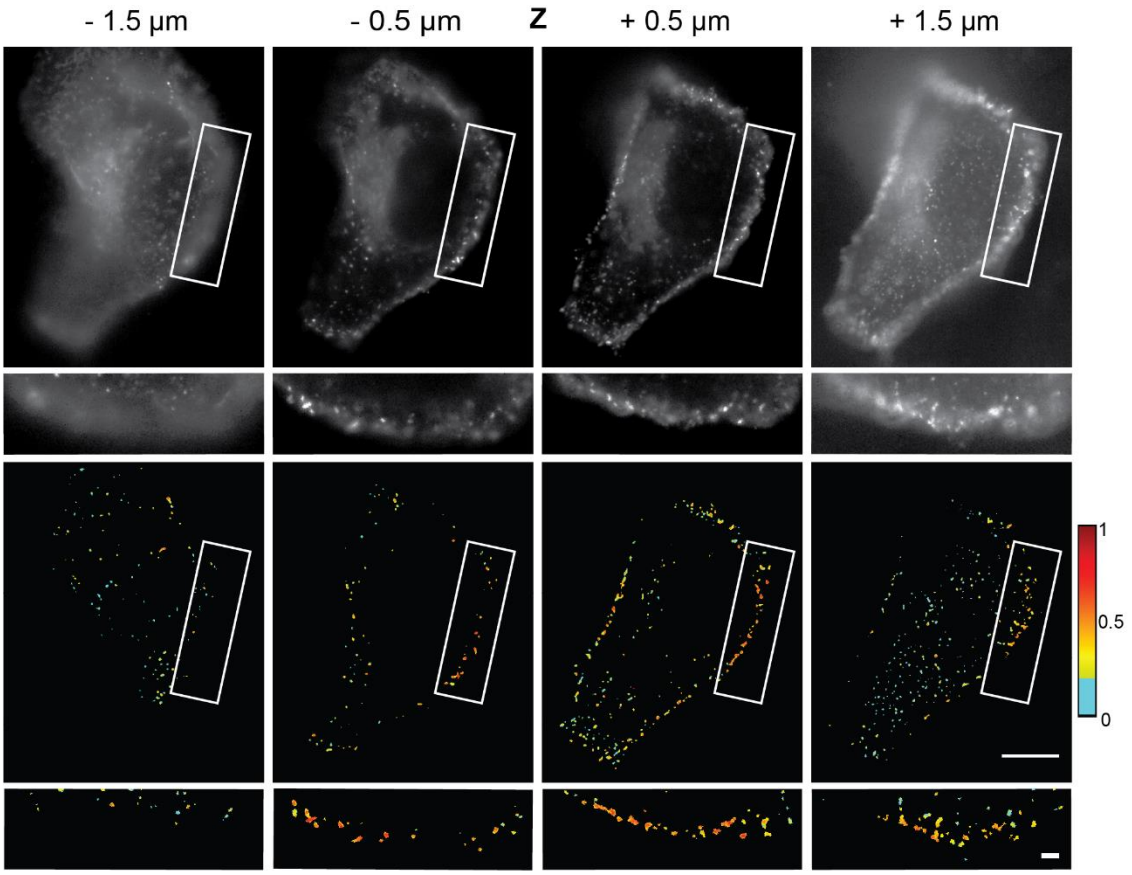

Supplemental Figure 7. Order factor is not focal plane dependent. HaCaT cell transfected with Dsg3-ΔEA-GFP and imaged at four focal planes (z), with a z-step of 1 µm. Average intensity images and order factor heatmaps are shown for each focal plane. ROIs represented by the white rectangles are highlighted below each image. When puncta are visible at cell borders, Dsg3-ΔEA-GFP is ordered regardless of focal plane. Scale bar= 10 µm, ROI scale bar= 2 µm

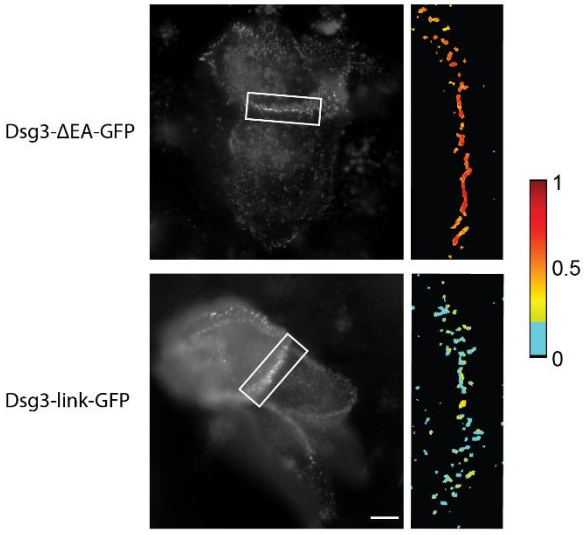

Supplemental Figure 8. Order factor in neighboring transfected cells. Neighboring HaCaT cells are transfected with Dsg3-ΔEA-GFP and Dsg3-link-GFP. Order factor measurements fall within the range of those measured from single cells (Figure 12g). Scale bar= 10 μm

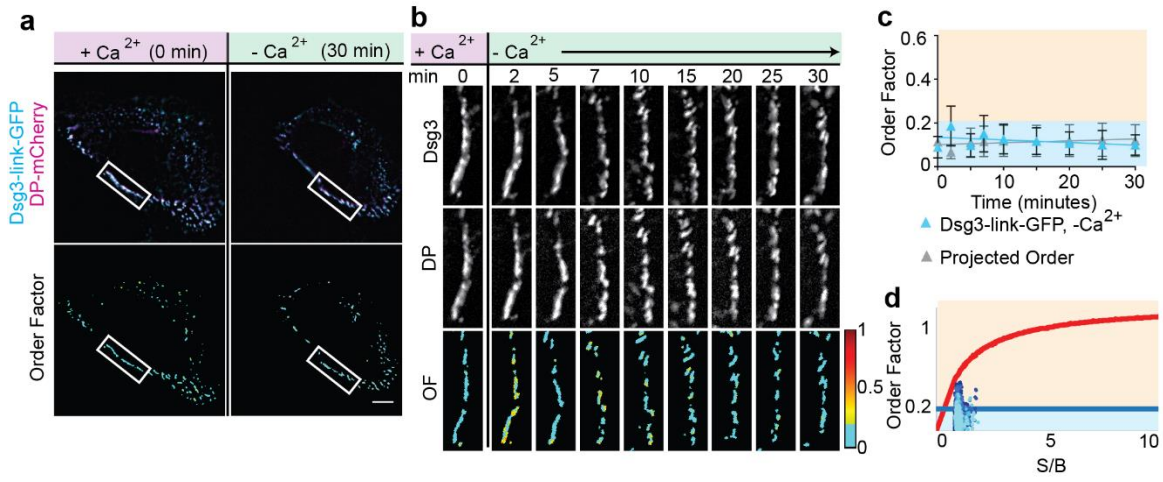

Supplemental Figure 9. Calcium switch time course of Dsg3-link-GFP. a) HaCaT cells were transfected with Dsg3-link-GFP (cyan) and DP-mCherry (magenta). Intensity and order factor images for time = 0 and 30 min post switch from normal (~3 mM Ca^{2+}) to low calcium media (~0.03 mM Ca^{2+}). Scale bar = 5 μm. **b)** Time lapse of cell border ROI of Dsg3-link-GFP, DP-mCherry, and order factor showing dynamics after calcium switch. Scale bar = 1 μm **c)** Plot of Dsg3-link-GFP order factor (blue triangles; mean ± sd) and the projected order factor (grey triangles; mean ± sd). The experimental and projected order factors were not significantly different by two-way ANOVA. **d)** Pixel-by-pixel order factor is plotted for each ROI in the time course, changing from dark to light blue markers through time.

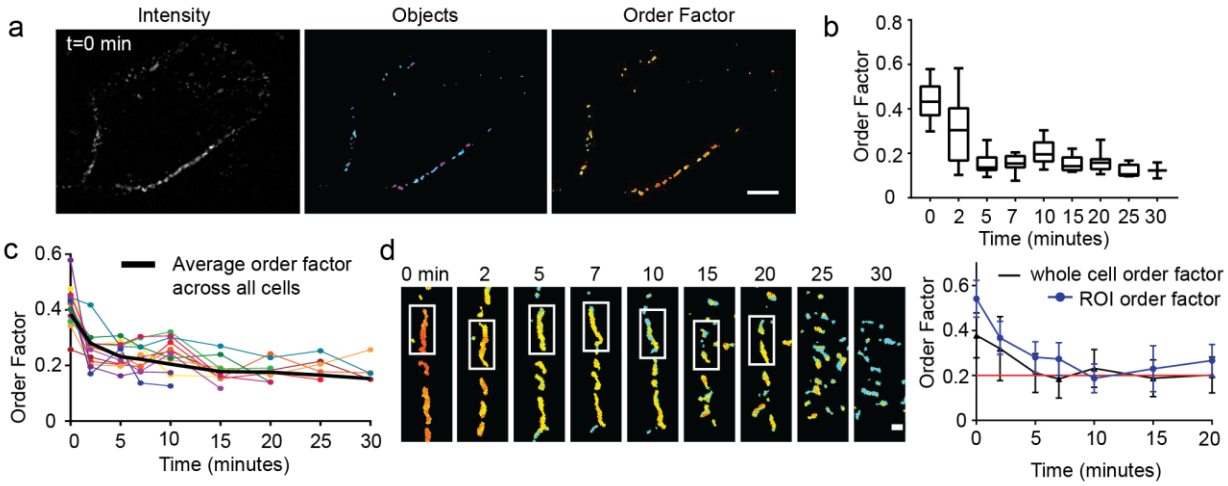

Supplemental Figure 10. Loss of order from single desmosomes. a) Intensity, identified objects, and order factor are shown for a representative cell (SB= 5 μm). **b)** Desmosome objects were identified for all cells analyzed in Fig 14 at each time point. Average order factor was calculated for each object across the time course and the distribution of values is represented as a box and whisker plot. **c)** Order factor was tracked for 12 individual objects across time points (n=4 cells) and compared to the average order factor for each time point. **d)** A desmosome was tracked across time points highlighted by the ROI until it was no longer identifiable. (SB=1 μm) The order factor for each ROI was plotted with the average order factor for the same cell (mean ± s.d).

Chapter 6

Protein exchange regulates calcium independence of epithelial junctions

This chapter adapted from:

Bartle, E.I., T.C. Rao, T.M. Urner, A.P. Kowalczyk, and A.L. Mattheyses. 2019. *In preparation*.

6.1 Introduction

Many vital cellular processes including gene expression, cell division, and cell motility are dependent on macromolecular complexes. Higher level features including protein architecture, order, organization, and dynamics are all critical regulators of macromolecular complex function. Importantly, complexes that appear static can adopt multiple conformational states (Vrabioiu and Mitchison, 2006), act as depots of regulatory proteins (Ray et al., 2007), and support exchange of protein components (Daigle et al., 2001; Griffis et al., 2003). Understanding this multifaceted regulation is key to deciphering macromolecular complex function and is therefore critical for our perception of cellular function and dysfunction in health and disease.

Cell junctions represent a class of plasma membrane associated macromolecular complexes with roles in adhesion, force transmission, and electrical connections (Garcia et al., 2018; Goodenough and Paul, 2009; Parsons et al., 2010). To perform these myriad functions, cell junctions have complex architectures which are key in signal integration and dynamic regulation (Bertocchi et al., 2017b; Kanchanawong et al., 2010b; Kaufmann et al., 2012a; Mehta et al., 2016; Nahidiazar et al., 2015; Stahley et al., 2016a). Epithelial cells harbor two similar yet distinct junction types that span between neighboring cells: desmosomes and adherens junctions. These junctions share the role of mediating cell-cell adhesion and are architecturally analogous with cadherin cores linked to the cytoskeleton though a network of plaque proteins. Despite these similarities, adherens junctions and desmosomes are molecularly and functionally distinct (Rubsam et al., 2018).

One key functional difference between desmosomes and adherens junctions is that desmosomes can adopt a calcium-independent, hyperadhesive state (Wallis et al., 2000). Adherens junctions and calcium-dependent desmosomes disassemble upon chelation of

extracellular calcium. In contrast, hyperadhesive desmosomes maintain adhesion when calcium has been removed (Garrod, 2010; Garrod et al., 2005; Wallis et al., 2000). Desmosome adhesion must be rapidly and precisely tuned to balance tissue strength with plasticity to accommodate a multitude of processes. During development and tissue remodeling, desmosomes are calcium dependent, plastic, and easily reorganized, but ultimately gain hyperadhesion in mature tissue (Kimura et al., 2012). In skin, desmosomes have different adhesive strengths in basal versus suprabasal cells (Garrod and Kimura, 2008; Harmon and Green, 2013). During wound healing desmosomes in suprabasal keratinocytes revert to a calcium dependent state to promote cell migration and wound closure (Garrod et al., 2005; Owen et al., 2008).

Despite the striking diversity between calcium-dependent and hyperadhesive states, corresponding changes to higher order structural features of desmosomes remain unknown. Because cadherins mediate adhesion, they are an obvious candidate for defining these functional states. Cadherins form the adhesive core of the desmosome by trans-binding with neighboring cadherins. “Classical” cadherins, including the adherens junction protein E-cadherin, and desmosomal cadherins are type I transmembrane proteins with similar ectodomain structures, including five extracellular cadherin (EC) domain repeats and inter-domain calcium binding sites which serve to rigidify the tertiary structure (Harrison et al., 2016; Pokutta et al., 1994; Sotomayor and Schulten, 2008). In contrast to classical cadherins, desmosomal cadherins have a more “bent” conformation (Harrison et al., 2016) and exhibit greater flexibility (Tariq et al., 2015) than classical cadherins, features that have been proposed to play a role in accommodating hyperadhesion.

In tissues, desmosomes have a characteristic dense midline bisecting the extracellular space as characterized by electron microscopy (EM). This dense midline is solely found in

hyperadhesive desmosomes and has been observed to correspond with an overlapping of EC1 domains at the site of trans-binding (Garrod et al., 2005; He et al., 2003; Shimizu et al., 2005). Previous research strongly suggested an ordered and periodic organization of desmosomal cadherins in the extracellular space of hyperadhesive desmosomes (Al-Amoudi et al., 2007; Al-Amoudi et al., 2005; He et al., 2003; Rayns et al., 1969). These characteristics support the hypothesis that the arrangement of the cadherin EC domains into quasi-crystalline ordered arrays is a structural feature defining hyperadhesive desmosomes, and possibly drives the function (Garrod, 2013).

Though distinct from the adhesive core, desmosomal plaque proteins, which link the cadherins to the cytoskeleton, have demonstrated roles in hyperadhesion. Overexpression of plakophilin-1 (PKP-1) results in hyperadhesive desmosomes with increased length and altered nanoscale organization (Stahley et al., 2016a; Tucker et al., 2014). By contrast, loss of PKP-3 induced hyperadhesion while PKP-3 overexpression impaired hyperadhesion in a PKCα dependent manner (Keil et al., 2016). Critically, inhibition of protein kinase C alpha (PKCα) has been demonstrated to induce hyperadhesion (Garrod et al., 2005) by preventing phosphorylation of desmoplakin (DP) which also corresponds to an increased its affinity for keratin (Albrecht et al., 2015; Hobbs and Green, 2012). Overexpression of a DP phospho-mutant is also capable of conferring hyperadhesion, illustrating how a single PKCα-dependent phosphorylation site on desmoplakin, allows the cell to rapidly control desmosomal plasticity.

Herein we determine the unique higher order features of hyperadhesive desmosomes by quantifying cadherin order, plaque organization, and protein dynamics in calcium-dependent and hyperadhesive states. Interestingly, changes in cadherin order and desmosome architecture did not contribute to the mechanism of hyperadhesion. Rather, we identify the ability of proteins to

exchange in and out of the complex as the control switch between calcium-dependent and hyperadhesive states. We show protein exchange is controlled via phosphorylation of DP, allowing a rapid switch in protein dynamics between static hyperadhesive and dynamic calcium dependent desmosomes. These findings reveal a novel mechanism for the regulation of cell adhesion that could have far-reaching significance in desmosomal function in health and disease.

6.2 Results

6.2.1 Dsg3 order is not required for adhesive function

Desmosomes can be switched from calcium dependent to hyperadhesive by inhibition of PKCα (Garrod et al., 2005; Kimura et al., 2007; Wallis et al., 2000). To study desmosomal changes associated with hyperadhesion, we used the PKCα inhibitor Gö6976 (Hobbs and Green, 2012). HaCaT cells, immortalized human keratinocytes, were treated with Gö6976 (50 nM) or vehicle (DMSO; mock). To verify Gö6976 treatment lead to hyperadhesion, cells were incubated in media containing normal levels of calcium (>1.8 mM; normal calcium media; NCM) or low levels of calcium (<0.03 mM; low calcium media; LCM) for 90 minutes (Garrod et al., 2005). Cells were then fixed and immunostained for Desmoglein 3 (Dsg3), a desmosomal cadherin, and DP (Fig. 15A). Dsg3 and DP co-localized at cell borders in NCM in both treatment groups, indicating presence of desmosomes. Mock treated cells incubated in LCM exhibited a rounded morphology, lack of cell-cell contact, and loss of desmosomes. In contrast, cells treated with Gö6976 incubated in LCM retained their morphology and cell-cell contacts. DP and Dsg3 co-localized in puncta at cell borders, indicating desmosomal resistance to calcium chelation. This data demonstrates that, as anticipated, treatment with Gö6976 led to desmosome hyperadhesion.

It has been proposed that the order of the cadherin extracellular domain is necessary for hyperadhesion (Garrod, 2013). To address this, we used excitation resolved fluorescence

polarization microscopy (FPM) to measure cadherin in living cells (DeMay et al., 2011; Kress et al., 2011). In FPM, a protein of interest is rigidly tagged with a fluorophore, such that the fluorophore orientation reflects the protein orientation. When excited with linearly polarized light, fluorophores with dipoles oriented parallel to the excitation polarization are excited while those perpendicular are not (Fig. 15B). If proteins within a complex are ordered, fluorescence intensity is modulated by changing the orientation of the excitation polarization (Fig. 15C, top). If the proteins are not ordered, there is no modulation of intensity (Fig. 15C, bottom). Order can therefore be quantified from fluorescence intensity recorded at 4 unique excitation polarizations and then fit with a trigonometric function to determine the order factor.

To measure the order of desmosomal cadherins, we replaced the Dsg3 extracellular anchor domain (EA) with GFP (Dsg3-ΔEA-GFP), as previously described (Bartle et al., 2017). This construct was transfected into HaCaT cells which were then imaged with FPM. We found desmosomal Dsg3 was ordered in the presence of calcium and when cells were switched into LCM, order was rapidly lost, as previously shown (Fig. 1D) (Bartle et al., 2017). Additionally, desmosomes began to disassemble following the switch to LCM, as evidenced by a reduction in fluorescence intensity in puncta at the cell border, rearrangement of the cell junctions, and significant cell morphological changes (Fig. 15D; Supplemental Fig. 11).

To test if cadherins are ordered in the hyperadhesive state, cells were treated with Gö6976 to inhibit PKCα. FPM revealed that Dsg3 was ordered in hyperadhesive desmosomes in NCM (Fig. 15E) and that Gö6976 treatment had no effect on Dsg3 order factor compared to mock treated controls (Supplemental Fig. 12). Interestingly, when Gö6976 treated cells were switched to LCM, order factor rapidly decreased (Fig. 15E) and followed the same dynamics as the mock treated cells. In contrast to the calcium-dependent case, desmosome morphology in

hyperadhesion was unchanged and intact desmosomes could be tracked throughout the time course (Fig. 15E, Supplemental Fig. 11). The rate of order loss (Fig. 15F) and the mean order factor 30 minutes following media change (Fig. 15G) were not significantly different between mock and Gö6976 treated cells. After 30 minutes in LCM, calcium-dependent desmosomes had significantly reduced Dsg3 protein levels compared to cells maintained in NCM or those with hyperadhesive desmosomes (Fig. 15H; Supplemental Fig 11). This demonstrates that cadherin order is not determined by adhesive state. Additionally, cadherins can be simultaneously disordered and adhesive in hyperadhesive desmosomes. A quasi-crystalline arrangement of cadherins therefore cannot be the driving mechanism of hyperadhesion.

Given the surprising result that cadherin order was dependent on calcium, not adhesive state, we wanted to further investigate this relationship. Because of the importance of calcium in regulating the cadherin tertiary structure (Harrison et al., 2016), we hypothesized that cadherin order is indicative of calcium binding. To test this, we used FPM to measure Dsg3 order as calcium was removed and then re-introduced from the media of HaCaT cells with calcium dependent-desmosomes. Cells in NCM were switched into LCM for 10 minutes and then switched back to NCM. Restoring calcium after 10 minutes halted desmosome disassembly, as indicated by the retention of puncta at cell borders over the time course (Fig. 16A). Dsg3 was initially ordered and became disordered following the switch to LCM. Interestingly, switching the cells back to NCM did not rescue order (Fig. 16A,B). We quantified this by comparing the initial order factor in NCM at t = -10 min (0.37±0.07) with the order factors at 10 min (0.23±0.04) and 90 min (0.18±0.03) (mean±sd) (Fig. 16C). To ensure there was not a loss of protein from desmosomes over the experiment, we quantified the desmosomal integrated intensity and found there was an initial loss of intensity immediately following the switch to

LCM, but that level of protein was then maintained over the 90 minutes (Fig. 16D). This revealed that once desmosomal cadherins are disordered following removal of calcium, the loss of order is no reversible and they do not return to their original ordered arrangement. Taken together, these results demonstrate adhesive function can be maintained with disordered cadherins in both calcium-dependent and hyperadhesive desmosomes.

6.2.2 Desmosome architecture is unaltered in hyperadhesion

Given that cadherin order did not correlate with adhesive state, we hypothesized that changes in nanoscale architecture of the desmosomal plaque may provide key insight on the mechanism of hyperadhesion. We used super-resolution direct stochastic optical reconstruction microscopy (dSTORM) (Heilemann et al., 2008) to quantify desmosome protein architecture in different adhesive states (Stahley et al., 2016a). We conducted dSTORM on HaCaT cells with calcium dependent (mock treated) or hyperadhesive (Gö6976 treated) desmosomes. To test if the presence or absence of calcium led to changes in plaque architecture, cells were either maintained in NCM or switched to LCM. Mock treated samples were switched to LCM for only 10 minutes to preserve junctions for imaging, while Gö6976 treated cells were incubated in LCM for 90 minutes to ensure all remaining desmosomes were hyperadhesive. Cells were fixed and labeled with antibodies for either the C-term of DP or plakoglobin (PG), which allowed us to assess architecture throughout the different regions of the desmosomal plaque. Following dSTORM imaging, plaque-to-plaque distances were measured to assess protein localization and architecture. Interestingly, neither treatment with Gö6976 nor switching to LCM resulted in significant changes in desmosome architecture. Plaque-to-plaque distances of both DP C-term (Fig. 17A) and PG (Fig. 17B) were not significantly different across treatment conditions (Fig. 17C). These results show that neither the membrane proximal outer dense plaque, represented by

PG, nor the membrane distal regions of the inner dense plaque, represented by DP C-term, are altered in hyperadhesion induced by PKCα inhibition. We conclude that plaque architecture is maintained regardless of adhesive state and thus cannot explain the mechanism of hyperadhesion.

6.2.3 Desmosomal cadherins are stabilized by hyperadhesion

To further investigate the physical changes between adhesive states, we explored the ability of cadherins to exchange in and out of desmosomes using fluorescence recovery after photobleaching (FRAP). First, cadherin exchange was investigated in cells with Ca^{2+}-dependent desmosomes transfected with Dsg3-ΔEA-GFP in the presence of Ca^{2+}. A region along the cell border containing multiple desmosomes was bleached and fluorescence recovery was measured for 20 minutes (Fig. 18A, Video 1). We found fluorescence recovered within desmosomal puncta, as highlighted by tracking individual puncta within the bleach region across the time course (Fig. 18B,C). To quantify the recovery, fluorescence intensity was photobleaching corrected, normalized, and fit to a one phase association. In the representative cell, the mobile fraction of Dsg3 was 18% with a $t_{1/2}$ of 1.1 min, representing the exchange of Dsg3 in and out of the complex (Fig. 18D).

Next, FRAP was conducted on cells treated with Gö6976 and incubated in LCM to select for hyperadhesive desmosomes (Fig. 18E, Video 2). Minimal recovery within the bleach region was observed, and this recovery did not appear to co-localize with desmosomal puncta in hyperadhesive desmosomes, (Fig. 18F,G). In the representative cell, the mobile fraction of Dsg3 was 8% with a $t_{1/2}$ of 8.5 min representing reduced exchange of Dsg3 in and out of the complex (Fig. 18H).

For the population of cells mock or Gö6976 treated, Dsg3 intensity was averaged and recovery was fit to a curve, resulting in a $t_{1/2}$ of 4.8 min or 3.2 min, respectively (Fig 18I). To determine the mean mobile fraction, the fluorescence intensity of each cell was fit with an individual curve and the plateaus were averaged. The mean mobile fraction for Dsg3 in calcium-dependent cells had a 22±11% (mean ± SD) recovery. Hyperadhesion exhibited decreased Dsg3 mobility with a recovery of 10±2% (Fig 18J). To test if reduced protein mobility in hyperadhesion was conserved across different cadherin isotypes, we performed FRAP on cells transfected with Dsg2-GFP (Supplemental Fig. 13, Videos 3 and 4). We found Dsg2-GFP had an average $t_{1/2}$ of 2.0 min with mock treatment and 3.3 min with Gö6976 treatment (Fig 4I). Average recovery of mock treated desmosomes showed a 27±14% mobile fraction of Dsg2 and a 9±2% recovery in Gö6976 treated desmosomes. This result shows a significant decrease in cadherin mobility for hyperadhesive desmosomes, compared to calcium-dependent.

To confirm that removal of calcium from the media was not responsible for the reduced recovery of Gö6976 treated desmosomes, we measured the mobile fraction of Dsg3 in cells treated with Gö6976 and maintained in NCM. Due to the incomplete effect of Gö6976, desmosomes maintained in NCM were expected to be a mixed population of both hyperadhesive and calcium-dependent (Garrod et al., 2005). The mobile fraction of the population (9±8%) was not significantly different from hyperadhesive desmosomes in LCM (Fig. 18J). However, within this data we observed two sub-populations, one with a mobile fraction of 5±3% (80% of ROIs) and the other with a mobile fraction of 24% ±7% (20% of ROIs) corresponding to the mobile fraction of hyperadhesive and calcium-dependent desmosomes respectively. This result shows hyperadhesive desmosomes can be distinguished from calcium-dependent based on their

mobility. Additionally, it confirms that decreased mobility is a consistent feature of hyperadhesive desmosomes.

6.2.4 Plaque proteins are stabilized in hyperadhesion

Given the reduced mobility of cadherins in hyperadhesion, we hypothesized desmosomal plaque proteins would also exhibit altered diffusion. Therefore, we tested if hyperadhesion resulted in reduced mobility of DP. FRAP experiments were conducted on mock treated HaCaT cells in NCM transfected with DP-mCherry (Fig. 19A, Video 5). DP-mCherry exhibited significant recovery within pre-existing desmosomes which can be tracked through the time course (Fig. 19B,C). A representative cell had a mobile fraction of 41% and a $t_{1/2}$ of 1.5 min for DP (Fig. 19D). DP dynamics in hyperadhesive desmosomes were measured following Gö6976 treatment in LCM (Fig. 19E, Video 6). Recovery of puncta was negligible (Fig. 19F,G) and DP had a low mobile fraction (3%) and a $t_{1/2}$ of 8.3 min in a representative cell (Fig. 19H).

Plakoglobin is a physical link between DP and desmosomal cadherins (Kowalczyk et al., 1997; Kowalczyk et al., 1994). Our cadherin and DP mobilities suggested that hyperadhesion would also result in decreased mobility of PG. Therefore we conducted FRAP experiments on cells transfected with PG-mEmerald mock treated in NCM (Fig. 19I, Video 7). Significant recovery of PG puncta was observed (Fig. 19J,K) corresponding to pre-bleach desmosomes. In a representative cell, PG mobile fraction was 35% with a $t_{1/2}$ of 3.5 min (Fig. 19L). PG mobility was also measured in cells treated with Gö6976 (Fig. 19M, Video 8). PG exhibited significantly reduced mobility in hyperadhesive desmosomes with a mobile fraction of 7% and a $t_{1/2}$ of 9.9 min (Fig. 19N-P).

In a population of cells, the average recovery curves showed decreased mobility for both DP and PG with Gö6976 treatment compared to mock (Fig. 19R). DP exhibited a $t_{1/2}$ of 1.7 min

or 1.1 min while PG exhibited a $t_{1/2}$ of 3.7 min or 2.6 min with mock and Gö6976 treatments, respectively. When analyzing the population of calcium-dependent cells expressing DP, we found that mobile fraction was highly variable between cells (3%-59%), which indicates a potential variability in the binding affinity of DP for keratin (Fig. 19Q). However, both DP (5±4%) and PG (8±6%) treated with Gö6976 consistently had significantly lower mobile fractions than mock treated DP (28±17%) and PG (34±17%). There was no significant difference between DP and PG mobility within the same treatment condition (Fig. 19S). These data show that hyperadhesion results in a loss of mobility throughout the desmosome, from the keratin-binding plaque to the intracellular adhesive core.

6.2.5 Trans-binding is necessary for Dsg3 order and loss of mobility

Since cadherin trans-binding mediates desmosome adhesion, we next tested if loss of trans interactions would impact cadherin order or dynamics. Cadherin trans-binding occurs through a strand-swap mechanism involving insertion of the tryptophan residue at position 2 (W2) from the EC1 domain of one cadherin into a hydrophobic binding pocket of a cadherin on the opposing cell (Haussinger et al., 2004; Overduin et al., 1995; Shapiro et al., 1995). Site directed mutagenesis was used to mutate this key tryptophan residue to alanine (W2A) in the Dsg3-ΔEA-GFP backbone (Dsg3-W2A) to abrogate trans-binding (Harrison et al., 2016; Lowndes et al., 2014). Dsg3-W2A was transfected into HaCaT cells and order factor was measured by FPM. Dsg3-W2A localized to punctate structures at the plasma membrane and had decreased order factor compared to wildtype Dsg3 (Fig. 20A). The order factor from a population of cells expressing Dsg3-W2A (0.22±0.04; mean ± SD) was significantly lower than Dsg3-wt (0.37±0.08l) (Fig. 20B). We conclude that Dsg3-W2A is recruited to desmosomes but

does not adopt an ordered conformation. This shows that trans-binding is necessary to establish cadherin order.

To investigate if cadherin mobility depends on trans-binding, we conducted FRAP experiments on cells co-transfected with the mutant Dsg3-W2A and wildtype DP (Fig. 20C, Video 9). We found that desmosomes incorporate the mutant Dsg3-W2A and a representative cell mock treated in NCM had significant fluorescence recovery of both Dsg3-W2A and DP. The Dsg3-W2A mobile fraction for the representative cell was 30% and had a $t_{1/2}$ of 4.7 min, while DP exhibited a mobile fraction of 12% and had a $t_{1/2}$ of 3.0 min (Fig. 20D). This shows cadherin diffusion in and out of the complex is not dependent on trans-binding.

We next tested if hyperadhesion could decrease the mobility of Dsg3-W2A. Cells co-transfected with Dsg3-W2A and wildtype DP were treated with Gö6976 and switched to LCM for 90 min (Fig. 20E, Video 10). In contrast to the lack of dynamics observed for wildtype cadherins in hyperadhesive desmosomes, Dsg3-W2A exhibited significant fluorescence recovery. In a representative cell, Dsg3-W2A exhibited a 29% recovery and a $t_{1/2}$ of 4.8 min (Fig. 20F). We verified these cells were hyperadhesive by measuring the recovery of DP-mCherry in the same bleach region, and found DP had minimal recovery with a mobile fraction of 2% with a $t_{1/2}$ of $4.1*10^{-8}$ min, as expected.

FRAP experiments were conducted on cells co-transfected with Dsg3-W2A and DP-mCherry (Fig. 20G). When mock treated, W2A and DP showed significant recovery with an average $t_{1/2}$ of 3.8 min and 1.9 min, respectively. When Gö6976 treated, W2A still exhibited significant recovery with an average $t_{1/2}$ of 2.1 min, while DP showed minimal recovery and had a $t_{1/2}$ of 1.7 min. FRAP experiments were also performed on cells expressing only Dsg3-W2A

(ST), which had a $t_{1/2}$ of 2.4 min and 2.2 min, in both mock and Gö6976 treated cells respectively (Supplemental Fig. 14).

The mean mobile fraction of Dsg3-W2A cotransfected with DP-mCherry was not significantly decreased between mock (24±15%) and Gö6976 (19±14%) treatments. As expected, DP in hyperadhesive desmosomes exhibited significantly diminished recovery (10±6 %), which indicates expression of Dsg3-W2A does not disrupt hyperadhesive desmosomes. The mean mobile fraction of cells expressing only Dsg3-W2A (ST) was also not significantly different between Gö6976 and mock treatments (20±11%, 22±13%; respectively). Neither adhesive state nor cotransfection altered the mobile fractions of Dsg3-W2A. These results indicate that trans-binding is an essential component of controlling cadherin mobility in hyperadhesion.

6.2.6 Phosphorylation of DP S2849 is the molecular switch controlling desmosome protein stability in hyperadhesion

Gö6976 treatment prevents DP phosphorylation at S2849, increasing the affinity of DP for keratin (Godsel et al., 2005). Blocking phosphorylation at this site by mutating the serine residue to glycine (S2849G) induces hyperadhesion (Albrecht et al., 2015; Hobbs and Green, 2012). We wanted to test if, like with Gö6976 treatment, cells expressing DP S2849G lost order following calcium chelation. We utilized the mutant DP-S2849G-mCherry in combination with Dsg3-ΔEA-GFP and measured Dsg3 order with FPM. Cells transfected with wildtype (0.37±0.12, mean ± SD) or mutant (0.39±0.11, mean ± SD) DP showed no significant difference in Dsg3 order (Supplemental Fig. 15). Following a switch to LCM, we measured Dsg3 order in cells co-expressing DP-S2849G-mCherry. These cells maintained punctate and stable cell borders, but order decreased rapidly upon removal of calcium (Fig. 21A, B). These dynamics

were observed across the population of cells (Fig. 21C) and the result is comparable to that obtained with PKCα inhibition induced hyperadhesion.

We next tested if DP S2849G could recapitulate the reduced mobility seen with Gö6976 treatment. We co-transfected DP-S2849G-mCherry with Dsg3-ΔEA-GFP and measured DP S2849G dynamics by FRAP (Fig. 21D, Video 11). All FRAP experiments with DP-S2849G-mCherry were conducted in NCM. No significant recovery of DP puncta was observed (Fig. 21E, F) and quantification of recovery in the representative cell revealed an 8% mobile fraction and a $t_{1/2}$ of 3.5 min. We measured Dsg3 dynamics in the same cell co-expressing DP-S2849G-mCherry to determine if the point mutation was sufficient to reduce cadherin mobility (Fig. 21D, Video 12). We found minimal recovery of Dsg3 with a mobile fraction of 5% with a $t_{1/2}$ of 3.4 min (Fig. 21E,F).

For a population of cells, both DP S2849G and Dsg3-ΔEA-GFP exhibit minimal recovery, with a $t_{1/2}$ of 2.8 min for DP S2849G and a $t_{1/2}$ of 2.2 min for Dsg3-ΔEA-GFP (Fig 21G). We also measured the recovery of Dsg3-W2A co-transfected with DP-S2849G-mCherry and observed significant mobility for the trans-binding mutant, as expected (Supplemental Fig. 16). The mean mobile fraction of DP S2849G (7 ± 3%) was not significantly different from the mean mobile fraction of Dsg3 (6±3%) (Fig. 21H). These findings indicate that blocking DP phosphorylation at S2849 is sufficient to stabilize desmosomes and prevent exchange of proteins over the course of 20 minutes. Together these results show that phosphorylation of DP at S2849 acts as the key molecular switch in regulating desmosome adhesive state by controlling protein dynamics.

6.3 Discussion

Modulating adhesive state allows desmosomes to adjust their strength to facilitate tissue integrity and plasticity. A key hypothesis in the field has been that cadherin order is a defining property of hyperadhesion (Al-Amoudi et al., 2007; Garrod, 2013; Rayns et al., 1969). Our data refutes this and shows adhesion can be maintained while cadherins are disordered in both calcium-dependent and hyperadhesive desmosomes. In a calcium pulse-chase experiment, calcium-dependent desmosome disassembly is halted by restoring calcium, but it was not sufficient to rescue cadherin order. This resulted in calcium-dependent desmosomes that were both adherent and disordered. We hypothesize that disordered cadherins can continue to engage in trans-binding because of the increased inter-domain flexibility of the desmosomal cadherins (Tariq et al., 2015). Molecular modeling similarly showed that when calcium was removed and reintroduced to the adherens junction protein C-cadherin, it did not regain its original tertiary structure (Sotomayor and Schulten, 2008). We conclude that cadherin order is not necessary for adhesion, contrary to expectations.

Given that neither cadherin order nor plaque architecture determine desmosome adhesive state, we explored alternative hypotheses. We discovered that the defining physical characteristic determining adhesive state is protein exchange. Calcium-dependent desmosomes exhibited significant mobility of desmosomal cadherins and plaque proteins (Fig. 22A). This diffusion involves exchange between two pools of desmosomal proteins: a pool integrated in the complex and a non-desmosome associated pool. Sequestration, degradation, or endocytosis of cadherins could “tip the balance” of the equilibrium between these populations. In our experiments the equilibrium is disrupted by disordering cadherins through the calcium switch assay, which prevents incorporation of new protein. Loss of the ability to recruit or retain new cadherins

ultimately results in desmosome disassembly (Fig. 22B). We posit the exchange of proteins in the complex provides a mechanism for desmosomes to rapidly adapt to changing cell conditions.

In contrast to the mobility of proteins in calcium-dependent desmosomes, we found that hyperadhesive desmosomes were static (Fig 22C). In our model, hyperadhesion is determined by the PKCα- dependent phosphorylation of DP, which modulates the DP-keratin binding affinity. Evidence suggests PKCα regulates adhesive state endogenously, since it can be sequestered on keratin and co-traffics with DP to desmosomes (Bass-Zubek et al., 2008; Kroger et al., 2013). The increased affinity of DP for keratin reduces DP exchange, which is propagated through the complex and results in reduced mobilities of plakoglobin and the cadherins. In the event that cells need to remodel hyperadhesive desmosomes, they must have a mechanism to switch back to calcium-dependence or be capable of engulfing intact desmosomes (Burdett, 1993; Mattey and Garrod, 1986; McHarg et al., 2014). Thus, phosphorylation of DP acts as a fast and powerful molecular switch for regulating desmosome adhesion via protein exchange.

We postulate here that loss of cadherin order does not result in loss of adhesion in hyperadhesive desmosomes because the desmosomal proteins are “locked” within the complex (Fig. 22D). Since disordered cadherins are immobile in hyperadhesion, we demonstrate that even inefficient trans-binding is sufficient for maintaining adhesion when combined with an immobile plaque. The stabilized plaque association means disordered cadherins still have a higher probability of trans-binding than diffusing out of the complex. Integrating our findings on order, organization, and dynamics, we conclude that protein mobility is the physical property that determines desmosome adhesive state.

While cadherin mobility was consistent in calcium-dependent desmosomes, DP mobility was highly variable and included a population with low mobilities. One way the dynamics of DP

may be determined is through incorporation into the desmosome through different transit pathways. While cadherins must diffuse in the plane of the membrane to enter a desmosome, DP can enter three ways: by trafficking along keratin, diffusion in the membrane through association with PG and cadherins, or directly from the cytoplasm unassociated with any binding partners, each of which could contribute to DP exchange (Bass-Zubek et al., 2008; Godsel et al., 2005). Another mechanism for controlling DP dynamics is by altering the resident time of DP in the desmosome. Post-translational modifications that occur downstream of DP S2849 phosphorylation further promote calcium-dependence and desmosome plasticity (Albrecht et al., 2015). These modifications could contribute to the variability in DP mobility, as desmosomes could exist in different stages of DP modification at any given time.

Since DP mobility controls desmosome stability, we postulated that the Dsg3-W2A would also become trapped in hyperadhesive desmosomes. Interestingly, Dsg3-W2A retained its mobility regardless of DP phosphorylation state. This was surprising because there are no known cadherin conformational changes that could transmit the lack of trans-binding to the desmosomal plaque. This data suggests hyperadhesion requires the correct binding equilibrium between each link in the desmosome structure. We postulate that Dsg3-W2A becomes enriched within desmosomes and occupies space that otherwise would be filled by a wildtype cadherin. Once hyperadhesive, the wildtype cadherins become locked in place, leaving spaces that allow Dsg3-W2A to continue to exchange. This exchange of Dsg3-W2A can therefore occur without disrupting the adhesive state of the complex. These results show that cadherin trans-binding is essential for DP phosphorylation state to control cadherin mobility.

Our findings also shed new light on the conflicting cadherin diffusion rates previously published. Mobilities reported from cell culture models were generally consistent with the

calcium-dependent mobility we measured for Dsg3 and Dsg2 (Gloushankova et al., 2003; Lowndes et al., 2014; Vielmuth et al., 2018; Windoffer et al., 2002). In comparison, desmosomal cadherin mobility in mouse epidermis was low, consistent with a hyperadhesive state (Foote et al., 2013). This is in direct contrast to adherens junction proteins, which do not acquire hyperadhesion and remain mobile in mature epidermis (Cao and Schnittler, 2019; Foote et al., 2013). E-cadherin also exhibited high mobile fractions *in vivo* and the mobile fraction correlated with junction integrity and cell invasiveness (Canel et al., 2010; Erami et al., 2016). Vascular endothelial cadherin mobility was also high and uncorrelated to endocytosis, but restricted by protein-protein interactions (Nanes et al., 2012). Together this points to a global mechanism where protein mobility in and out of cell junctions plays a central role in defining stability versus plasticity.

This work provides a novel framework for understanding the regulation of cell-cell adhesion and raises interesting questions to pursue in further work. Determining adhesive function by measuring FRAP dynamics of cell junctions will allow us investigate adhesion *in situ* and place the findings in the larger context of signaling events, morphological changes, and other regulatory mechanisms. Our results demonstrate that hyperadhesion is established by a loss of protein dynamics and plasticity that is unique to desmosomes. Post-translational modification allows the cell to rapidly and precisely control cell cohesion and tissue integrity by modulating desmosome stability. Epithelial tissues can thus rapidly respond to both intrinsic and extrinsic cues to control processes like cell migration and proliferation that require tuning adhesive function. This regulation is critical for maintaining tissue homeostasis, with aberrant adhesive function contributing to cancer invasiveness, skin fragility, and cardiac arrhythmias. Future work

focused on modulating junctional protein mobility could address these dysfunctions, resulting in new therapeutic options and impacting disease prognosis.

6.4 Materials and Methods

Cell culture

The human immortalized keratinocyte cell line HaCaT (Addex Bio, San Diego CA) was cultured in optimized Dulbecco's modified Eagle's medium (DMEM) (Addex Bio) supplemented with 10% fetal bovine serum (FBS) (Corning, Corning, NY) and 100 U/mL Pen/Strep (Corning) and maintained at 37°C and 5% CO_2. For imaging, cells were either seeded into 8-well #1.5 coverslip bottom dishes (Ibidi, Madison, WI) or on to 25mm #1.5 coverslips (Electron Microscopy Sciences, Hatfield, PA) transfected, and imaged in FluoroBrite DMEM (Fisher Scientific, Waltham, MA), supplemented with 10% FBS and 100 U/mL Pen/Strep.

Cloning and constructs

Dsg3-ΔEA-GFP, Dsg3-link-GFP and DP-mCherry were previously published (Bartle et al., 2017). PG-mEmerald was a gift from Michael Davidson (Addgene plasmid # 54133). Desmoplakin-GFP was a gift from Kathleen Green (Addgene plasmid # 32227). Site-directed mutagenesis was conducted on the Dsg3-ΔEA-GFP backbone using QuikChange II (Agilent, Santa Clara, CA) to generate Dsg3-ΔEA-W2A. Dsg3-ΔEA-W2A primers were forward 5'-3' GGTACAAACGTGAAGCGGTGAAATTTGC and reverse 5'-3' GCAAATTTCACCGCTTCACGTTTGTACC. Site-directed mutagenesis was conducted on both the DP-mCherry and DP-GFP backbones using QuikChange II to generate DP-S2849G-mCherry and DP-S2849G-GFP mutants. DP-S2849G primers were forward 5'-3' GGCGTCAAAGCCTCCTCTCCGGGACCC and reverse 5'-3'

GGGTCCCGGAGAGGAGGCTTTGACGCC. All constructs were verified by sequencing with the Heflin Center for Genomic Sciences (UAB).

Transfection

HaCaT cells were transfected with Lipofectamine 3000 (Fisher Scientific) at 50% confluency following manufacturer's instructions. DNA concentration was optimized to 110ng per 1 cm^2. Cells were imaged 40-48 hours after transfection.

Inhibitor treatment

Gö6976 inhibitor (Abcam, Cambridge, UK) was diluted in DMSO to 10mM or purchased pre-diluted to 10mM (Biovision, San Francisco, CA). The inhibitor was further diluted in DMSO to 50uM and used at 1μL/mL of media to achieve a 50nM final concentration. Mock treatment used 1 μL/mL of DMSO in media. Cells were incubated with the inhibitor or mock for 1 hour at 37°C and 5% CO_2.

Calcium switch

Low calcium media (LCM) was generated by incubating FluoroBrite DMEM (Fisher Scientific) with Chelex resin (Bio-Rad, Hercules, CA) for 1 hour, rotating at 4°C, followed by sterile filtration and supplementation with 3mM EGTA (Millipore, Billerica, MA) For fluorescence polarization experiments, cells were switched from normal calcium FluoroBrite DMEM (~1.8mM) to LCM while on the microscope stage. For FRAP and dSTORM experiments, following either mock or Gö6976 treatment the cells were incubated with LCM at 37°C and 5% CO_2 for 90 minutes where treatment (mock or Gö6976) was maintained in the LCM.

Fluorescence polarization microscopy

Fluorescence polarization microscopy was conducted as described previously (Bartle et al., 2017). Experiments were conducted using a Nikon Ti-2 microscope, equipped with a motorized

stage, stage-top incubator to maintain 37°C and 5% CO_2 (Tokai Hit INUBG2SF-TIZB, Shizuoka, Japan) and a 60x 1.49NA objective. A cleanup polarizer, half-wave plate, and lens were used to polarize and focus a 488 nm laser (Coherent, Santa Clara, CA) at the back focal plane (ThorLabs, Newton, NJ). A motorized mount (PRM1Z8; ThorLabs) rotated the half wave plate and controlled the orientation of the excitation polarization. Images were captured with an ORCA-Flash 4.0 v3 CMOS camera (Hamamatsu, Hamamatsu City, Japan). The system was controlled with Nikon Elements software. A series of four images were collected at 0°, 45°, 90°, and 135° excitation for each polarization image.

Fluorescence Polarization Microscopy analysis

Fluorescence polarization images were analyzed using custom built Polarized Order Detection Software (PODS) v1.0 for MATLAB, as previously published (Bartle et al., 2017). Briefly, data images were corrected with the mean of three flatfield images acquired by imaging a green fluorescent slide (Chroma, Bellows Falls, VT) to control for uneven laser illumination and polarization-dependent intensity changes. A binary mask was then generated on the average intensity image to identify desmosomes. Pixel-by-pixel order factor was calculated as previously described and displayed within the mask. PODS is available for download at www.mattheyseslab.com/software.

FRAP Microscopy

FRAP experiments were conducted on a Nikon Ti-2 A1R confocal microscope, equipped with a motorized stage, stage-top incubator to maintain 37°C and 5% CO_2 (Tokai Hit) and a 60x 1.49NA objective. Images were acquired in Nikon Elements at Nyquist resolution in a 512 x 512 scan region with GASP detectors and 525/50 and 595/30 emission filters. Photobleaching was

performed at 25% laser power with ½ fps pixel dwell for 1 cycle. 5 pre-bleach images were acquired and every 2 minutes after photobleaching for 20 minutes.

FRAP analysis

Using FIJI, intensity was measured for the bleach, reference, photobleaching correction and background regions for each cell at each time point. The bleach and reference intensities were background and photobleaching corrected. Background was measured in a region of interest outside the cell. Photobleaching correction was performed on each cell by measuring intensity at each time point in a non-bleach region of comparable size to the bleach region, normalizing the max intensity to 1 and dividing the background subtracted intensity by the correction value. Graphpad Prism (GraphPad Software, La Jolla, CA) was used to fit the intensities to an exponential and calculate the mobile fraction and $T_{1/2}$ for each bleach region. For population analysis, mean normalized intensity and standard deviation were calculated at each time point after bleaching for cells from 3 technical replicates. Graphpad Prism was used to fit the mean normalized intensity to an exponential and calculate the mobile fraction for the population. In the case of minimal recovery where an exponential curve has an ambiguous fit, the recovery is fit to a linear regression and the mobile fraction (y) is calculated for x= 20 min.

Immunofluorescence staining

Fixation and labeling protocols were done as described previously (Stahley et al., 2016a). Briefly, cells were pre-extracted for 60 seconds with 0.2% Triton X-100 and 300 mM sucrose in PBS with calcium and magnesium at 37°C. Cells were then fixed in 4% paraformaldehyde prepared fresh from 16% electron microscopy grade material (Electron Microscopy Sciences, Hatfield, PA) for 12 minutes, followed by 30 minutes blocking and permeabilization with 5% normal horse serum, 5% normal goat serum, 1% bovine serum albumin and 0.25% Triton X-100

with multiple washes between steps. Cells were incubated in primary antibody for 3 hours and secondary antibody for 1 hour. Samples were stored chilled, in the dark.

Antibodies

Primary antibodies were anti-desmoplakin (DPI/II, Bethyl Labs, Montgomery, TX), anti-γ-catenin (H-80, Santa Cruz Biotechnology, Dallas, TX), and anti-desmoglein 3 (G194, Progen Biotechnik GmbH, Heidelberg, Germany). Secondary antibodies were Alexa 488 and Alexa 647 conjugated goat anti- mouse or goat anti- rabbit (IgG H&L) from Invitrogen (Grand Island, NY).

dSTORM

dSTORM experiments were conducted on a Nikon Ti-2 N-STORM microscope equipped with a 100× 1.49 NA oil immersion objective, 488 and 647 nm lasers, and an iXon ultra EMCCD camera (Andor). 60,000-100,000 frames were collected with sub-critical inclined excitation and reconstructed in Nikon Elements. Photoswitching imaging buffer included glucose oxidase (Sigma, St Louis, Missouri), glucose (Sigma), catalase (Roche, Penzberg, Germany), and β-mercaptoethanol (Sigma) (Rust et al., 2006).

dSTORM analysis

Reconstructed dSTORM images were exported at 4nm/pixel and saved as 16-bit TIFF images to be processed in MatLab (The MathWorks, Natick, MA) as previously described (Stahley et al., 2016a). Briefly, intensity is averaged along the length of the desmosome and then measured by linescan across the desmosome axis. Linescans were normalized, smoothed, and the peak finder function was used to measure the “peak-to-peak” distance. Custom MatLab scripts for desmosome dSTORM processing are available upon request.

Statistics

All statistical analysis was performed with Graphpad Prism (GraphPad Software). P-values were determined by Student's t-test when measuring significance between two conditions. P-values were determined one-way ANOVA with multiple comparisons when measuring significance between more than two conditions. Curve fitting for FRAP analysis was done using linear regression or one-phase association fitting algorithms, where the plateau determines the mobile fraction.

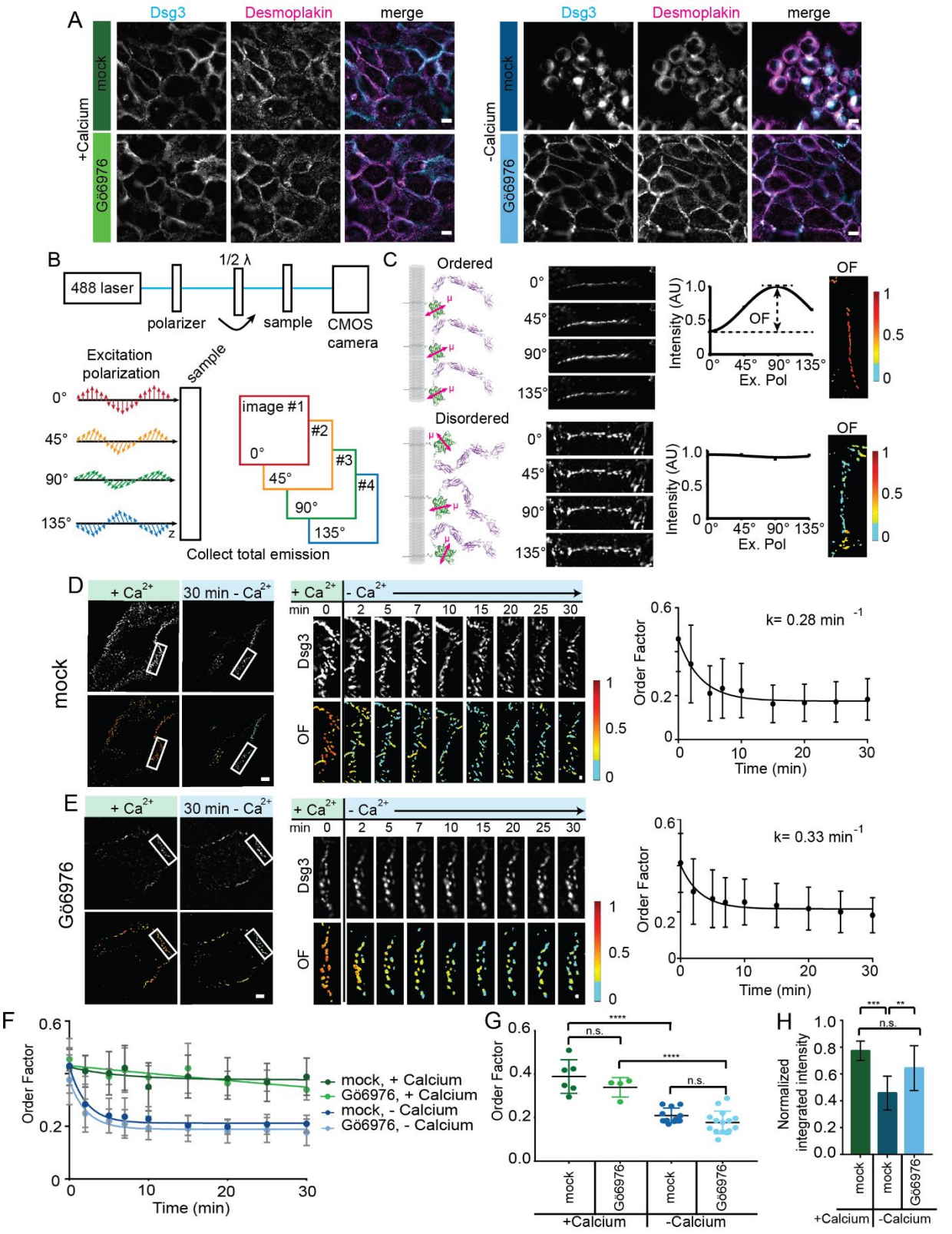

Figure 15. Hyperadhesion does not protect against loss of Dsg3 order in low calcium. (A) Representative images of HaCaT cells treated with either vehicle (DMSO; mock) or Gö6976,

maintained in normal calcium media (NCM; left) or switched into low calcium media (LCM; right) for 90 min. Cells were stained for Dsg3 (cyan) and DP (magenta). scale bar = 20 μm (B) Schematic of the fluorescence polarization microscope. Samples are sequentially illuminated with four different angles of polarized excitation and total emission. (C) Ordered cadherins (top) are differentially excited by the different excitation polarizations, resulting in modulated intensity across the four images. Disordered cadherins (bottom) are equally excited regardless of excitation polarization resulting in equal intensity for each angle of excitation. Intensity was plotted as a function of excitation polarization and the amplitude was used to calculate pixel by pixel order factor (OF). (D) HaCaT cells were transfected with Dsg3-ΔEA-GFP, mock (D) or Gö6976 treated (E) and switched from NCM to LCM. Fluorescence and order factor images in NCM ($+Ca^{++}$) and after 30 min in LCM ($-Ca^{++}$) (scale bar = 5μm). Region of interest (ROI) indicated by white box is enlarged and shown as a timecourse (scale bar = 1μm). Order factor for the ROI plotted as a function of time (mean±sd) and fit to an exponential decay. Order factor decreased at a rate of (D) 0.28 ± 0.05 min^{-1} and (E) 0.33 ± 0.09 min^{-1}. (F-G) Population analysis of cells treated mock in NCM (n = 6), mock in LCM (n = 11), Gö6976 in NCM (n = 6), and Gö6976 in LCM (n = 15) (F) Order factor plotted as a function of time (mean±sd). (G) Order factor at t=30 minutes (mean±sd) compared by one-way ANOVA with multiple comparisons (n.s., not significant, $p>0.05$; **** $p\leq0.0001$). (H) Integrated intensity was measured for the calcium switch time course and normalized to the first time point. Normalized integrated intensity for the 30 min time point compared by one-way ANOVA with multiple comparisons (n.s., not significant, $p>0.05$; ** $p\leq0.01$; *** $p\leq0.001$).

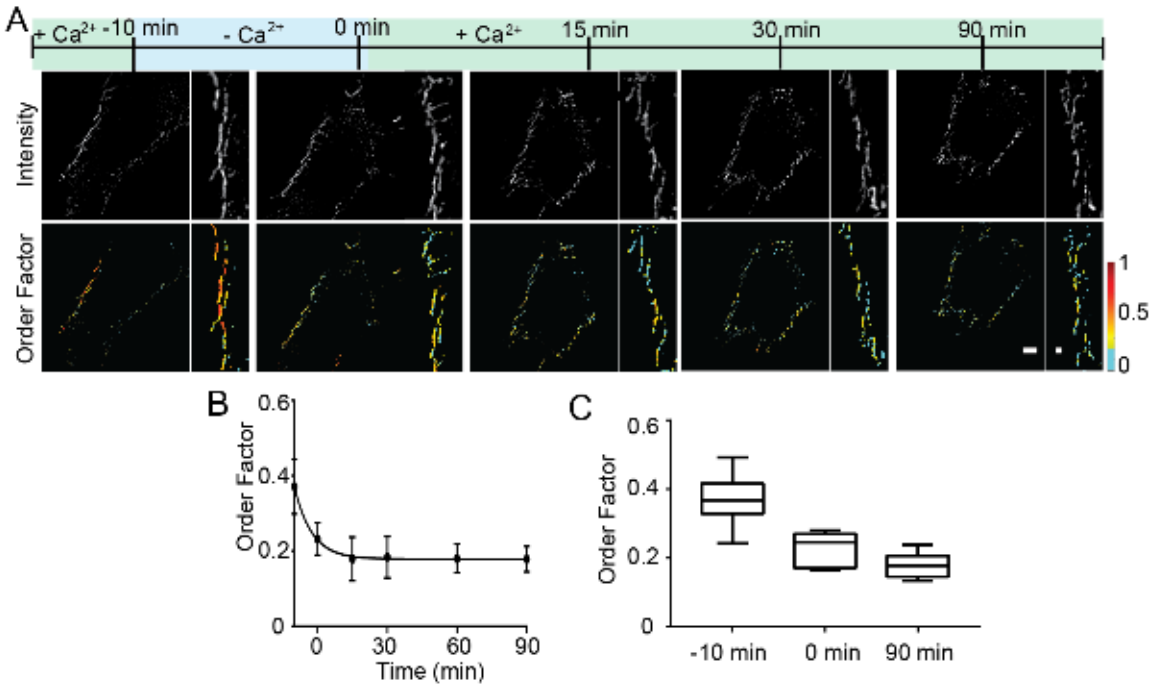

Figure 16. Dsg3 order is not restored following a calcium pulse-chase. (A) HaCaT cells were transfected with Dsg3-ΔEA-GFP and subjected to a calcium pulse chase including: incubation in normal calcium media (NCM), at t = -10 min switch to low calcium media (LCM) for 10 minutes, and at t = 0 return to NCM which was maintained for 90 minutes. Cells were imaged with fluorescence polarization microscopy and Dsg3-ΔEA-GFP intensity and order factor images are shown for a whole cell and ROI over the timecourse. Scale bar=5 μm; ROI scale bar=1 μm. (B) Quantification of order factor (mean±sd) for a population of cells as a function of time over the pulse-chase (n=6). (C) Order factor at -10 min, 0 min, and 90 min where whiskers indicate the range of the data, while the line and box represent the median ± quartile (ns: not significant, $p>0.05$; *** $p\leq0.001$; **** $p\leq0.0001$; ANOVA).

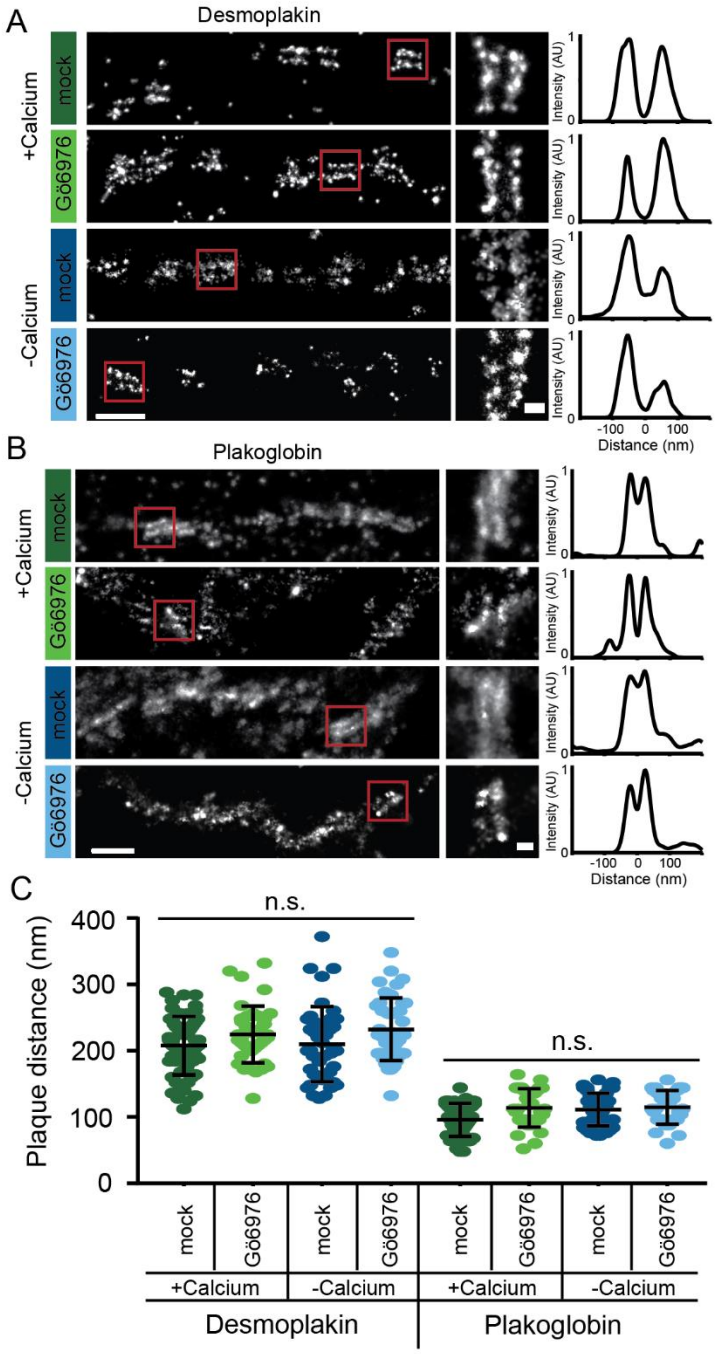

Figure 17. Nanoscale organization of desmosomal plaques is unchanged in Gö6976 induced hyperadhesion. HaCaT cells were mock or Gö6976 treated and incubated in NCM or LCM, fixed, stained for (A) desmoplakin (DP) or (B) plakoglobin (PG) and imaged by dSTORM. Representative cell borders are shown for each condition. Scale bar= 500 nm. Regions of interest

(ROIs) indicated by the red squares illustrate individual desmosomes ROI scale bar= 100 nm. Linescans of fluorescence intensity perpendicular to the desmosome axis highlight the peaks used to quantify plaque architecture. (C) Quantification of plaque-to-plaque distance shows no significant difference across treatment groups for DP or PG by one-way ANOVA followed by Tukey's multiple comparison test. (DP left to right, n=58, 40, 44, 41; PG left to right n= 41, 30, 48, 31) Bars represent mean ± sd (ns: not significant, $p>0.05$).

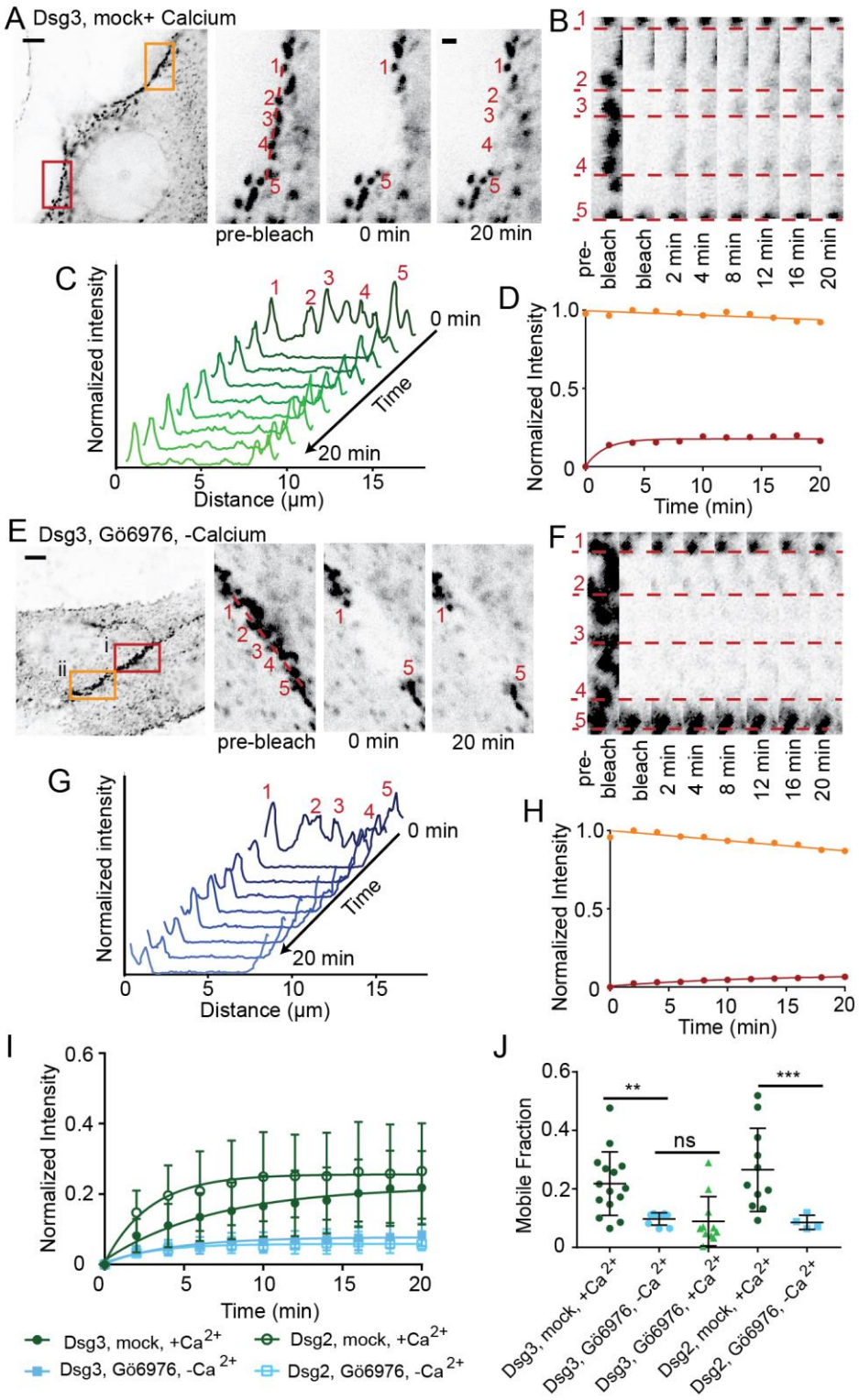

Figure 18. Hyperadhesion blocks Dsg3 mobility in desmosomes. (A-D) FRAP experiments were conducted on HaCaT cells transfected with Dsg3-ΔEA-GFP and mock treated in normal

calcium media (NCM). (A) Representative cell (inverted intensity) with bleach (red) and control (orange) ROIs. Bleach ROI shown with individual desmosomal puncta indicated. Scale bar = 5μm; ROI scale bar = 1μm. (B) Images of bleach region over time with dashed lines underscoring individual puncta, highlighting recovery over time. (C) Staggered intensity linescans through the bleach region at each time point show the recovery of individual puncta. (D) FRAP recovery curves of the bleach (red) and reference (orange) ROIs. The bleach region intensity was fit to a one-phase association to determine mobile fraction (18% ± 0.6% SE). (E-H) FRAP experiments were conducted on HaCaT cells transfected with Dsg3-ΔEA-GFP, Gö6976 treated, and switched to low calcium media (LCM) for 90 minutes. (E) Representative cell (inverted intensity) with bleach (red) and reference (orange) ROIs. Bleach ROI shown with individual desmosomal puncta indicated. Scale bar = 5μm; ROI scale bar = 1μm. (F) Images of bleach region over time with dashed lines underscoring individual puncta, highlighting recovery over time. (G) Staggered intensity linescans through the bleach region at each time point show the absence of recovery of individual puncta. (H) FRAP recovery curves of the bleach (red) and reference (orange) ROIs. The bleach region intensity was fit to a one-phase association to determine mobile fraction (8% ± 0.9% SE). (I) Average FRAP recovery curves for cells transfected with Dsg3-ΔEA-GFP and mock treated in NCM (n=15) or Gö6976 treated in LCM (n=11) and cells transfected with Dsg2-GFP and mock treated in NCM (n=11) or Gö6976 treated in LCM (n=10). Data points mean±sd and fit to one-phase association curve. (J) Mobile fraction for treatments in (I) and Dsg3-ΔEA-GFP Gö6976 treated in NCM (n=11) where whiskers indicate the range of the data, while the line and box represent the median ± quartile. The Dsg3 mobile fraction was significantly lower with Gö6976 (10% ± 2%) than mock treatment (22% ±11%) by Student's t-test. There was no significant difference in Dsg3 mobile fraction in

Gö6976 treated cells in NCM or LCM. The Dsg2 mean mobile fraction was significantly lower with Gö6976 treatment (9% ± 2%) than mock treatment (27% ±14%) by Student's t-test (ns: not significant, $p>0.05$; ** $p<0.01$; *** $p<0.001$).

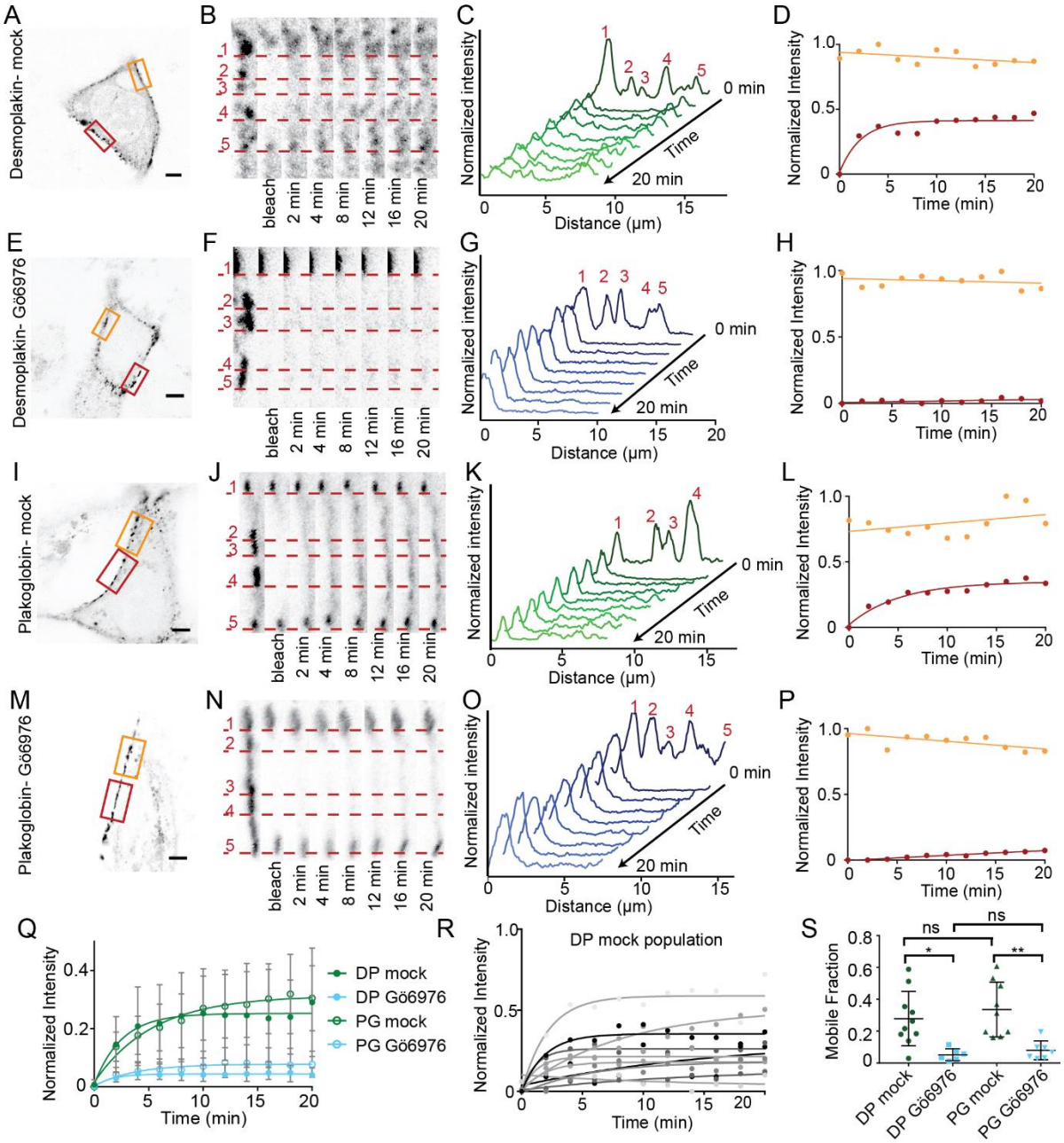

Figure 19. Plakoglobin and desmoplakin mobility is reduced in hyperadhesive desmosomes. (A-D) FRAP experiments were conducted on HaCaT cells transfected with DP-mCherry, mock treated, in NCM. (A) A representative cell (inverted intensity) shows desmosomes at the cell-cell border with a bleach region (red) and reference region (orange). (B) Individual puncta can be tracked through the time course and are underscored by dashed lines. (C) Desmosome recovery

is further highlighted by the recovery of individual peaks in the staggered linescans from the bleach region at each time point. (D) Fluorescence intensity of the bleach and reference regions is plotted through the time course. The intensity of the bleach region was fit to a one-phase association to calculate mobile fraction (41% ± 2% SE). (E) FRAP experiments were conducted on HaCaT cells transfected with DP-GFP or DP-mCherry and treated with Gö6976. (F) Individual desmosomes are underscored by dashed lines, which highlights the lack of recovery within puncta. (G) Lack of desmosome recovery is further highlighted by the linescans from each time point. (H) Fluorescence intensity of the bleach and reference regions is plotted through the time course. The bleach region intensity is fit to a one-phase association and use to calculate the mobile fraction (4% ± 3% SE). (I) FRAP experiments were conducted on HaCaT cells transfected with PG-mEmerald and mock treated. (J) Individual puncta can be tracked through the time course and are underscored by dashed lines. (K) Desmosome recovery is further highlighted by the recovery of individual peaks in the staggered linescans from the bleach region at each time point. (L) Fluorescence intensity of the bleach and reference regions is plotted through the time course. The bleach region intensity was fit to a one-phase association and use to calculate the mobile fraction (35% ± 2% SE). (M) FRAP experiments were conducted on HaCaT cells transfected with PG-mEmerald and treated with Gö6976. (N) Individual desmosomes are underscored by dashed lines, which highlights the lack of recovery within puncta. (O) Lack of desmosome recovery is further highlighted in the linescans. (P) Fluorescence intensity of the bleach and reference regions is plotted through the time course. The bleach region intensity is ambiguously fit by a one-phase association and can only be correctly fit by a line, which results in a mobile fraction y= 8% ±2% when x=20 min. (Q) FRAP recovery of DP-mCherry from individual cells shows a wide variability in fluorescence recovery (n=11). (R) FRAP recovery

(mean± sd) for HaCaT cells transfected with either PG-mEmerald mock (n=9) or Gö6976 (n=8) treated or DP-mCherry mock (n=14) or Gö6976 (n=7) treated were fit to one-phase association curves. (S) Mean mobile fraction for each condition where the line and box represent the median ± quartile and whiskers indicate the range of the data. The mobile fraction of DP in cells treated with Gö6976 (5% ± 4%) was significantly less than mock treated cells (28% ± 17%). The mobile fraction of PG in cells treated with Gö6976 was significantly lower (8% ± 6%) than mock treatment (34% ± 17%) by one-way ANOVA with multiple comparisons (ns: not significant, $p>0.05$; * $p<0.05$; ** $p<0.01$).

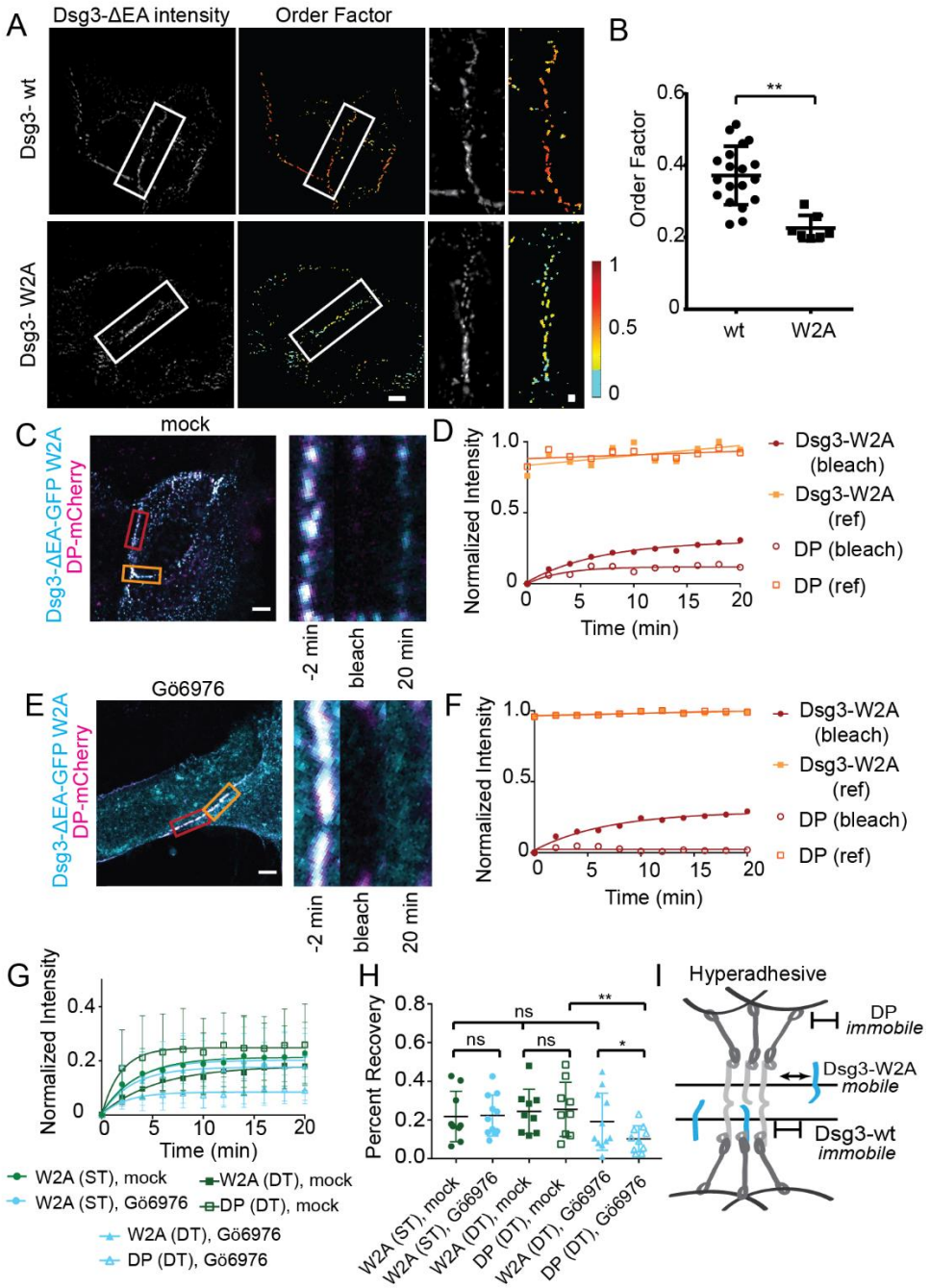

Figure 20. Dsg3 trans-binding is critical cadherin order and stability. (A) HaCaT cells were transfected with Dsg3-ΔEA-GFP (Dsg3) or Dsg3- ΔEA-GFP-W2A (Dsg3-W2A) and imaged with fluorescence polarization microscopy. Representative cells and ROIs shown of intensity and order factor. Scale bar= 5 μm, crop scale bar=1 μm. (B) Quantification shows Dsg3-W2A (n=7)

is significantly less ordered than Dsg3 (n=19) (mean±sd; ** $p<0.01$; Student's t-test). (C) FRAP experiments were conducted on HaCaT cells cotransfected with Dsg3-W2A and DP-mCherry and mock treated in NCM. (D) Dsg3-W2A exhibited significant recovery of 30% and a $t_{1/2}$ of 4.7 min, while DP exhibited a recovery of 12% and a $t_{1/2}$ of 3.0 min. (E) Dsg3-W2A cotransfected with DP-mcherry was treated with Gö6976 and recovery was measure over time. (F) Dsg3-W2A with Gö6976 exhibited recovery of 29% a $t_{1/2}$ of 4.8 min, while DP exhibited a recovery of 2% and a $t_{1/2}$ of $4.1e^{-8}$ min. (G) Average FRAP recovery curves for cells single transfected with W2A mock had a $t_{1/2}$ of 2.4 min (n=9) while Gö6976 treated cells had a $t_{1/2}$ of 2.2 min (n = 12). Mock treated cells cotransfected with W2A and DP exhibited a $t_{1/2}$ of 3.8 and 1.3 min, respectively (n=9). Gö6976 treated cells cotransfected with W2A and DP exhibited a $t_{1/2}$ of 2.1 and 1.7 min, respectively (n=11). (H) Mean mobile fractions for a population of cells expressing W2A were as follows: mock ST- 22±13% ; Gö6976 ST- 22±11%; mock DT- 24±12%; Gö6976 DT- 19±14%, none of which were significantly different. Mean mobile fractions for DP co-expressed with W2A were 25±14% for mock treated cells and 10±7% for Gö6976 treated cells, which were significantly different (ns: not significant $p>0.05$; * $p<0.05$; ** <0.01). (I) Model of Dsg3-W2A mobility in hyperadhesive desmosomes.

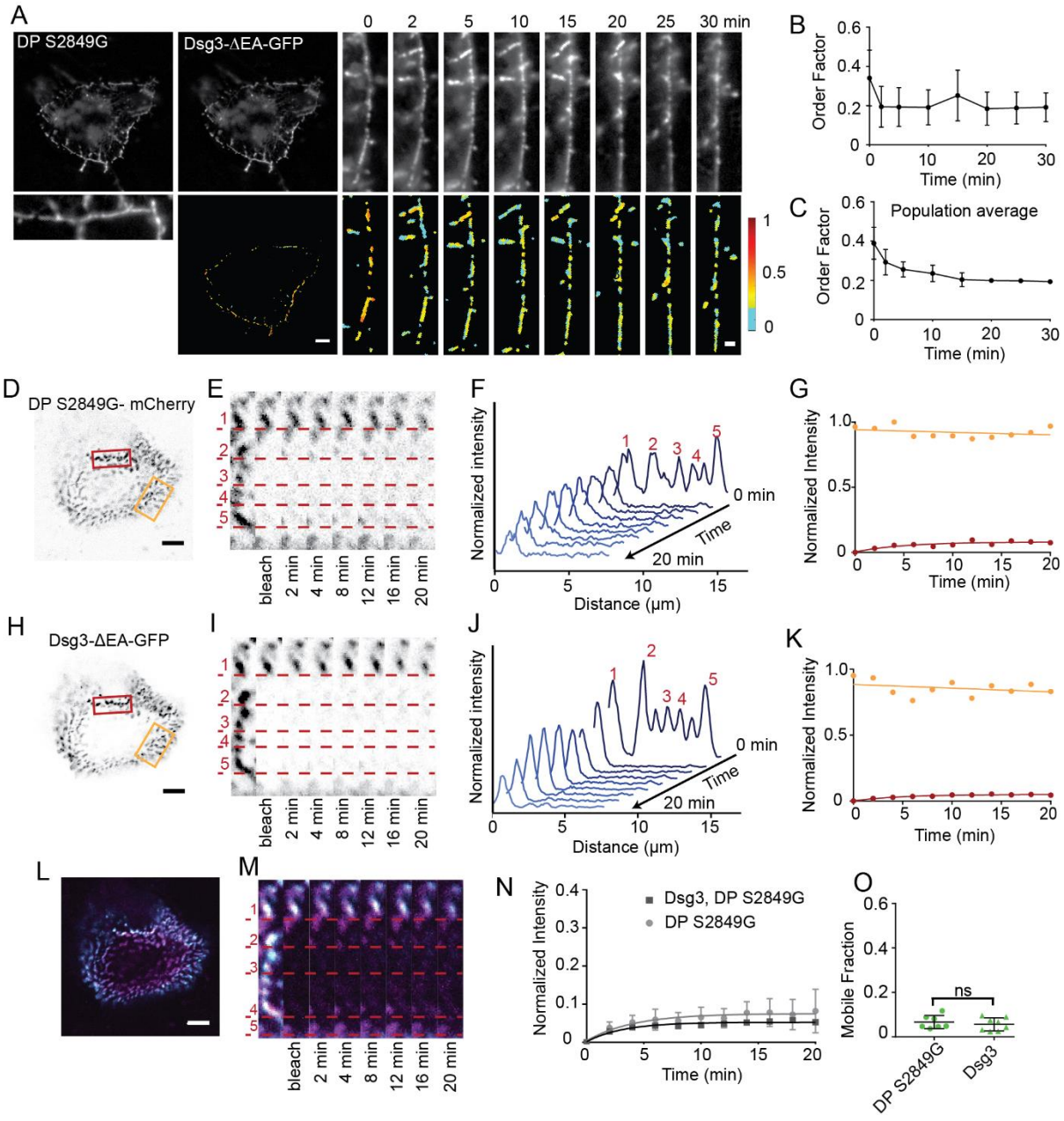

Figure 21. DP S2849G induces hyperadhesion and decreases mobility of desmosomal proteins (A) Cells were co-transfected with Dsg3-ΔEA-GFP and DP S2849G-mCherry and imaged with FPM. (B) Order factor of the ROI is plotted over time and shown to fall below the threshold for disorder (0.2). (C) Order factor over time (mean±sd) plotted from a population of cells (n=8). (D) HaCaT cells were transfected with DP S249G-mCherry and fluorescence

recovery was measured for 20 minutes. (E) Individual desmosomes are underscored by dashed lines and their recovery is measured over time. (F) Linescans of each time point highlight the lack of recovery of individual peaks. (G) The bleach region intensity is fit to a one-phase association and use to calculate the mobile fraction (8% ± 0.9%). (H) HaCaT cells transfected with DP S2849-mCherry also expressed Dsg3-ΔEA-GFP. (I) FRAP on Dsg3-ΔEA-GFP in the presence of DP S2849-mCherry shows decreased mobility. (J) Linescans through the bleach region for each time point do not have peaks corresponding to the initial desmosomes, showing the lack of recovery. (K) The bleach region intensity is fit to a one-phase association and use to calculate the mobile fraction (5% ± 0.2%). (L) Merged image of DP S2849G mCherry and Dsg3-ΔEA-GFP shows colocalization. (M) FRAP timecourse of merged channels shows equivalent lack of recovery. (N) Mean normalized intensity with standard deviation for DP S2849G-mCherry (n=7) and Dsg3-ΔEA-GFP co-transfected with DP S2849G-mCherry (n=8) in a population of HaCaT cells were fit to a one-phase association. (O) DP S2849G (7% ± 3%) mobility was significantly less than wildtype DP. Dsg3 mobility in cells expressing DP S2849G (5% ± 3%) was significantly less than Dsg3 in cells expressing wildtype DP. There was no significant difference in mobile fraction between DP S2849G and Dsg3 in cells expressing DP S2849G. Significance tested by Student's T-test (mean±sd) (ns: not significant, $p>0.05$; * $p<0.05$; ** $p<0.01$).

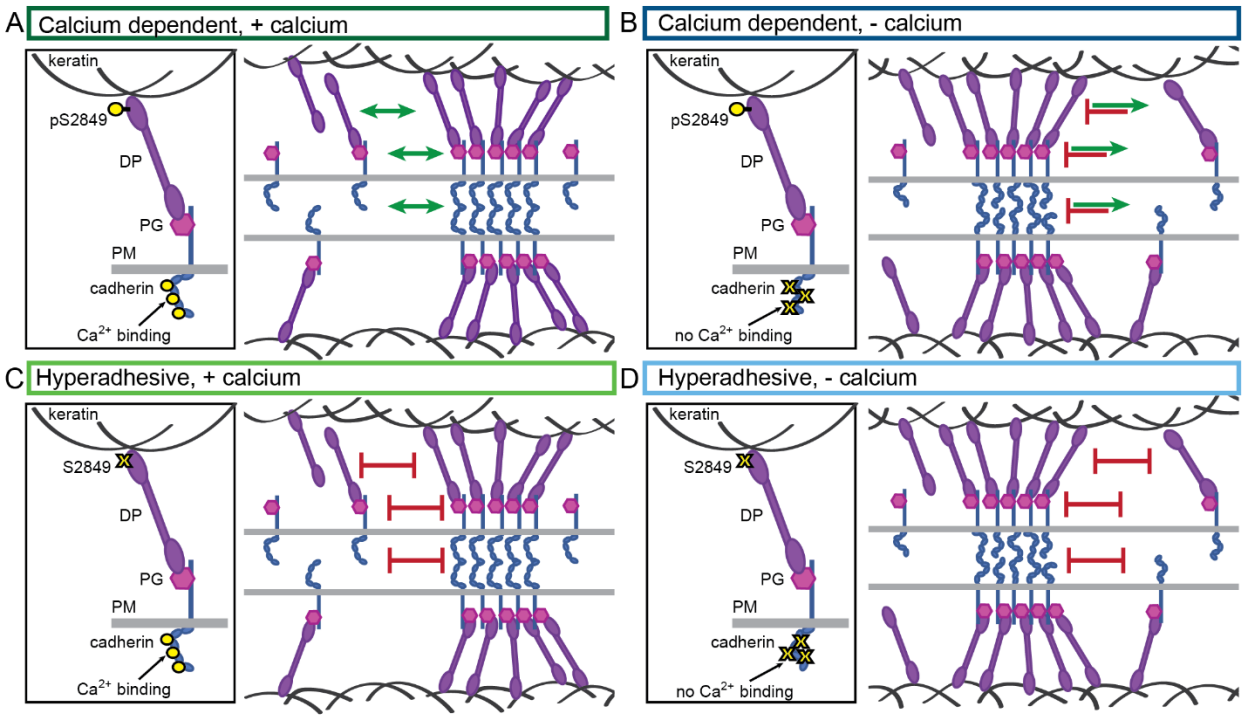

Figure 22. Hyperadhesion is the result of decreased desmosome protein mobility. Summary model illustrating how restricted mobility confers hyperadhesion. (A) In the presence of calcium, cadherins in calcium dependent desmosomes are ordered and desmosome proteins diffuse in and out of the complex. (B) If calcium is depleted from calcium dependent desmosomes, cadherin order is lost and desmosomes disassemble. (C) In hyperadhesive desmosomes in the presence of calcium, cadherins are ordered, but desmosome proteins are unable to diffuse in or out of the complex. (D) In the absence of calcium, the cadherins in hyperadhesive desmosomes become disordered. Adhesion is maintained because desmosome proteins are unable to diffuse out of the complex.

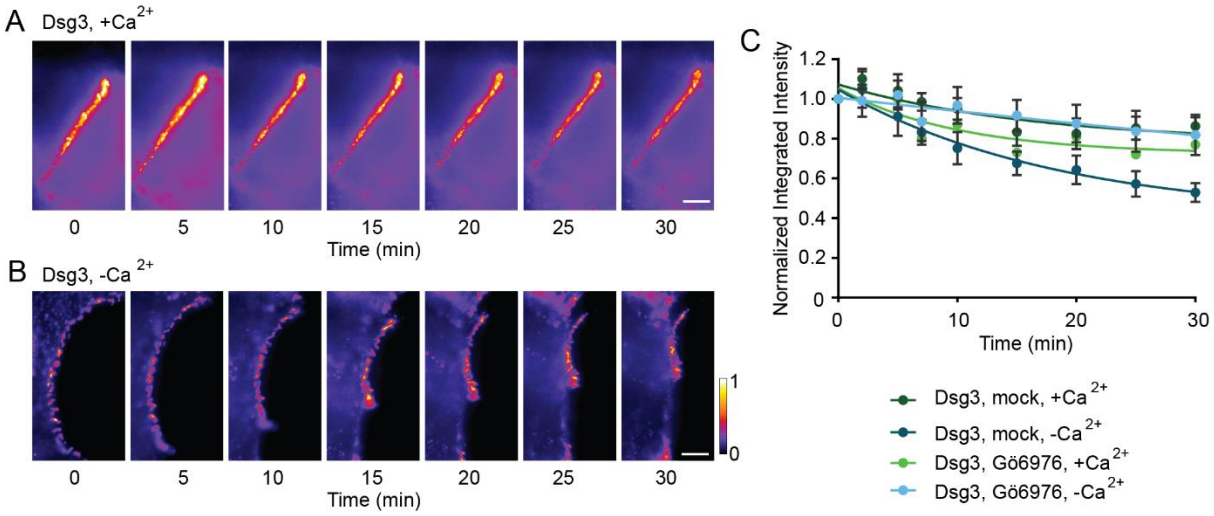

Supplemental Figure 11. Dsg3 diffuses out of calcium-dependent desmosomes in the absence of calcium. HaCaT cells were transfected with Dsg3-ΔEA-GFP, mock treated, either maintained in (A) normal calcium media (NCM) or (B) switched into low calcium media (LCM) and imaged for 30 min. Representative intensity images at each time point are shown pseudo-colored by intensity. (C) Intensity over time was quantified by masking each image based on intensity and calculating the integrated intensity (sum of each pixel intensity) within the mask. Integrated intensity was normalized and averaged across the population of cells. Cells, either mock (n=6) or Gö6976 (n=6) treated and maintained in NCM show a slight decrease in intensity over time due to photobleaching. In comparison, calcium-dependent desmosomes switched into LCM (n=11) have a significantly larger decrease in integrated intensity at 30 min. Cells treated with Gö6976 and switched into LCM (n=15) show a decrease in intensity not significantly different from cells maintained in NCM ($p \leq 0.01$).

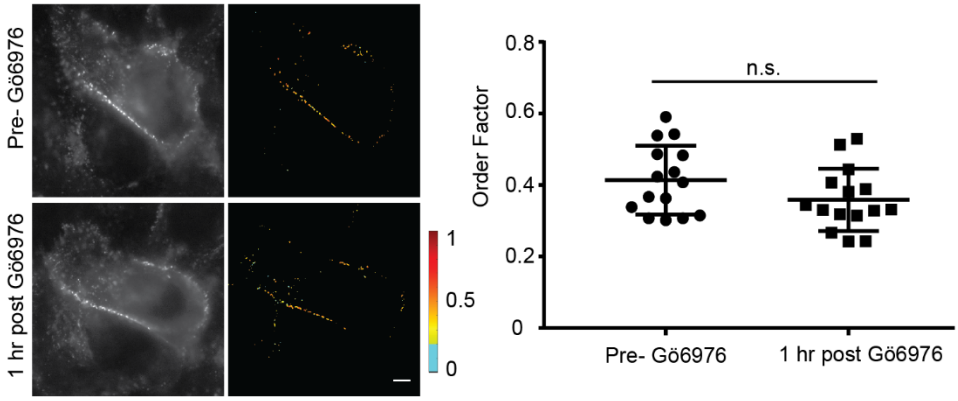

Supplemental Figure 12. Gö6976 does not alter Dsg3 order factor. HaCaT cells transfected with Dsg3-ΔEA-GFP were imaged by fluorescence polarization microscopy and order factor was measured. Following treatment with Gö6976 (1 hr) the same cells were reimaged (scale bar= 5μm). Order factor between pre- and post- treatment images (n= 15) was not significantly different by Student's t-test (ns).

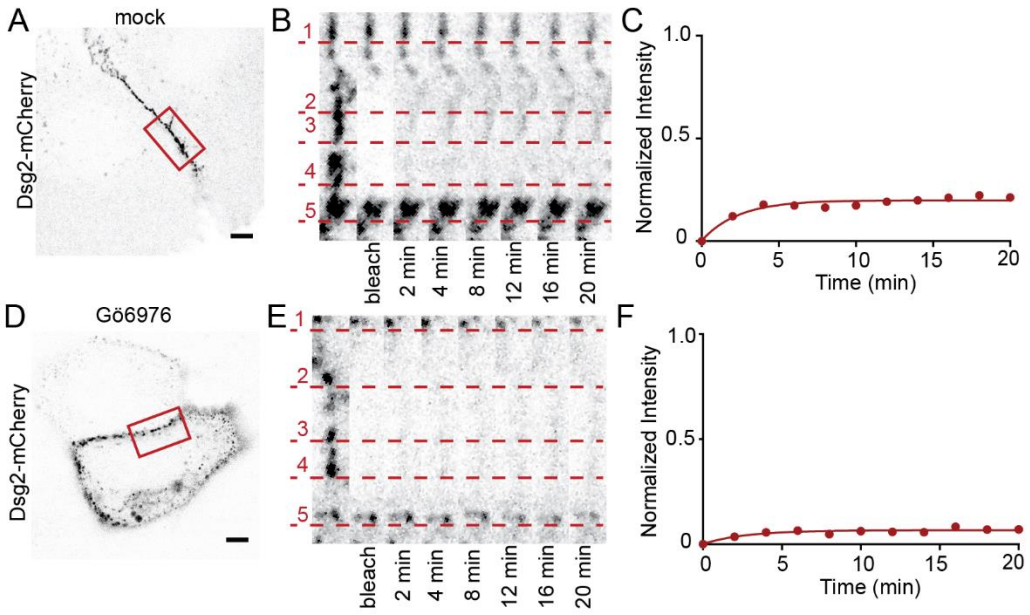

Supplemental Figure 13. Dsg2 recovery following photobleaching is dependent on adhesive state. Representative cells from data presented in Fig 5. (A) Representative HaCaT cell transfected with Dsg2-mCherry and mock treated with bleach (red) ROIs indicated. Scale bar = 5μm. (B) Zoom in of cell boarder in bleach ROI over time. Recovery of individual puncta is underscored by the dashed lines. (C) Fluorescence intensity was plotted and showed a mobile fraction of 20%. (D) Representative HaCaT cell transfected with Dsg2-mCherry and Gö6976 treated. Scale bar= 5μm (E) Recovery of individual puncta is underscored by the dashed lines. (F) Fluorescence intensity was plotted and showed a mobile fraction of 7%.

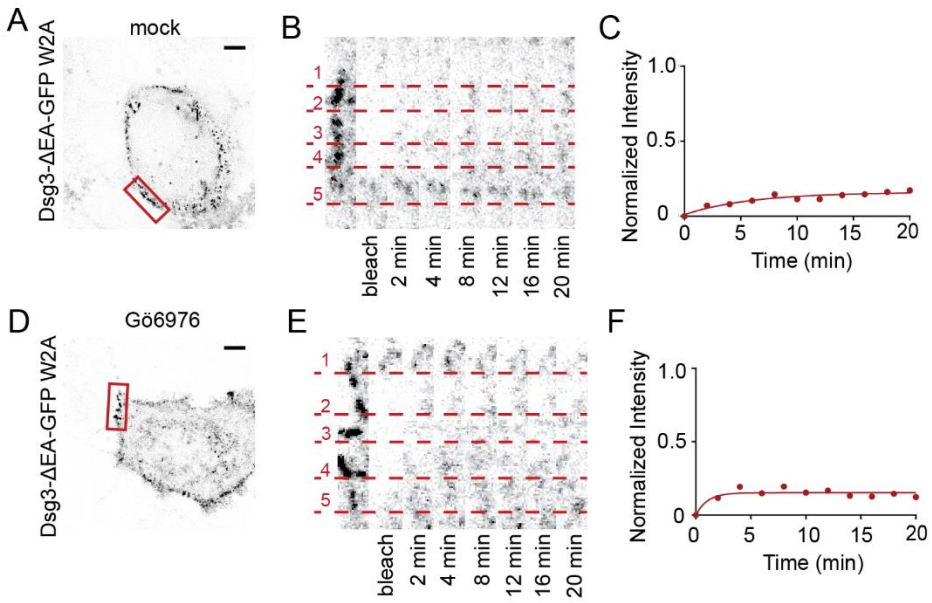

Supplemental Figure 14. Dsg3-W2A-GFP recovers in both calcium dependent and hyperadhesive desmosomes. Representative cells from data presented in Fig 6. (A) Representative HaCaT cell transfected with Dsg3-ΔEA-GFP W2A and mock treated with bleach (red) and control (orange) ROIs indicated. Scale bar = 5μm. (B) Zoom in of cell border in bleach ROI over time. Recovery of individual puncta is underscored by the dashed lines. (C) Fluorescence intensity was plotted and fit to a one-phase association curve to determine the $t_{1/2}$ was 4.1 min. (D) Representative HaCaT cell transfected with Dsg3-ΔEA-GFP W2A and Gö6976 treated. Scale bar= 5μm (E) A region of desmosomes was bleached and recovery was tracked over time. Recovery of individual puncta is underscored by the dashed lines. (F) Dsg3-W2A with Gö6976 in LCM exhibited significant recovery with a $t_{1/2}$ of 0.7 min.

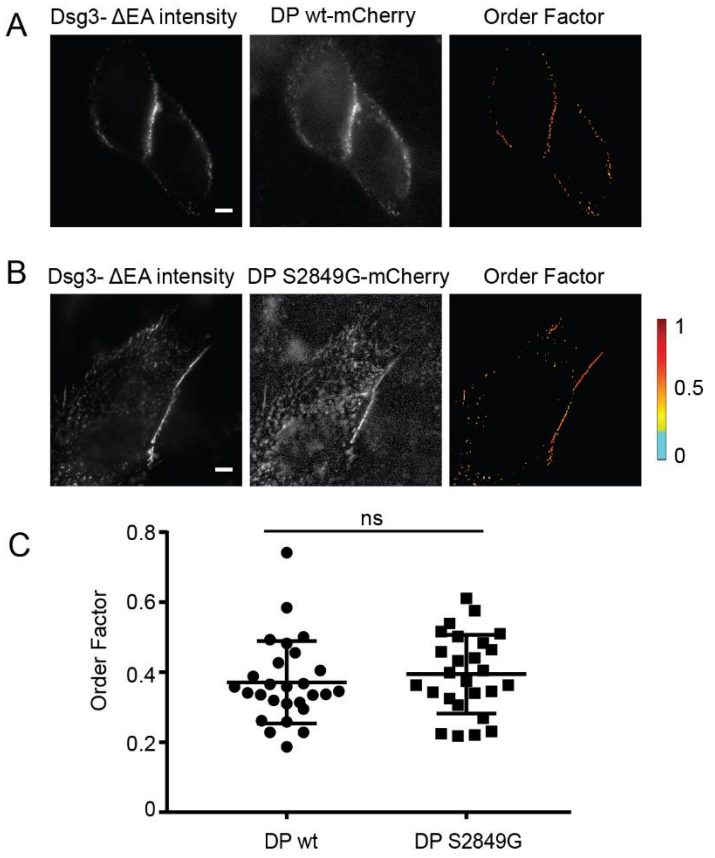

Supplemental Figure 15. Co-expression of DP S2849G does not change Dsg3 order factor. (A) Representative HaCaT cell co-transfected with Dsg3-ΔEA-GFP and DP-wt-mCherry were imaged with fluorescence polarization microscopy. Scale bar= 5μm (B) HaCaT cells were co-transfected with Dsg3-ΔEA-GFP and DP-S2849G-mCherry and imaged with fluorescence polarization microscopy. Scale bar= 5μm. (C) Expression of DP S2849G-mCherry (n = 26) compared to DP-wt (n=27) resulted in no significant change in Dsg3 order by Student's T-test (ns).

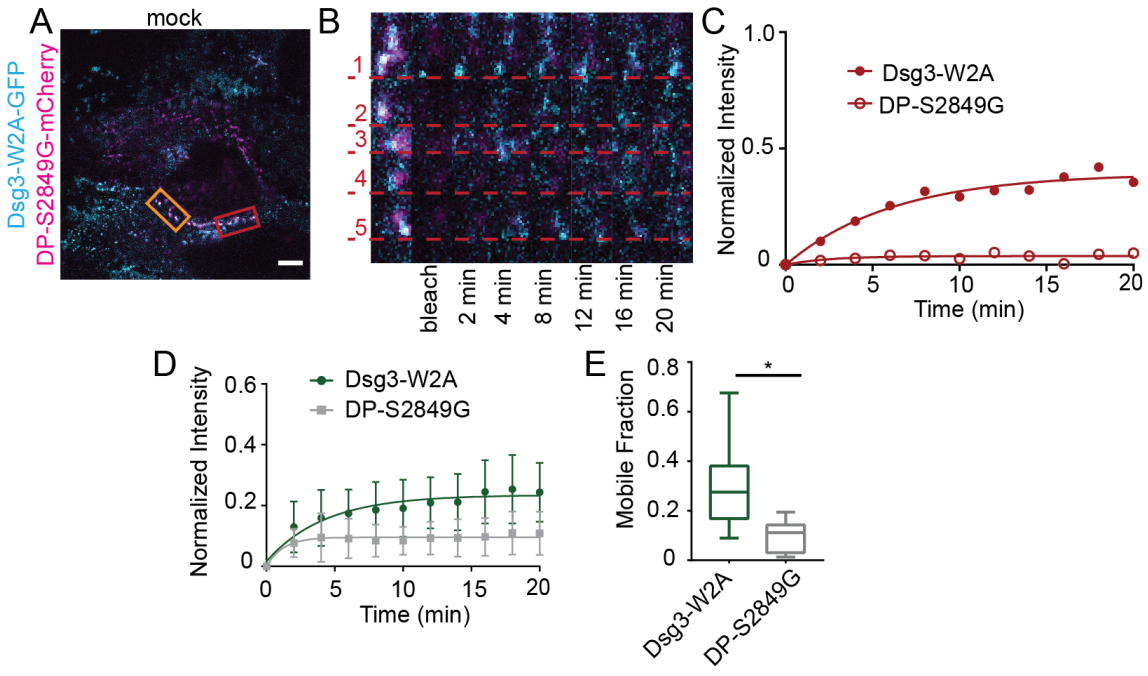

Supplemental Figure 16. Co-expression of DP S2849G with Dsg3-W2A results in hyperadhesive desmosomes where Dsg3-W2A is mobile. (A) Dsg3-W2A was co-transfected with DP-S2849G-mCherry. (B) Recovery was tracked over time in both channels with significant recovery of Dsg3-W2A and negligible recovery of DP-S2849G. (C) Bleach region intensity was normalized and fit to a one-phase association, resulting in a 39% recovery and a $t_{1/2}$ of 4.2 min for Dsg3-W2A and a 4% recovery and a $t_{1/2}$ of 1.7 min for DP-S2849G. (D) Intensity over time for a population of cells was averaged, fit to a curve, and used to calculate a $t_{1/2}$ of 2.1 min for Dsg3-W2A and 1.7 min for DP S2849G. (E) Mean mobile fraction for the population of curves was 30±18% for Dsg3-W2A and 10±7% for DP S2849G. Significance was determined by Student's t-test (* $p<0.05$)

Chapter 7

Summary and future directions

In this dissertation the overall aim was to develop and apply novel optical techniques to investigate the relationship between desmosome molecular architecture and adhesive function. While the structure of macromolecular complexes is generally accepted to inform and contribute to their functions, we have lacked the tools to directly investigate these principles *in situ*. Integrating information across many scales including protein (angstrom), macromolecular complex (nanometer), cell (micrometer), and tissue (millimeter) scales is a significant challenge in biology. The work in this dissertation utilized advanced imaging modalities with the objective of bridging this gap in desmosomes. First, I measured the nanoscale organization of desmosomal plaque components in primary human keratinocytes, cell culture models, and in control human epidermis. Second, I explored the ordering of the desmosomal cadherin Dsg3 in the extracellular space in a living cell culture model. Finally, I integrated these analyses to investigate the role of order and organization as it contributes to desmosome hyperadhesion. The collection of work presented in this dissertation illustrates that desmosome organization is highly conserved regardless of cell type or adhesive state. Furthermore, while desmosomes are endogenously ordered, neither cadherin order nor desmosome organization are significantly different between adhesive states. Ultimately, I concluded that desmosome structure and function are not sufficient to understand the complexities of desmosome adhesion. Desmosome dynamics also plays a crucial role in adhesive function and, in fact, is the mechanism controlling hyperadhesion. The studies here have addressed long-standing questions in the desmosome field and have also led to a myriad of new questions that we now have the tools to investigate.

7.1 How does the nanoscale organization of the desmosome contribute to adhesive function?

The work in Chapter 4 of this dissertation demonstrated that desmosomes have a highly organized molecular architecture. I used a super-resolution fluorescence microscopy technique (dSTORM) which permitted measurements to be made in both cells and tissue sections. The mirror symmetry of the desmosome allowed for the architecture to be quantified by linescans across the plasma membrane, or perpendicular to the axis of symmetry. Since the plaque-to-plaque distance measured by these linescans was consistent between sample types, we can utilize this method to investigate desmosome structure in cell culture or mouse models and be confident in the relevance to human skin biology.

I applied dSTORM in both Chapter 4 and Chapter 6 to study the molecular architecture of the desmosome in hyperadhesion. In Chapter 4, I used a viral overexpression of plakophilin-1 (Pkp-1), which results in calcium-independent desmosomes that are significantly longer than normal. This is consistent with the *in vivo* localization of Pkp-1, which is enriched in the upper layers of the skin, where desmosomes are also found to be longer and more abundant than in the basal layer (Hatzfeld et al., 2000). I further determined that overexpression of Pkp-1 results in a conformational change of desmoplakin (DP), where the c-term and rod domains of DP rearrange closer to the plasma membrane. Because of this result, I hypothesized that changes in plaque architecture could determine adhesive strength. However, in Chapter 6, when I induced hyperadhesion by inhibiting PKCα, I found no change in plaque architecture. This indicates that the changing architecture is a byproduct of protein overexpression and not the mechanism of hyperadhesion. Future work should continue evaluating the architecture of different types of hyperadhesion, including cell confluency, to fully elucidate the role of changes in protein organization for adhesive function.

Another application for future work using dSTORM could expand on the previous SIM analysis of desmosomes in disease states, like in the presence of Pemphigus vulgaris (PV) antibodies. The Kowalczyk lab used SIM to investigate the architecture and composition of unique structures, called linear arrays, that form in response to PV IgG and act as sites of desmosome internalization (Stahley et al., 2014). Understanding the nanoscale architecture within these structures at an even higher resolution than SIM could help further elucidate their function. Are desmosomes split along the plasma membrane when linear arrays form? Or does the internalization maintain the double membrane structure and engulf part of the neighboring cell? In addition to linear arrays, I hypothesize that the normal architecture of the desmosome becomes disrupted during the process of PV-induced disassembly. Both steric hindrance and signaling processes have been implicated in PV disruption (Kitajima, 2013) and changes in plaque architecture could help unravel the distinction. For instance, measuring plaque-to-plaque distances in PV-bound desmosomes with and without inhibiting the involved signaling pathways (ie MAPK) would shed new light on the mechanism of PV disruption. Super resolution microscopy, and specifically dSTORM, is poised to study this mechanism.

Another interesting feature that has been noted during dSTORM imaging experiments is that desmosome architecture is slightly varied across sub-confluent cells, depending upon whether the cells are at the center or periphery of an island. While the architecture at the center of the cell cluster matches that measured in skin sections, desmosomes in cells at the edge of clusters exhibit significantly wider plaque-to-plaque distances (Stahley, Bartle, and Mattheyses; *unpublished*). To account for these differences, the lab decided upon a neighbors-of-neighbors rule, where all cells imaged by dSTORM must have a neighbor at every edge and all of those cells must also be surrounded by neighbors. However, by ignoring the population of cells at the

edge of cell islands, I neglect a potentially biologically significant structural feature. Why are desmosomal plaques in peripheral cells wider?

One hypothesis to explain the desmosome widening at the periphery is that immature desmosomes exhibit the wider phenotype. To explore this idea, a wound healing model could be used to synchronize cell migration, proliferation, and desmosome assembly. If plaque architecture reflects the maturation of desmosomes, I would anticipate that desmosomes at the wound edge would become wider following wounding. Given the results in chapter 6 that plaque-to-plaque distance is not impacted by adhesive strength, I hypothesize that existing desmosomes will be unaffected regardless of their adhesive state. However, newly forming desmosomes in the migrating cells would likely exhibit wider plaque distances. After migration, when the wound is closed, architecture should be re-established with normal plaque distances. If desmosome plaque width corresponds to desmosome maturation, plaque-to-plaque distance then becomes an assay for *in vivo* analysis of desmosome adhesive state, which would be particularly useful in diseased patient tissue or mouse models of desmosomes-related diseases.

7.2 What is the role of cadherin order in desmosome adhesion?

As described in Chapters 5 and 6, order has been thought to be important for adhesion because of the electron dense structures observed by EM. Since the dense midline is only found in EM of hyperadhesive desmosomes, the increased density was attributed to an increase in cadherin order. Using fluorescence polarization microscopy provided a unique opportunity for studying desmosome order. I measured a sub-diffraction resolution architectural property of the desmosome using a diffraction limited technique and I did so in living cells, eliminating potential fixation artifacts that could mimic an ordered array.

I found that desmosomes in living cells are ordered and order decreases when desmosomes disassemble in the absence of calcium. Interestingly, I observed that order decreased prior to loss of adhesion, as determined by a dispase fragmentation assay. This result hinted that desmosomes could be adhesive while disordered. Further work supported this preliminary hypothesis and showed (1) no increase in order when hyperadhesion was induced and (2) desmosomal cadherins were capable of being simultaneously adherent and disordered. The calcium switch assay used to test adhesive state and induce disorder is not an endogenous system but is informative for understanding the structure-function relationship of the desmosome. These results suggested that order is a natural property of adherent desmosomes, but it is not necessary for adhesive function. This outcome leads to several new questions about cadherin order: how is order established? Do disease states result in cadherin disordering? In the presence of calcium, can order be used to assess adhesive function?

To address these questions, future work should examine order in desmosome assembly. There are two likely hypotheses for how order is established. First, it is possible that order is a product of desmosome maturation. During assembly it is known that adherens junction and desmosome components are initially mixed and segregate into individual junctions as they mature (Lowndes et al., 2014; Shafraz et al., 2018). This process of segregation may be necessary for establishing cadherin order. Second, it is possible that order is established earlier, upon translocation of the cadherins to the cell membrane. Simply the integration of the cadherins into clusters prior to segregation, regardless of the type of cadherins involved, may be sufficient to induce order (Fink et al., 2012; Moore et al., 2008). While I showed that transbinding is essential for desmosome order, transbinding and incorporation into the plasma membrane may

be the only requirements. My result showing that cadherins cannot regain order once it has been lost indicates that the assembly process is necessary for establishing order.

Though I showed that order is not necessary for adhesion, order as a physical property may still be informative for improving our understanding of desmosome biology. Exploring order during assembly or in states of desmosomal disease can increase our knowledge of desmosome ultrastructure.

7.3 How can the physical properties of desmosomes inform the study of cell functions?

While Chapters 4 and 5 elucidated nanoscale features of desmosome architecture, including desmosome plaque structure and cadherin order, it is important to understand how these features impact desmosome function. Chapter 6 explored the relationship between desmosome physical features and the hyperadhesive state. I found that changes in structure were less important for function than changes in protein mobility. This provided an important lesson for future studies of macromolecular complexes, where dynamics should be weighted as equally important as structure in the biological conclusions.

These results support a role for desmosomes as a depot of cell signaling, as described by Ray et al (Ray et al., 2007), where proteins dissociated from the desmosome play a critical role in the regulation of the complex. The diffusion of proteins in and out of the desmosome complex may have signaling consequences that support calcium-dependent adhesion, in addition to the structural impacts. For instance, it has been shown that the mislocalization of desmosomal proteins away from the plasma membrane both reduces desmosome number and alters cell processes like migration and proliferation (Wang et al., 2018). Conversely, hyperadhesion may also have signaling consequences, where loss of mobility blocks the depot function of the complex and prevents cell signaling. Future work differentiating the downstream signaling

impacts from the physical structure will further elucidate the complex role of desmosome adhesion.

Since I determined that desmosome hyperadhesion is the result of protein stabilization, or loss of mobility, future work should exploit this phenotype to measure adhesive strength in living cells without perturbing the sample. By conducting FRAP experiments to measure protein dynamics, the adhesive strength of desmosomes could be determined on not only a cell-by-cell basis but by individual desmosome. Given the relative ease of access of FRAP, compared to dSTORM or fluorescence polarization microscopy, this assay is poised to be widely accessible to the desmosome field for measuring adhesive function.

Basic biology questions that could be addressed using this approach in future work are numerous. Can I induce hyperadhesion by making the cadherins less mobile, or is desmoplakin mobility more important? The Dsg2 ARVC mutation that exhibits increased adhesive strength (Dieding et al., 2017) would be an interesting model for this question, as well as suggesting cadherin mutation sites that could control adhesive strength. Could I induce hyperadhesion in adherens junctions (which endogenously do not adopt a hyperadhesive state) by blocking protein mobility through similar mechanisms? Can I use inhibitors to dynamically control adhesive state; ie switch desmosomes from calcium-dependent to hyperadhesive and back to calcium-dependent?

These approaches will also allow for novel analysis of desmosome strength in disease models. What is the role of desmosome dynamics in disease? With the complexity of desmosome regulation in cancer, changes in protein dynamics may be able to rapidly predict if mutations or protein overexpression results in a pro-proliferative (more dynamic) or pro-adhesive (less dynamic) phenotype for a screening assay. The importance of dynamics for

adhesion sheds new light on our understanding of PV. It was previously established that hyperadhesion is protective against desmosome disruption in response to PV IgG (Cirillo et al., 2010; Tucker et al., 2014). It is also known that cadherin endocytosis plays an important role in PV IgG induced disassembly (Calkins et al., 2006; Saito et al., 2012; Stahley et al., 2016b). Together those results suggest that hyperadhesive desmosomes are resistant to PV because the cadherins cannot be internalized and depleted from the membrane.

Another model that will benefit from being studied in the context of protein dynamics is wound healing. Unlike in the PV model where blocking protein mobility is protective, wound healing first requires an increase in protein dynamics followed by re-establishment of immobile, or hyperadhesive desmosomes. Understanding how to promote desmosome protein dynamics could accelerate wound healing and lead to new targets for treatment. For instance, perhaps a one-time topical treatment of a PKCα activator immediately after injury would jump-start the wound healing process. Studying hyperadhesion and dynamics in the context of diseases of skin fragility has the power to yield new diagnostic and treatment tools.

7.4 Concluding remarks

The studies in this dissertation have made a significant contribution to the field of desmosome biology by revealing the organization of the desmosomal components and elucidating the role of structure in adhesive function. Many of the results in this work are counter to the hypotheses that originated from past electron microscopy studies. However, the advanced imaging techniques allowed me to achieve a previously unattainable resolution and level of detail with molecular specificity. Measuring desmosome order, ultrastructural properties like plaque-to-plaque distance, and protein dynamics allowed me to bridge the gap between protein

structure, macromolecular complex organization, and cell function. This increased understanding of the importance of not just desmosome architecture, but also dynamics, and how these properties confer adhesive function will inform future work on desmosome biology and desmosome-related diseases.

References

Abbe, E. 1882. The Relation of Aperture and Power in the Microscope*. *Journal of the Royal Microscopical Society*. 2:300-309.

Agullo-Pascual, E., M. Cerrone, and M. Delmar. 2014a. Arrhythmogenic cardiomyopathy and Brugada syndrome: diseases of the connexome. *FEBS Lett.* 588:1322-1330.

Agullo-Pascual, E., X. Lin, A. Leo-Macias, M. Zhang, F.-X. Liang, Z. Li, A. Pfenniger, I. Lübkemeier, S. Keegan, D. Fenyö, K. Willecke, E. Rothenberg, and M. Delmar. 2014b. Super-resolution imaging reveals that loss of the C-terminus of connexin43 limits microtubule plus-end capture and NaV1.5 localization at the intercalated disc. *Cardiovasc. Res.* 104:371-381.

Agullo-Pascual, E., X. Lin, A. Leo-Macias, M. Zhang, F.X. Liang, Z. Li, A. Pfenniger, I. Lubkemeier, S. Keegan, D. Fenyo, K. Willecke, E. Rothenberg, and M. Delmar. 2014c. Super-resolution imaging reveals that loss of the C-terminus of connexin43 limits microtubule plus-end capture and NaV1.5 localization at the intercalated disc. *Cardiovasc Res*. 104:371-381.

Agullo-Pascual, E., D.A. Reid, S. Keegan, M. Sidhu, D. Fenyo, E. Rothenberg, and M. Delmar. 2013a. Super-resolution fluorescence microscopy of the cardiac connexome reveals plakophilin-2 inside the connexin43 plaque. *Cardiovasc Res*. 100:231-240.

Agullo-Pascual, E., D.A. Reid, S. Keegan, M. Sidhu, D. Fenyö, E. Rothenberg, and M. Delmar. 2013b. Super-resolution fluorescence microscopy of the cardiac connexome reveals plakophilin-2 inside the connexin43 plaque. *Cardiovasc. Res.* 100:231-240.

Al-Amoudi, A., D. Castano-Diez, D.P. Devos, R.B. Russell, G.T. Johnson, and A.S. Frangakis. 2011. The three-dimensional molecular structure of the desmosomal plaque. *Proc Natl Acad Sci U S A*. 108:6480-6485.

Al-Amoudi, A., J.-J. Chang, A. Leforestier, A. McDowall, L.M. Salamin, L.P.O. Norlén, K. Richter, N.S. Blanc, D. Studer, and J. Dubochet. 2004. Cryo-electron microscopy of vitreous sections. *EMBO J*. 23:3583-3588.

Al-Amoudi, A., D.C. Diez, M.J. Betts, and A.S. Frangakis. 2007. The molecular architecture of cadherins in native epidermal desmosomes. *Nature*. 450:832-837.

Al-Amoudi, A., J. Dubochet, and L. Norlen. 2005. Nanostructure of the epidermal extracellular space as observed by cryo-electron microscopy of vitreous sections of human skin. *J Invest Dermatol*. 124:764-777.

Al-Amoudi, A., and A.S. Frangakis. 2008. Structural studies on desmosomes. *Biochem Soc Trans*. 36:181-187.

Al-Jassar, C., T. Knowles, M. Jeeves, K. Kami, E. Behr, H. Bikker, M. Overduin, and M. Chidgey. 2011. The nonlinear structure of the desmoplakin plakin domain and the effects of cardiomyopathy-linked mutations. *J Mol Biol*. 411:1049-1061.

Alazawi, W.O., L.S. Morris, M.A. Stanley, D.R. Garrod, and N. Coleman. 2003. Altered expression of desmosomal components in high-grade squamous intraepithelial lesions of the cervix. *Virchows Arch*. 443:51-56.

Albrecht, L.V., L. Zhang, J. Shabanowitz, E. Purevjav, J.A. Towbin, D.F. Hunt, and K.J. Green. 2015. GSK3- and PRMT-1-dependent modifications of desmoplakin control desmoplakin-cytoskeleton dynamics. *J Cell Biol*. 208:597-612.

Alroy, J., B.U. Pauli, and R.S. Weinstein. 1981. Correlation between numbers of desmosomes and the aggressiveness of transitional cell carcinoma in human urinary bladder. *Cancer*. 47:104-112.

Amagai, M. 1999. Autoimmunity against desmosomal cadherins in pemphigus. *J Dermatol Sci*. 20:92-102.

Amagai, M., V. Klaus-Kovtun, and J.R. Stanley. 1991. Autoantibodies against a novel epithelial cadherin in pemphigus vulgaris, a disease of cell adhesion. *Cell*. 67:869-877.

Andrea Hartsock, W.J.N. 2008. Adherens and Tight Junctions: Structure, Function and Connections to the Actin Cytoskeleton. *Biochim. Biophys. Acta*. 1778:660.

Arimoto, K., C. Burkart, M. Yan, D. Ran, S. Weng, and D.E. Zhang. 2014. Plakophilin-2 promotes tumor development by enhancing ligand-dependent and -independent epidermal growth factor receptor dimerization and activation. *Mol Cell Biol*. 34:3843-3854.

Atkinson, C.E., A.L. Mattheyses, M. Kampmann, and S.M. Simon. 2013. Conserved spatial organization of FG domains in the nuclear pore complex. *Biophysical journal*. 104:37-50.

Axelrod, D. 1979. Carbocyanine dye orientation in red cell membrane studied by microscopic fluorescence polarization. *Biophysical journal*. 26:557-573.

Baker, S.M., R.W. Buckheit, 3rd, and M.M. Falk. 2010. Green-to-red photoconvertible fluorescent proteins: tracking cell and protein dynamics on standard wide-field mercury arc-based microscopes. *BMC Cell Biol*. 11:15.

Bartle, E.I., T.M. Urner, S.S. Raju, and A.L. Mattheyses. 2017. Desmoglein 3 Order and Dynamics in Desmosomes Determined by Fluorescence Polarization Microscopy. *Biophysical journal*. 113:2519-2529.

Bass-Zubek, A.E., L.M. Godsel, M. Delmar, and K.J. Green. 2009. Plakophilins: multifunctional scaffolds for adhesion and signaling. *Curr Opin Cell Biol*. 21:708-716.

Bass-Zubek, A.E., and K.J. Green. 2007. Biochemical Characterization of the Desmosome. *J Invest Dermatol*. 127 Suppl 3:E4-5.

Bass-Zubek, A.E., R.P. Hobbs, E.V. Amargo, N.J. Garcia, S.N. Hsieh, X. Chen, J.K. Wahl, 3rd, M.F. Denning, and K.J. Green. 2008. Plakophilin 2: a critical scaffold for PKC alpha that regulates intercellular junction assembly. *J Cell Biol*. 181:605-613.

Basso, C., B. Bauce, D. Corrado, and G. Thiene. 2012. Pathophysiology of arrhythmogenic cardiomyopathy. *Nat Rev Cardiol*. 9:223-233.

Bates, M., B. Huang, G.T. Dempsey, and X. Zhuang. 2007. Multicolor super-resolution imaging with photo-switchable fluorescent probes. *Science*. 317:1749-1753.

Beaudry, V.G., R.A. Ihrie, S.B. Jacobs, B. Nguyen, N. Pathak, E. Park, and L.D. Attardi. 2010. Loss of the desmosomal component perp impairs wound healing in vivo. *Dermatol Res Pract*. 2010:759731.

Beck, M., and E. Hurt. 2017. The nuclear pore complex: understanding its function through structural insight. *Nat Rev Mol Cell Biol*. 18:73-89.

Beghein, E., and J. Gettemans. 2017. Nanobody Technology: A Versatile Toolkit for Microscopic Imaging, Protein–Protein Interaction Analysis, and Protein Function Exploration. *Front. Immunol.* 8.

Berika, M., and D. Garrod. 2014. Desmosomal adhesion in vivo. *Cell Commun. Adhes.* 21:65-75.

Bertocchi, C., Y. Wang, A. Ravasio, Y. Hara, Y. Wu, T. Sailov, M.A. Baird, M.W. Davidson, R. Zaidel-Bar, Y. Toyama, B. Ladoux, R.-M. Mege, and P. Kanchanawong. 2017a. Nanoscale architecture of cadherin-based cell adhesions. *Nat. Cell Biol.* 19:28-37.

Bertocchi, C., Y. Wang, A. Ravasio, Y. Hara, Y. Wu, T. Sailov, M.A. Baird, M.W. Davidson, R. Zaidel-Bar, Y. Toyama, B. Ladoux, R.M. Mege, and P. Kanchanawong. 2017b. Nanoscale architecture of cadherin-based cell adhesions. *Nat Cell Biol*. 19:28-37.

Betzig, E., G.H. Patterson, R. Sougrat, O.W. Lindwasser, S. Olenych, J.S. Bonifacino, M.W. Davidson, J. Lippincott-Schwartz, and H.F. Hess. 2006. Imaging intracellular fluorescent proteins at nanometer resolution. *Science*. 313:1642-1645.

Bianchini, P., F. Cardarelli, M. Di Luca, A. Diaspro, and R. Bizzarri. 2014. Nanoscale protein diffusion by STED-based pair correlation analysis. *PLoS One*. 9:e99619.

Boggon, T.J., J. Murray, S. Chappuis-Flament, E. Wong, B.M. Gumbiner, and L. Shapiro. 2002. C-cadherin ectodomain structure and implications for cell adhesion mechanisms. *Science*. 296:1308-1313.

Bondia, P., S. Casado, and C. Flors. 2017. Correlative Super-Resolution Fluorescence Imaging and Atomic Force Microscopy for the Characterization of Biological Samples. *In* Methods in Molecular Biology. 105-113.

Bornslaeger, E.A., C.M. Corcoran, T.S. Stappenbeck, and K.J. Green. 1996. Breaking the connection: displacement of the desmosomal plaque protein desmoplakin from cell-cell interfaces disrupts anchorage of intermediate filament bundles and alters intercellular junction assembly. *J Cell Biol*. 134:985-1001.

Bornslaeger, E.A., L.M. Godsel, C.M. Corcoran, J.K. Park, M. Hatzfeld, A.P. Kowalczyk, and K.J. Green. 2001. Plakophilin 1 interferes with plakoglobin binding to desmoplakin, yet together with plakoglobin promotes clustering of desmosomal plaque complexes at cell-cell borders. *J Cell Sci*. 114:727-738.

Brejc, K., T.K. Sixma, P.A. Kitts, S.R. Kain, R.Y. Tsien, M. Ormo, and S.J. Remington. 1997. Structural basis for dual excitation and photoisomerization of the Aequorea victoria green fluorescent protein. *Proc Natl Acad Sci U S A*. 94:2306-2311.

Brennan, D., Y. Hu, S. Joubeh, Y.W. Choi, D. Whitaker-Menezes, T. O'Brien, J. Uitto, U. Rodeck, and M.G. Mahoney. 2007. Suprabasal Dsg2 expression in transgenic mouse skin confers a hyperproliferative and apoptosis-resistant phenotype to keratinocytes. *J Cell Sci*. 120:758-771.

Brennan, D., and M.G. Mahoney. 2009. Increased expression of Dsg2 in malignant skin carcinomas: A tissue-microarray based study. *Cell Adh Migr*. 3:148-154.

Breuninger, S., S. Reidenbach, C.G. Sauer, P. Strobel, J. Pfitzenmaier, L. Trojan, and I. Hofmann. 2010. Desmosomal plakophilins in the prostate and prostatic adenocarcinomas: implications for diagnosis and tumor progression. *Am J Pathol*. 176:2509-2519.

Brooke, M.A., D. Nitoiu, and D.P. Kelsell. 2012. Cell-cell connectivity: desmosomes and disease. *J Pathol*. 226:158-171.

Broussard, J.A., S. Getsios, and K.J. Green. 2015. Desmosome regulation and signaling in disease. *Cell Tissue Res*. 360:501-512.

Brown, C.M. 2007. Fluorescence microscopy - avoiding the pitfalls. *J. Cell Sci.* 120:1703-1705.

Brown, J.K., A.D. Pemberton, S.H. Wright, and H.R.P. Miller. 2004. Primary Antibody–Fab Fragment Complexes: A Flexible Alternative to Traditional Direct and Indirect Immunolabeling Techniques. *J. Histochem. Cytochem.* 52:1219-1230.

Burdett, I.D. 1993. Internalisation of desmosomes and their entry into the endocytic pathway via late endosomes in MDCK cells. Possible mechanisms for the modulation of cell adhesion by desmosomes during development. *J Cell Sci*. 106 (Pt 4):1115-1130.

Calkins, C.C., and S.V. Setzer. 2007. Spotting Desmosomes: The First 100 Years. *J Invest Dermatol*. 127 Suppl 3:E2-3.

Calkins, C.C., S.V. Setzer, J.M. Jennings, S. Summers, K. Tsunoda, M. Amagai, and A.P. Kowalczyk. 2006. Desmoglein endocytosis and desmosome disassembly are coordinated responses to pemphigus autoantibodies. *J Biol Chem*. 281:7623-7634.

Calore, M., A. Lorenzon, M. De Bortoli, G. Poloni, and A. Rampazzo. 2015. Arrhythmogenic cardiomyopathy: a disease of intercalated discs. *Cell Tissue Res*. 360:491-500.

Canel, M., A. Serrels, D. Miller, P. Timpson, B. Serrels, M.C. Frame, and V.G. Brunton. 2010. Quantitative in vivo imaging of the effects of inhibiting integrin signaling via Src and FAK on cancer cell movement: effects on E-cadherin dynamics. *Cancer Res*. 70:9413-9422.

Cao, J., and H. Schnittler. 2019. Putting VE-cadherin into JAIL for junction remodeling. *J Cell Sci*. 132.

Celentano, A., and N. Cirillo. 2017. Desmosomes in disease: a guide for clinicians. *Oral Dis*. 23:157-167.

Cerrone, M., and M. Delmar. 2014. Desmosomes and the sodium channel complex: implications for arrhythmogenic cardiomyopathy and Brugada syndrome. *Trends Cardiovasc. Med.* 24:184-190.

Chatel, G., S.H. Desai, A.L. Mattheyses, M.A. Powers, and B. Fahrenkrog. 2012. Domain topology of nucleoporin Nup98 within the nuclear pore complex. *J Struct Biol*. 177:81-89.

Chen, X., S. Bonne, M. Hatzfeld, F. van Roy, and K.J. Green. 2002. Protein binding and functional characterization of plakophilin 2. Evidence for its diverse roles in desmosomes and beta -catenin signaling. *J Biol Chem*. 277:10512-10522.

Chen, Y.J., J.T. Chang, L. Lee, H.M. Wang, C.T. Liao, C.C. Chiu, P.J. Chen, and A.J. Cheng. 2007. DSG3 is overexpressed in head neck cancer and is a potential molecular target for inhibition of oncogenesis. *Oncogene*. 26:467-476.

Chidgey, M., and C. Dawson. 2007. Desmosomes: a role in cancer? *Br J Cancer*. 96:1783-1787.

Chitaev, N.A., R.E. Leube, R.B. Troyanovsky, L.G. Eshkind, W.W. Franke, and S.M. Troyanovsky. 1996. The binding of plakoglobin to desmosomal cadherins: patterns of binding sites and topogenic potential. *J Cell Biol*. 133:359-369.

Choi, H.J., J.C. Gross, S. Pokutta, and W.I. Weis. 2009. Interactions of plakoglobin and beta-catenin with desmosomal cadherins: basis of selective exclusion of alpha- and beta-catenin from desmosomes. *J Biol Chem*. 284:31776-31788.

Choi, H.J., S. Park-Snyder, L.T. Pascoe, K.J. Green, and W.I. Weis. 2002. Structures of two intermediate filament-binding fragments of desmoplakin reveal a unique repeat motif structure. *Nat Struct Biol*. 9:612-620.

Cirillo, N., A. Lanza, and S.S. Prime. 2010. Induction of hyper-adhesion attenuates autoimmune-induced keratinocyte cell-cell detachment and processing of adhesion molecules via mechanisms that involve PKC. *Exp Cell Res*. 316:580-592.

Cole, N.B., C.L. Smith, N. Sciaky, M. Terasaki, M. Edidin, and J. Lippincott-Schwartz. 1996. Diffusional mobility of Golgi proteins in membranes of living cells. *Science*. 273:797-801.

Cooper, G. 2000. The Cell: A Molecular Approach. Sinauer Associates, Sunderland (MA).

Cowin, P., and D.R. Garrod. 1983. Antibodies to epithelial desmosomes show wide tissue and species cross-reactivity. *Nature*. 302:148-150.

Cowin, P., H.P. Kapprell, W.W. Franke, J. Tamkun, and R.O. Hynes. 1986. Plakoglobin: a protein common to different kinds of intercellular adhering junctions. *Cell*. 46:1063-1073.

Cowin, P., D. Mattey, and D. Garrod. 1984. Identification of desmosomal surface components (desmocollins) and inhibition of desmosome formation by specific Fab'. *J Cell Sci*. 70:41-60.

Curry, N., G. Ghézali, G.S. Kaminski Schierle, N. Rouach, and C.F. Kaminski. 2017. Correlative STED and Atomic Force Microscopy on Live Astrocytes Reveals Plasticity of Cytoskeletal Structure and Membrane Physical Properties during Polarized Migration. *Front. Cell. Neurosci.* 11:104.

Daigle, N., J. Beaudouin, L. Hartnell, G. Imreh, E. Hallberg, J. Lippincott-Schwartz, and J. Ellenberg. 2001. Nuclear pore complexes form immobile networks and have a very low turnover in live mammalian cells. *J Cell Biol*. 154:71-84.

Day, C.A., L.J. Kraft, M. Kang, and A.K. Kenworthy. 2012. Analysis of protein and lipid dynamics using confocal fluorescence recovery after photobleaching (FRAP). *Curr Protoc Cytom*. Chapter 2:Unit2 19.

De Bruin, A., E. Muller, S. Wurm, R. Caldelari, M. Wyder, M.J. Wheelock, and M.M. Suter. 1999. Loss of invasiveness in squamous cell carcinoma cells overexpressing desmosomal cadherins. *Cell Adhes Commun*. 7:13-28.

Delva, E., J.M. Jennings, C.C. Calkins, M.D. Kottke, V. Faundez, and A.P. Kowalczyk. 2008. Pemphigus vulgaris IgG-induced desmoglein-3 endocytosis and desmosomal disassembly

are mediated by a clathrin- and dynamin-independent mechanism. *J Biol Chem*. 283:18303-18313.

Delva, E., D.K. Tucker, and A.P. Kowalczyk. 2009. The desmosome. *Cold Spring Harb Perspect Biol*. 1:a002543.

DeMay, B.S., N. Noda, A.S. Gladfelter, and R. Oldenbourg. 2011. Rapid and quantitative imaging of excitation polarized fluorescence reveals ordered septin dynamics in live yeast. *Biophysical journal*. 101:985-994.

Demirag, G.G., Y. Sullu, D. Gurgenyatagi, N.O. Okumus, and I. Yucel. 2011. Expression of plakophilins (PKP1, PKP2, and PKP3) in gastric cancers. *Diagn Pathol*. 6:1.

Demmerle, J., C. Innocent, A.J. North, G. Ball, M. Müller, E. Miron, A. Matsuda, I.M. Dobbie, Y. Markaki, and L. Schermelleh. 2017. Strategic and practical guidelines for successful structured illumination microscopy. *Nat. Protoc.* 12:988-1010.

Dempsey, G.T. 2013. A user's guide to localization-based super-resolution fluorescence imaging. *Methods Cell Biol.* 114:561-592.

Dempsey, G.T., J.C. Vaughan, K.H. Chen, M. Bates, and X. Zhuang. 2011. Evaluation of fluorophores for optimal performance in localization-based super-resolution imaging. *Nat. Methods*. 8:1027-1036.

den Haan, A.D., B.Y. Tan, M.N. Zikusoka, L.I. Llado, R. Jain, A. Daly, C. Tichnell, C. James, N. Amat-Alarcon, T. Abraham, S.D. Russell, D.A. Bluemke, H. Calkins, D. Dalal, and D.P. Judge. 2009. Comprehensive desmosome mutation analysis in north americans with arrhythmogenic right ventricular dysplasia/cardiomyopathy. *Circ Cardiovasc Genet*. 2:428-435.

Dertinger, T., R. Colyer, G. Iyer, S. Weiss, and J. Enderlein. 2009. Fast, background-free, 3D super-resolution optical fluctuation imaging (SOFI). *Proc. Natl. Acad. Sci. U. S. A.* 106:22287-22292.

Desai, B.V., R.M. Harmon, and K.J. Green. 2009. Desmosomes at a glance. *J Cell Sci*. 122:4401-4407.

Deschout, H., T. Lukes, A. Sharipov, D. Szlag, L. Feletti, W. Vandenberg, P. Dedecker, J. Hofkens, M. Leutenegger, T. Lasser, and A. Radenovic. 2016. Complementarity of PALM and SOFI for super-resolution live-cell imaging of focal adhesions. *Nat. Commun.* 7:13693.

Dieding, M., J.D. Debus, R. Kerkhoff, A. Gaertner-Rommel, V. Walhorn, H. Milting, and D. Anselmetti. 2017. Arrhythmogenic cardiomyopathy related DSG2 mutations affect desmosomal cadherin binding kinetics. *Sci Rep*. 7:13791.

Durisic, N., L.L. Cuervo, and M. Lakadamyali. 2014a. Quantitative super-resolution microscopy: pitfalls and strategies for image analysis. *Curr. Opin. Chem. Biol.* 20:22-28.

Durisic, N., L. Laparra-Cuervo, A. Sandoval-Álvarez, J.S. Borbely, and M. Lakadamyali. 2014b. Single-molecule evaluation of fluorescent protein photoactivation efficiency using an in vivo nanotemplate. *Nat. Methods*. 11:156-162.

Dusek, R.L., and L.D. Attardi. 2011. Desmosomes: new perpetrators in tumour suppression. *Nat Rev Cancer*. 11:317-323.

Erami, Z., D. Herrmann, S.C. Warren, M. Nobis, E.J. McGhee, M.C. Lucas, W. Leung, N. Reischmann, A. Mrowinska, J.P. Schwarz, S. Kadir, J.R.W. Conway, C. Vennin, S.A. Karim, A.D. Campbell, D. Gallego-Ortega, A. Magenau, K.J. Murphy, R.A. Ridgway, A.M. Law, S.N. Walters, S.T. Grey, D.R. Croucher, L. Zhang, H. Herzog, E.C.

Hardeman, P.W. Gunning, C.J. Ormandy, T.R.J. Evans, D. Strathdee, O.J. Sansom, J.P. Morton, K.I. Anderson, and P. Timpson. 2016. Intravital FRAP Imaging using an E-cadherin-GFP Mouse Reveals Disease- and Drug-Dependent Dynamic Regulation of Cell-Cell Junctions in Live Tissue. *Cell Rep*. 14:152-167.

Farquhar, M.G., and G.E. Palade. 1963. Junctional complexes in various epithelia. *J Cell Biol*. 17:375-412.

Feller, L., R. Ballyram, R.A. Khammissa, M. Altini, and J. Lemmer. 2017. Immunopathogenic Oral Diseases: An Overview Focusing on Pemphigus Vulgaris and Mucous Membrane Pemphigoid. *Oral Health Prev Dent*. 15:177-182.

Fink, A., N. Sal-Man, D. Gerber, and Y. Shai. 2012. Transmembrane domains interactions within the membrane milieu: principles, advances and challenges. *Biochim Biophys Acta*. 1818:974-983.

Fölling, J., M. Bossi, H. Bock, R. Medda, C.A. Wurm, B. Hein, S. Jakobs, C. Eggeling, and S.W. Hell. 2008. Fluorescence nanoscopy by ground-state depletion and single-molecule return. *Nat. Methods*. 5:943-945.

Foote, H.P., K.D. Sumigray, and T. Lechler. 2013. FRAP analysis reveals stabilization of adhesion structures in the epidermis compared to cultured keratinocytes. *PLoS One*. 8:e71491.

Furukawa, C., Y. Daigo, N. Ishikawa, T. Kato, T. Ito, E. Tsuchiya, S. Sone, and Y. Nakamura. 2005. Plakophilin 3 oncogene as prognostic marker and therapeutic target for lung cancer. *Cancer Res*. 65:7102-7110.

Galdeen, S.A., and A.J. North. 2011. Live Cell Fluorescence Microscopy Techniques. *In* Methods in Molecular Biology. 205-222.

Garcia, M.A., W.J. Nelson, and N. Chavez. 2018. Cell-Cell Junctions Organize Structural and Signaling Networks. *Cold Spring Harb Perspect Biol*. 10.

Garrod, D. 2010. Desmosomes in vivo. *Dermatol Res Pract*. 2010:212439.

Garrod, D., and M. Chidgey. 2008. Desmosome structure, composition and function. *Biochim Biophys Acta*. 1778:572-587.

Garrod, D., and T.E. Kimura. 2008. Hyper-adhesion: a new concept in cell-cell adhesion. *Biochem Soc Trans*. 36:195-201.

Garrod, D.R. 2013. The assay that defines desmosome hyper-adhesion. *J Invest Dermatol*. 133:576-577.

Garrod, D.R., M.Y. Berika, W.F. Bardsley, D. Holmes, and L. Tabernero. 2005. Hyper-adhesion in desmosomes: its regulation in wound healing and possible relationship to cadherin crystal structure. *J Cell Sci*. 118:5743-5754.

Gehne, N., A. Lamik, M. Lehmann, R.F. Haseloff, A.V. Andjelkovic, and I.E. Blasig. 2017. Cross-over endocytosis of claudins is mediated by interactions via their extracellular loops. *PLoS One*. 12:e0182106.

Getsios, S., A.C. Huen, and K.J. Green. 2004. Working out the strength and flexibility of desmosomes. *Nat Rev Mol Cell Biol*. 5:271-281.

Gloushankova, N.A., T. Wakatsuki, R.B. Troyanovsky, E. Elson, and S.M. Troyanovsky. 2003. Continual assembly of desmosomes within stable intercellular contacts of epithelial A-431 cells. *Cell Tissue Res*. 314:399-410.

Godin, A.G., B. Lounis, and L. Cognet. 2014. Super-resolution microscopy approaches for live cell imaging. *Biophys. J.* 107:1777-1784.

Godsel, L.M., S.N. Hsieh, E.V. Amargo, A.E. Bass, L.T. Pascoe-McGillicuddy, A.C. Huen, M.E. Thorne, C.A. Gaudry, J.K. Park, K. Myung, R.D. Goldman, T.L. Chew, and K.J. Green. 2005. Desmoplakin assembly dynamics in four dimensions: multiple phases differentially regulated by intermediate filaments and actin. *J Cell Biol*. 171:1045-1059.

Goodenough, D.A., and D.L. Paul. 2009. Gap Junctions. *Cold Spring Harb. Perspect. Biol.* 1.

Gorbsky, G., and M.S. Steinberg. 1981. Isolation of the intercellular glycoproteins of desmosomes. *J Cell Biol*. 90:243-248.

Green, K.J., S. Getsios, S. Troyanovsky, and L.M. Godsel. 2010. Intercellular junction assembly, dynamics, and homeostasis. *Cold Spring Harb Perspect Biol*. 2:a000125.

Green, K.J., and C.L. Simpson. 2007. Desmosomes: new perspectives on a classic. *J Invest Dermatol*. 127:2499-2515.

Griffis, E.R., S. Xu, and M.A. Powers. 2003. Nup98 localizes to both nuclear and cytoplasmic sides of the nuclear pore and binds to two distinct nucleoporin subcomplexes. *Mol Biol Cell*. 14:600-610.

Grum, V.L., D. Li, R.I. MacDonald, and A. Mondragon. 1999. Structures of two repeats of spectrin suggest models of flexibility. *Cell*. 98:523-535.

Gumbiner, B.M. 1996. Cell adhesion: the molecular basis of tissue architecture and morphogenesis. *Cell*. 84:345-357.

Günzel, D., and M. Fromm. 2012. Claudins and Other Tight Junction Proteins. *In* Comprehensive Physiology.

Gustafsson, M.G. 2000. Surpassing the lateral resolution limit by a factor of two using structured illumination microscopy. *J. Microsc.* 198:82-87.

Gustafsson, M.G.L. 2005. Nonlinear structured-illumination microscopy: wide-field fluorescence imaging with theoretically unlimited resolution. *Proc. Natl. Acad. Sci. U. S. A.* 102:13081-13086.

Gustafsson, M.G.L., L. Shao, P.M. Carlton, C.J.R. Wang, I.N. Golubovskaya, W.Z. Cande, D.A. Agard, and J.W. Sedat. 2008. Three-dimensional resolution doubling in wide-field fluorescence microscopy by structured illumination. *Biophys. J.* 94:4957-4970.

Hakimelahi, S., H.R. Parker, A.J. Gilchrist, M. Barry, Z. Li, R.C. Bleackley, and M. Pasdar. 2000. Plakoglobin regulates the expression of the anti-apoptotic protein BCL-2. *J Biol Chem*. 275:10905-10911.

Harke, B., P. Bianchini, G. Vicidomini, S. Galiani, and A. Diaspro. 2013. Stimulated Emission Depletion (STED) Microscopy. *In* Encyclopedia of Biophysics. 2470-2475.

Harke, B., J. Keller, C.K. Ullal, V. Westphal, A. Schönle, and S.W. Hell. 2008. Resolution scaling in STED microscopy. *Opt. Express*. 16:4154-4162.

Harmon, R.M., and K.J. Green. 2013. Structural and functional diversity of desmosomes. *Cell Commun Adhes*. 20:171-187.

Harrison, O.J., J. Brasch, G. Lasso, P.S. Katsamba, G. Ahlsen, B. Honig, and L. Shapiro. 2016. Structural basis of adhesive binding by desmocollins and desmogleins. *Proc Natl Acad Sci U S A.* 113:7160-7165.

Hatzfeld, M., C. Haffner, K. Schulze, and U. Vinzens. 2000. The function of plakophilin 1 in desmosome assembly and actin filament organization. *J Cell Biol*. 149:209-222.

Haussinger, D., T. Ahrens, T. Aberle, J. Engel, J. Stetefeld, and S. Grzesiek. 2004. Proteolytic E-cadherin activation followed by solution NMR and X-ray crystallography. *EMBO J*. 23:1699-1708.

He, W., P. Cowin, and D.L. Stokes. 2003. Untangling desmosomal knots with electron tomography. *Science*. 302:109-113.

Heilemann, M., S. van de Linde, M. Schuttpelz, R. Kasper, B. Seefeldt, A. Mukherjee, P. Tinnefeld, and M. Sauer. 2008. Subdiffraction-resolution fluorescence imaging with conventional fluorescent probes. *Angew Chem Int Ed Engl*. 47:6172-6176.

Hein, B., K.I. Willig, C.A. Wurm, V. Westphal, S. Jakobs, and S.W. Hell. 2010. Stimulated emission depletion nanoscopy of living cells using SNAP-tag fusion proteins. *Biophys. J.* 98:158-163.

Heintzmann, R. 2003. Saturated patterned excitation microscopy with two-dimensional excitation patterns. *Micron*. 34:283-291.

Heintzmann, R., T.M. Jovin, and C. Cremer. 2002. Saturated patterned excitation microscopy--a concept for optical resolution improvement. *J. Opt. Soc. Am. A Opt. Image Sci. Vis.* 19:1599-1609.

Hell, S.W. 2009. Microscopy and its focal switch. *Nat. Methods*. 6:24-32.

Hell, S.W., and J. Wichmann. 1994. Breaking the diffraction resolution limit by stimulated emission: stimulated-emission-depletion fluorescence microscopy. *Opt. Lett.* 19:780-782.

Henriques, R., C. Griffiths, E. Hesper Rego, and M.M. Mhlanga. 2011. PALM and STORM: unlocking live-cell super-resolution. *Biopolymers*. 95:322-331.

Heupel, W.M., D. Zillikens, D. Drenckhahn, and J. Waschke. 2008. Pemphigus vulgaris IgG directly inhibit desmoglein 3-mediated transinteraction. *J Immunol*. 181:1825-1834.

Hirano, Y., A. Matsuda, and Y. Hiraoka. 2015. Recent advancements in structured-illumination microscopy toward live-cell imaging. *Microscopy*. 64:237-249.

Hobbs, R.P., and K.J. Green. 2012. Desmoplakin regulates desmosome hyperadhesion. *J Invest Dermatol*. 132:482-485.

Holthofer, B., R. Windoffer, S. Troyanovsky, and R.E. Leube. 2007. Structure and function of desmosomes. *Int Rev Cytol*. 264:65-163.

Homberg, M., and T.M. Magin. 2014. Beyond expectations: novel insights into epidermal keratin function and regulation. *Int Rev Cell Mol Biol*. 311:265-306.

Huang, B., W. Wang, M. Bates, and X. Zhuang. 2008. Three-Dimensional Super-Resolution Imaging by Stochastic Optical Reconstruction Microscopy. *Science*. 319:810-813.

Hudson, T.Y., L. Fontao, L.M. Godsel, H.-J. Choi, A.C. Huen, L. Borradori, W.I. Weis, and K.J. Green. 2004. In Vitro Methods for Investigating Desmoplakin–Intermediate Filament Interactions and Their Role in Adhesive Strength. *In* Methods in Cell Biology. Vol. 78. Academic Press. 757-786.

Indra, I., S. Hong, R. Troyanovsky, B. Kormos, and S. Troyanovsky. 2013. The adherens junction: a mosaic of cadherin and nectin clusters bundled by actin filaments. *J. Invest. Dermatol.* 133:2546-2554.

Inoue, S., O. Shimomura, M. Goda, M. Shribak, and P.T. Tran. 2002. Fluorescence polarization of green fluorescence protein. *Proc Natl Acad Sci U S A*. 99:4272-4277.

Irobalieva, R.N., B. Martins, and O. Medalia. 2016. Cellular structural biology as revealed by cryo-electron tomography. *J Cell Sci*. 129:469-476.

Ishida-Yamamoto, A., M. Kishibe, and M. Honma. 2017. Desmosomes and corneodesmosomes and their relevance to genetic skin diseases. *G Ital Dermatol Venereol*. 152:148-157.

Ivanov, A.I., and N.G. Naydenov. 2013. Dynamics and regulation of epithelial adherens junctions: recent discoveries and controversies. *Int. Rev. Cell Mol. Biol.* 303:27-99.

Johnson, E., and R. Kaufmann. 2017. Correlative In-Resin Super-Resolution Fluorescence and Electron Microscopy of Cultured Cells. *In* Methods in Molecular Biology. 163-177.

Johnson, J.L., N.A. Najor, and K.J. Green. 2014a. Desmosomes: regulators of cellular signaling and adhesion in epidermal health and disease. *Cold Spring Harb Perspect Med*. 4:a015297.

Johnson, J.L., N.A. Najor, and K.J. Green. 2014b. Desmosomes: regulators of cellular signaling and adhesion in epidermal health and disease. *Cold Spring Harb. Perspect. Med.* 4:a015297.

Jones, S.A., S.-H. Shim, J. He, and X. Zhuang. 2011. Fast, three-dimensional super-resolution imaging of live cells. *Nat. Methods*. 8:499-508.

Jungmann, R., C. Steinhauer, M. Scheible, A. Kuzyk, P. Tinnefeld, and F.C. Simmel. 2010. Single-molecule kinetics and super-resolution microscopy by fluorescence imaging of transient binding on DNA origami. *Nano Lett.* 10:4756-4761.

Kampmann, M., C.E. Atkinson, A.L. Mattheyses, and S.M. Simon. 2011. Mapping the orientation of nuclear pore proteins in living cells with polarized fluorescence microscopy. *Nat Struct Mol Biol*. 18:643-649.

Kanchanawong, P., G. Shtengel, A.M. Pasapera, E.B. Ramko, M.W. Davidson, H.F. Hess, and C.M. Waterman. 2010a. Nanoscale architecture of integrin-based cell adhesions. *Nature*. 468:580-584.

Kanchanawong, P., G. Shtengel, A.M. Pasapera, E.B. Ramko, M.W. Davidson, H.F. Hess, and C.M. Waterman. 2010b. Nanoscale architecture of integrin-based cell adhesions. *Nature*. 468:580-584.

Kant, S., B. Holthofer, T.M. Magin, C.A. Krusche, and R.E. Leube. 2015a. Desmoglein 2-Dependent Arrhythmogenic Cardiomyopathy Is Caused by a Loss of Adhesive Function. *Circ Cardiovasc Genet*. 8:553-563.

Kant, S., B. Holthöfer, T.M. Magin, C.A. Krusche, and R.E. Leube. 2015b. Desmoglein 2-Dependent Arrhythmogenic Cardiomyopathy Is Caused by a Loss of Adhesive Function. *Circ. Cardiovasc. Genet.* 8:553-563.

Kaufmann, R., J. Piontek, F. Grull, M. Kirchgessner, J. Rossa, H. Wolburg, I.E. Blasig, and C. Cremer. 2012a. Visualization and quantitative analysis of reconstituted tight junctions using localization microscopy. *PLoS One*. 7:e31128.

Kaufmann, R., J. Piontek, F. Grüll, M. Kirchgessner, J. Rossa, H. Wolburg, I.E. Blasig, and C. Cremer. 2012b. Visualization and quantitative analysis of reconstituted tight junctions using localization microscopy. *PLoS One*. 7:e31128.

Keil, R., K. Rietscher, and M. Hatzfeld. 2016. Antagonistic Regulation of Intercellular Cohesion by Plakophilins 1 and 3. *J Invest Dermatol*. 136:2022-2029.

Kelly, D.E. 1966. Fine structure of desmosomes. , hemidesmosomes, and an adepidermal globular layer in developing newt epidermis. *J Cell Biol*. 28:51-72.

Kemperman, M.H., L.H. Hoefsloot, and C.W. R. 2002. Hearing loss and connexin 26. *JRSM Short Rep.* 95:171-177.

Kierszenbaum, F., J. Dandliker, and W.B. Dandliker. 1969. Investigation of the antigen-antibody reaction by fluorescence polarization. Measurement of the effect of the fluorescent label upon the bovine serum albumin (BSA) anti-bsa equilibrium. *Immunochemistry*. 6:125-137.

Kim, S.A., C.Y. Tai, L.P. Mok, E.A. Mosser, and E.M. Schuman. 2011. Calcium-dependent dynamics of cadherin interactions at cell-cell junctions. *Proc Natl Acad Sci U S A*. 108:9857-9862.

Kim, S.Y., Y. Arai, T. Tani, H. Takatsuka, Y. Saito, T. Kawashima, S. Kawakami, A. Miyawaki, and T. Nagai. 2017. Simultaneous imaging of multiple cellular events using high-accuracy fluorescence polarization microscopy. *Microscopy (Oxf)*. 66:110-119.

Kimura, T.E., A.J. Merritt, and D.R. Garrod. 2007. Calcium-independent desmosomes of keratinocytes are hyper-adhesive. *J Invest Dermatol*. 127:775-781.

Kimura, T.E., A.J. Merritt, F.R. Lock, J.J. Eckert, T.P. Fleming, and D.R. Garrod. 2012. Desmosomal adhesiveness is developmentally regulated in the mouse embryo and modulated during trophectoderm migration. *Dev Biol*. 369:286-297.

Kitajima, Y. 2013. New insights into desmosome regulation and pemphigus blistering as a desmosome-remodeling disease. *Kaohsiung J Med Sci*. 29:1-13.

Kitajima, Y. 2014. 150(th) anniversary series: Desmosomes and autoimmune disease, perspective of dynamic desmosome remodeling and its impairments in pemphigus. *Cell Commun Adhes*. 21:269-280.

Klar, T.A., S. Jakobs, M. Dyba, A. Egner, and S.W. Hell. 2000. Fluorescence microscopy with diffraction resolution barrier broken by stimulated emission. *Proc. Natl. Acad. Sci. U. S. A.* 97:8206-8210.

Koch, P.J., M.J. Walsh, M. Schmelz, M.D. Goldschmidt, R. Zimbelmann, and W.W. Franke. 1990. Identification of desmoglein, a constitutive desmosomal glycoprotein, as a member of the cadherin family of cell adhesion molecules. *Eur J Cell Biol*. 53:1-12.

Kouklis, P.D., E. Hutton, and E. Fuchs. 1994. Making a connection: direct binding between keratin intermediate filaments and desmosomal proteins. *J Cell Biol*. 127:1049-1060.

Koulu, L., A. Kusumi, M.S. Steinberg, V. Klaus-Kovtun, and J.R. Stanley. 1984. Human autoantibodies against a desmosomal core protein in pemphigus foliaceus. *J Exp Med*. 160:1509-1518.

Koval, M., S.A. Molina, and B. Schlingmann. 2016. Use of Super-resolution Immunofluorescence Microscopy to Analyze Tight Junction Protein Interactions in situ. *Microsc. Microanal.* 22:1014-1015.

Kowalczyk, A.P., E.A. Bornslaeger, J.E. Borgwardt, H.L. Palka, A.S. Dhaliwal, C.M. Corcoran, M.F. Denning, and K.J. Green. 1997. The amino-terminal domain of desmoplakin binds to plakoglobin and clusters desmosomal cadherin-plakoglobin complexes. *J Cell Biol*. 139:773-784.

Kowalczyk, A.P., and K.J. Green. 2013. Structure, function, and regulation of desmosomes. *Prog Mol Biol Transl Sci*. 116:95-118.

Kowalczyk, A.P., H.L. Palka, H.H. Luu, L.A. Nilles, J.E. Anderson, M.J. Wheelock, and K.J. Green. 1994. Posttranslational regulation of plakoglobin expression. Influence of the desmosomal cadherins on plakoglobin metabolic stability. *J Biol Chem*. 269:31214-31223.

Kress, A., P. Ferrand, H. Rigneault, T. Trombik, H.T. He, D. Marguet, and S. Brasselet. 2011. Probing orientational behavior of MHC class I protein and lipid probes in cell membranes by fluorescence polarization-resolved imaging. *Biophysical journal*. 101:468-476.

Kroger, C., F. Loschke, N. Schwarz, R. Windoffer, R.E. Leube, and T.M. Magin. 2013. Keratins control intercellular adhesion involving PKC-alpha-mediated desmoplakin phosphorylation. *J Cell Biol*. 201:681-692.

Kurzen, H., I. Munzing, and W. Hartschuh. 2003. Expression of desmosomal proteins in squamous cell carcinomas of the skin. *J Cutan Pathol*. 30:621-630.

Lambert, T.J., and J.C. Waters. 2017. Navigating challenges in the application of superresolution microscopy. *J. Cell Biol.* 216:53-63.

Lee, C.W., E.A. Vitriol, S. Shim, A.L. Wise, R.P. Velayutham, and J.Q. Zheng. 2013. Dynamic localization of G-actin during membrane protrusion in neuronal motility. *Curr. Biol.* 23:1046-1056.

Lemmer, P., M. Gunkel, D. Baddeley, R. Kaufmann, A. Urich, Y. Weiland, J. Reymann, P. Müller, M. Hausmann, and C. Cremer. 2008. SPDM: light microscopy with single-molecule resolution at the nanoscale. *Appl. Phys. B*. 93:1-12.

Lewis, J.D., A.L. Caldara, S.E. Zimmer, A. Seybold, N.L. Strong, S.N. Stahley, A.S. Frangakis, I. Levental, J.K. Wahl, A.L. Mattheyses, T. Sasaki, K. Nakabayashi, K. Hata, Y. Matsubara, A. Ishida-Yamamoto, M. Amagai, A. Kubo, and A.P. Kowalczyk. 2018. The Desmosome is a Mesoscale Lipid Raft-Like Membrane Domain. *bioRxiv*:401455.

Li, D., L. Shao, B.-C. Chen, X. Zhang, M. Zhang, B. Moses, D.E. Milkie, J.R. Beach, J.A. Hammer, 3rd, M. Pasham, T. Kirchhausen, M.A. Baird, M.W. Davidson, P. Xu, and E. Betzig. 2015. ADVANCED IMAGING. Extended-resolution structured illumination imaging of endocytic and cytoskeletal dynamics. *Science*. 349:aab3500.

Li, L., K. Chapman, X. Hu, A. Wong, and M. Pasdar. 2007. Modulation of the oncogenic potential of beta-catenin by the subcellular distribution of plakoglobin. *Mol Carcinog*. 46:824-838.

Lippincott-Schwartz, J., E. Snapp, and A. Kenworthy. 2001. Studying protein dynamics in living cells. *Nat Rev Mol Cell Biol*. 2:444-456.

Liu, W., F. Edin, H. Blom, P. Magnusson, A. Schrott-Fischer, R. Glueckert, P.A. Santi, H. Li, G. Laurell, and H. Rask-Andersen. 2016. Super-resolution structured illumination fluorescence microscopy of the lateral wall of the cochlea: the Connexin26/30 proteins are separately expressed in man. *Cell Tissue Res.* 365:13-27.

Liu, W., H. Li, F. Edin, J. Brännström, R. Glueckert, A. Schrott-Fischer, M. Molnar, D. Pacholsky, K. Pfaller, and H. Rask-Andersen. 2017. Molecular composition and distribution of gap junctions in the sensory epithelium of the human cochlea—a super-resolution structured illumination microscopy (SR-SIM) study. *Ups. J. Med. Sci.*:1-11.

Loschberger, A., C. Franke, G. Krohne, S. van de Linde, and M. Sauer. 2014. Correlative super-resolution fluorescence and electron microscopy of the nuclear pore complex with molecular resolution. *J Cell Sci*. 127:4351-4355.

Loschberger, A., S. van de Linde, M.C. Dabauvalle, B. Rieger, M. Heilemann, G. Krohne, and M. Sauer. 2012. Super-resolution imaging visualizes the eightfold symmetry of gp210 proteins around the nuclear pore complex and resolves the central channel with nanometer resolution. *J Cell Sci*. 125:570-575.

Loschke, F., M. Homberg, and T.M. Magin. 2016. Keratin Isotypes Control Desmosome Stability and Dynamics through PKCalpha. *J Invest Dermatol*. 136:202-213.

Lowndes, M., S. Rakshit, O. Shafraz, N. Borghi, R.M. Harmon, K.J. Green, S. Sivasankar, and W.J. Nelson. 2014. Different roles of cadherins in the assembly and structural integrity of the desmosome complex. *J Cell Sci*. 127:2339-2350.

Maeda, S., S. Nakagawa, M. Suga, E. Yamashita, A. Oshima, Y. Fujiyoshi, and T. Tsukihara. 2009. Structure of the connexin 26 gap junction channel at 3.5 Å resolution. *Nature*. 458:597-602.

Malkusch, S., W. Muranyi, B. Müller, H.-G. Kräusslich, and M. Heilemann. 2013. Single-molecule coordinate-based analysis of the morphology of HIV-1 assembly sites with near-molecular spatial resolution. *Histochem. Cell Biol.* 139:173-179.

Marziano, N.K., S.O. Casalotti, A.E. Portelli, D.L. Becker, and A. Forge. 2003. Mutations in the gene for connexin 26 (GJB2) that cause hearing loss have a dominant negative effect on connexin 30. *Hum. Mol. Genet.* 12:805-812.

Mattey, D.L., and D.R. Garrod. 1986. Splitting and internalization of the desmosomes of cultured kidney epithelial cells by reduction in calcium concentration. *J Cell Sci*. 85:113-124.

Mattheyses, A.L., M. Kampmann, C.E. Atkinson, and S.M. Simon. 2010. Fluorescence anisotropy reveals order and disorder of protein domains in the nuclear pore complex. *Biophysical journal*. 99:1706-1717.

McAleer, M.A., E. Pohler, F.J. Smith, N.J. Wilson, C. Cole, S. MacGowan, J.L. Koetsier, L.M. Godsel, R.M. Harmon, R. Gruber, D. Crumrine, P.M. Elias, M. McDermott, K. Butler, A. Broderick, O. Sarig, E. Sprecher, K.J. Green, W.H. McLean, and A.D. Irvine. 2015. Severe dermatitis, multiple allergies, and metabolic wasting syndrome caused by a novel

mutation in the N-terminal plakin domain of desmoplakin. *J Allergy Clin Immunol*. 136:1268-1276.

McHarg, S., G. Hopkins, L. Lim, and D. Garrod. 2014. Down-regulation of desmosomes in cultured cells: the roles of PKC, microtubules and lysosomal/proteasomal degradation. *PLoS One*. 9:e108570.

McKoy, G., N. Protonotarios, A. Crosby, A. Tsatsopoulou, A. Anastasakis, A. Coonar, M. Norman, C. Baboonian, S. Jeffery, and W.J. McKenna. 2000. Identification of a deletion in plakoglobin in arrhythmogenic right ventricular cardiomyopathy with palmoplantar keratoderma and woolly hair (Naxos disease). *Lancet*. 355:2119-2124.

McQuilken, M., S.B. Mehta, A. Verma, G. Harris, R. Oldenbourg, and A.S. Gladfelter. 2015. Polarized Fluorescence Microscopy to Study Cytoskeleton Assembly and Organization in Live Cells. *Curr Protoc Cell Biol*. 67:4 29 21-13.

Mehta, S.B., M. McQuilken, P.J. La Riviere, P. Occhipinti, A. Verma, R. Oldenbourg, A.S. Gladfelter, and T. Tani. 2016. Dissection of molecular assembly dynamics by tracking orientation and position of single molecules in live cells. *Proc Natl Acad Sci U S A*. 113:E6352-E6361.

Merritt, A.J., M.Y. Berika, W. Zhai, S.E. Kirk, B. Ji, M.J. Hardman, and D.R. Garrod. 2002. Suprabasal desmoglein 3 expression in the epidermis of transgenic mice results in hyperproliferation and abnormal differentiation. *Mol Cell Biol*. 22:5846-5858.

Moerner, W.E., M. Orrit, U.P. Wild, and T. Basché. 2008. Single-Molecule Optical Detection, Imaging and Spectroscopy. John Wiley & Sons. 264 pp.

Moh, M.C., and S. Shen. 2009. The roles of cell adhesion molecules in tumor suppression and cell migration: a new paradox. *Cell Adh Migr*. 3:334-336.

Moore, D.T., B.W. Berger, and W.F. DeGrado. 2008. Protein-protein interactions in the membrane: sequence, structural, and biological motifs. *Structure*. 16:991-1001.

Mouritsen, O.G., and K. Jorgensen. 1994. Dynamical order and disorder in lipid bilayers. *Chem Phys Lipids*. 73:3-25.

Nahidiazar, L., M. Kreft, B. van den Broek, P. Secades, E.M.M. Manders, A. Sonnenberg, and K. Jalink. 2015. The molecular architecture of hemidesmosomes, as revealed with super-resolution microscopy. *J. Cell Sci.* 128:3714-3719.

Najor, N.A. 2018. Desmosomes in Human Disease. *Annu Rev Pathol*. 13:51-70.

Nanes, B.A., C. Chiasson-MacKenzie, A.M. Lowery, N. Ishiyama, V. Faundez, M. Ikura, P.A. Vincent, and A.P. Kowalczyk. 2012. p120-catenin binding masks an endocytic signal conserved in classical cadherins. *J Cell Biol*. 199:365-380.

Nei, H., T. Saito, H. Tobioka, E. Itoh, M. Mori, and R. Kudo. 1996. Expression of component desmosomal proteins in uterine endometrial carcinoma and their relation to cellular differentiation. *Cancer*. 78:461-470.

Neil, M.A.A., R. Juškaitis, and T. Wilson. 1997. Method of obtaining optical sectioning by using structured light in a conventional microscope. *Opt. Lett., OL*. 22:1905-1907.

Nekrasova, O., and K.J. Green. 2013. Desmosome assembly and dynamics. *Trends Cell Biol*. 23:537-546.

Nie, Z., A. Merritt, M. Rouhi-Parkouhi, L. Tabernero, and D. Garrod. 2011. Membrane-impermeable cross-linking provides evidence for homophilic, isoform-specific binding of desmosomal cadherins in epithelial cells. *J Biol Chem*. 286:2143-2154.

Niessen, C.M. 2007. Tight junctions/adherens junctions: basic structure and function. *J. Invest. Dermatol.* 127:2525-2532.

Norgett, E.E., S.J. Hatsell, L. Carvajal-Huerta, J.C. Cabezas, J. Common, P.E. Purkis, N. Whittock, I.M. Leigh, H.P. Stevens, and D.P. Kelsell. 2000. Recessive mutation in desmoplakin disrupts desmoplakin-intermediate filament interactions and causes dilated cardiomyopathy, woolly hair and keratoderma. *Hum Mol Genet*. 9:2761-2766.

North, A.J., W.G. Bardsley, J. Hyam, E.A. Bornslaeger, H.C. Cordingley, B. Trinnaman, M. Hatzfeld, K.J. Green, A.I. Magee, and D.R. Garrod. 1999a. Molecular map of the desmosomal plaque. *J. Cell Sci.* 112 (Pt 23):4325-4336.

North, A.J., W.G. Bardsley, J. Hyam, E.A. Bornslaeger, H.C. Cordingley, B. Trinnaman, M. Hatzfeld, K.J. Green, A.I. Magee, and D.R. Garrod. 1999b. Molecular map of the desmosomal plaque. *J Cell Sci*. 112 (Pt 23):4325-4336.

O'Keefe, E.J., H.P. Erickson, and V. Bennett. 1989. Desmoplakin I and desmoplakin II. Purification and characterization. *J Biol Chem*. 264:8310-8318.

Odland, G.F. 1958. The fine structure of the interrelationship of cells in the human epidermis. *J. Biophys. Biochem. Cytol.* 4:529-538.

Ohmachi, M., Y. Komori, A.H. Iwane, F. Fujii, T. Jin, and T. Yanagida. 2012. Fluorescence microscopy for simultaneous observation of 3D orientation and movement and its application to quantum rod-tagged myosin V. *Proc Natl Acad Sci U S A*. 109:5294-5298.

Oldenbourg, R. 2013. Polarized light microscopy: principles and practice. *Cold Spring Harb Protoc*. 2013.

Olshausen, P.v., H.J.D. Soufo, K. Wicker, R. Heintzmann, P.L. Graumann, and A. Rohrbach. 2013. Superresolution Imaging of Dynamic MreB Filaments in B. subtilis—A Multiple-Motor-Driven Transport? *Biophys. J.* 105:1171-1181.

Ortolano, S., G. Di Pasquale, G. Crispino, F. Anselmi, F. Mammano, and J.A. Chiorini. 2008. Coordinated control of connexin 26 and connexin 30 at the regulatory and functional level in the inner ear. *Proc. Natl. Acad. Sci. U. S. A.* 105:18776-18781.

Overduin, M., T.S. Harvey, S. Bagby, K.I. Tong, P. Yau, M. Takeichi, and M. Ikura. 1995. Solution structure of the epithelial cadherin domain responsible for selective cell adhesion. *Science*. 267:386-389.

Owen, G.R., D. Acehan, K.D. Derr, W.J. Rice, and D.L. Stokes. 2008. Cryoelectron tomography of isolated desmosomes. *Biochem Soc Trans*. 36:173-179.

Palka, H.L., and K.J. Green. 1997. Roles of plakoglobin end domains in desmosome assembly. *J Cell Sci*. 110 (Pt 19):2359-2371.

Parsons, J.T., A.R. Horwitz, and M.A. Schwartz. 2010. Cell adhesion: integrating cytoskeletal dynamics and cellular tension. *Nat Rev Mol Cell Biol*. 11:633-643.

Pástor, M.V.D. 2009. Direct Immunofluorescent Labeling of Cells. *In* Methods in Molecular Biology. 135-142.

Patel, S.D., C.P. Chen, F. Bahna, B. Honig, and L. Shapiro. 2003. Cadherin-mediated cell-cell adhesion: sticking together as a family. *Curr Opin Struct Biol*. 13:690-698.

Paul, M., T. Wichter, L. Fabritz, J. Waltenberger, E. Schulze-Bahr, and P. Kirchhof. 2012. Arrhythmogenic right ventricular cardiomyopathy: an update on pathophysiology, genetics, diagnosis, and risk stratification. *Herzschrittmacherther Elektrophysiol*. 23:186-195.

Penn, E.J., I.D. Burdett, C. Hobson, A.I. Magee, and D.A. Rees. 1987. Structure and assembly of desmosome junctions: biosynthesis and turnover of the major desmosome components of Madin-Darby canine kidney cells in low calcium medium. *J Cell Biol*. 105:2327-2334.

Perez-Moreno, M., C. Jamora, and E. Fuchs. 2003. Sticky business: orchestrating cellular signals at adherens junctions. *Cell*. 112:535-548.

Perkovic, M., M. Kunz, U. Endesfelder, S. Bunse, C. Wigge, Z. Yu, V.-V. Hodirnau, M.P. Scheffer, A. Seybert, S. Malkusch, E.M. Schuman, M. Heilemann, and A.S. Frangakis. 2014. Correlative light- and electron microscopy with chemical tags. *J. Struct. Biol.* 186:205-213.

Peters, S., M. Trummel, and W. Meyners. 2004. Prevalence of right ventricular dysplasia-cardiomyopathy in a non-referral hospital. *Int J Cardiol*. 97:499-501.

Pokutta, S., K. Herrenknecht, R. Kemler, and J. Engel. 1994. Conformational changes of the recombinant extracellular domain of E-cadherin upon calcium binding. *Eur J Biochem*. 223:1019-1026.

Porter, K.R. 1956. Observation on the Fine Structure of Animal Epidermis.

Rampazzo, A., M. Calore, J. van Hengel, and F. van Roy. 2014. Intercalated discs and arrhythmogenic cardiomyopathy. *Circ Cardiovasc Genet*. 7:930-940.

Ray, P.S., A. Arif, and P.L. Fox. 2007. Macromolecular complexes as depots for releasable regulatory proteins. *Trends Biochem Sci*. 32:158-164.

Rayleigh, L. 1879. LVI. Investigations in optics, with special reference to the spectroscope. *Philos. Mag.* 8:477-486.

Rayns, D.G., F.O. Simpson, and J.M. Ledingham. 1969. Ultrastructure of desmosomes in mammalian intercalated disc; appearances after lanthanum treatment. *J Cell Biol*. 42:322-326.

Resnik, N., K. Sepcic, A. Plemenitas, R. Windoffer, R. Leube, and P. Veranic. 2011. Desmosome assembly and cell-cell adhesion are membrane raft-dependent processes. *J Biol Chem*. 286:1499-1507.

Ribeiro, S.A., P. Vagnarelli, Y. Dong, T. Hori, B.F. McEwen, T. Fukagawa, C. Flors, and W.C. Earnshaw. 2010. A super-resolution map of the vertebrate kinetochore. *Proc Natl Acad Sci U S A*. 107:10484-10489.

Rickelt, S., and S. Pieperhoff. 2012. Mutations with pathogenic potential in proteins located in or at the composite junctions of the intercalated disk connecting mammalian cardiomyocytes: a reference thesaurus for arrhythmogenic cardiomyopathies and for Naxos and Carvajal diseases. *Cell Tissue Res*. 348:325-333.

Rieger-Christ, K.M., L. Ng, R.S. Hanley, O. Durrani, H. Ma, A.S. Yee, J.A. Libertino, and I.C. Summerhayes. 2005. Restoration of plakoglobin expression in bladder carcinoma cell lines suppresses cell migration and tumorigenic potential. *Br J Cancer*. 92:2153-2159.

Rittweger, E., K.Y. Han, S.E. Irvine, C. Eggeling, and S.W. Hell. 2009. STED microscopy reveals crystal colour centres with nanometric resolution. *Nat. Photonics*. 3:144-147.

Roberts, B.J., K.E. Johnson, K.P. McGuinn, J. Saowapa, R.A. Svoboda, M.G. Mahoney, K.R. Johnson, and J.K. Wahl, 3rd. 2014. Palmitoylation of plakophilin is required for desmosome assembly. *J Cell Sci*. 127:3782-3793.

Rocheleau, J.V., M. Edidin, and D.W. Piston. 2003. Intrasequence GFP in class I MHC molecules, a rigid probe for fluorescence anisotropy measurements of the membrane environment. *Biophysical journal*. 84:4078-4086.

Rosell, F.I., and S.G. Boxer. 2003. Polarized absorption spectra of green fluorescent protein single crystals: transition dipole moment directions. *Biochemistry*. 42:177-183.

Rothbauer, U., K. Zolghadr, S. Tillib, D. Nowak, L. Schermelleh, A. Gahl, N. Backmann, K. Conrath, S. Muyldermans, M.C. Cardoso, and H. Leonhardt. 2006. Targeting and tracing antigens in live cells with fluorescent nanobodies. *Nat. Methods*. 3:887-889.

Rotzer, V., E. Hartlieb, J. Winkler, E. Walter, A. Schlipp, M. Sardy, V. Spindler, and J. Waschke. 2016. Desmoglein 3-Dependent Signaling Regulates Keratinocyte Migration and Wound Healing. *J Invest Dermatol*. 136:301-310.

Rubsam, M., J.A. Broussard, S.A. Wickstrom, O. Nekrasova, K.J. Green, and C.M. Niessen. 2018. Adherens Junctions and Desmosomes Coordinate Mechanics and Signaling to Orchestrate Tissue Morphogenesis and Function: An Evolutionary Perspective. *Cold Spring Harb Perspect Biol*. 10.

Rübsam, M., J.A. Broussard, S.A. Wickström, O. Nekrasova, K.J. Green, and C.M. Niessen. 2017. Adherens Junctions and Desmosomes Coordinate Mechanics and Signaling to Orchestrate Tissue Morphogenesis and Function: An Evolutionary Perspective. *Cold Spring Harb. Perspect. Biol.*

Rust, M.J., M. Bates, and X. Zhuang. 2006. Sub-diffraction-limit imaging by stochastic optical reconstruction microscopy (STORM). *Nat. Methods*. 3:793-795.

Saito, M., S.N. Stahley, C.Y. Caughman, X. Mao, D.K. Tucker, A.S. Payne, M. Amagai, and A.P. Kowalczyk. 2012. Signaling dependent and independent mechanisms in pemphigus vulgaris blister formation. *PLoS One*. 7:e50696.

Samuelov, L., O. Sarig, R.M. Harmon, D. Rapaport, A. Ishida-Yamamoto, O. Isakov, J.L. Koetsier, A. Gat, I. Goldberg, R. Bergman, R. Spiegel, O. Eytan, S. Geller, S. Peleg, N. Shomron, C.S.M. Goh, N.J. Wilson, F.J.D. Smith, E. Pohler, M.A. Simpson, W.H.I. McLean, A.D. Irvine, M. Horowitz, J.A. McGrath, K.J. Green, and E. Sprecher. 2013.

Desmoglein 1 deficiency results in severe dermatitis, multiple allergies and metabolic wasting. *Nat Genet*. 45:1244-1248.

Sarangi, N.K., I.I. P, K.G. Ayappa, S.S. Visweswariah, and J.K. Basu. 2016. Super-resolution Stimulated Emission Depletion-Fluorescence Correlation Spectroscopy Reveals Nanoscale Membrane Reorganization Induced by Pore-Forming Proteins. *Langmuir*. 32:9649-9657.

Schermelleh, L., P.M. Carlton, S. Haase, L. Shao, L. Winoto, P. Kner, B. Burke, M.C. Cardoso, D.A. Agard, M.G.L. Gustafsson, H. Leonhardt, and J.W. Sedat. 2008. Subdiffraction multicolor imaging of the nuclear periphery with 3D structured illumination microscopy. *Science*. 320:1332-1336.

Schermelleh, L., R. Heintzmann, and H. Leonhardt. 2010. A guide to super-resolution fluorescence microscopy. *J. Cell Biol.* 190:165-175.

Schiavon, M., A. Zorzi, C. Basso, A. Pelliccia, G. Thiene, and D. Corrado. 2011. Arrhythmogenic Cardiomyopathy and Sports-Related Sudden Death. *Cardiac Electrophysiology Clinics*. 3:323-331.

Schlingmann, B., C.E. Overgaard, S.A. Molina, K.S. Lynn, L.A. Mitchell, S. Dorsainvil White, A.L. Mattheyses, D.M. Guidot, C.T. Capaldo, and M. Koval. 2016. Regulation of claudin/zonula occludens-1 complexes by hetero-claudin interactions. *Nat. Commun.* 7:12276.

Schlipp, A., C. Schinner, V. Spindler, F. Vielmuth, K. Gehmlich, P. Syrris, W.J. McKenna, A. Dendorfer, E. Hartlieb, and J. Waschke. 2014. Desmoglein-2 interaction is crucial for cardiomyocyte cohesion and function. *Cardiovasc Res*. 104:245-257.

Seiffert, S., and W. Oppermann. 2005. Systematic evaluation of FRAP experiments performed in a confocal laser scanning microscope. *J Microsc*. 220:20-30.

Selby, C.C. 1955. AN ELECTRON MICROSCOPE STUDY OF THE EPIDERMIS OF MAMMALIAN SKIN IN THIN SECTIONS: I. DERMO-EPIDERMAL JUNCTION AND BASAL CELL LAYER. *J. Cell Biol.* 1:429-444.

Shafraz, O., M. Rubsam, S.N. Stahley, A.L. Caldara, A.P. Kowalczyk, C.M. Niessen, and S. Sivasankar. 2018. E-cadherin binds to desmoglein to facilitate desmosome assembly. *Elife*. 7.

Shao, L., P. Kner, E.H. Rego, and M.G.L. Gustafsson. 2011. Super-resolution 3D microscopy of live whole cells using structured illumination. *Nat. Methods*. 8:1044-1046.

Shapiro, L., A.M. Fannon, P.D. Kwong, A. Thompson, M.S. Lehmann, G. Grubel, J.F. Legrand, J. Als-Nielsen, D.R. Colman, and W.A. Hendrickson. 1995. Structural basis of cell-cell adhesion by cadherins. *Nature*. 374:327-337.

Sharonov, A., and R.M. Hochstrasser. 2006. Wide-field subdiffraction imaging by accumulated binding of diffusing probes. *Proc. Natl. Acad. Sci. U. S. A.* 103:18911-18916.

Shimizu, A., A. Ishiko, T. Ota, H. Saito, H. Oka, K. Tsunoda, M. Amagai, and T. Nishikawa. 2005. In vivo ultrastructural localization of the desmoglein 3 adhesive interface to the desmosome mid-line. *J Invest Dermatol*. 124:984-989.

Shroff, H., C.G. Galbraith, J.A. Galbraith, and E. Betzig. 2008. Live-cell photoactivated localization microscopy of nanoscale adhesion dynamics. *Nat. Methods*. 5:417-423.

Shtengel, G., J.A. Galbraith, C.G. Galbraith, J. Lippincott-Schwartz, J.M. Gillette, S. Manley, R. Sougrat, C.M. Waterman, P. Kanchanawong, M.W. Davidson, R.D. Fetter, and H.F.

Hess. 2009. Interferometric fluorescent super-resolution microscopy resolves 3D cellular ultrastructure. *Proceedings of the National Academy of Sciences*. 106:3125-3130.

Siljamäki, E., L. Raiko, M. Toriseva, L. Nissinen, T. Näreoja, J. Peltonen, V.-M. Kähäri, and S. Peltonen. 2014. p38δ mitogen-activated protein kinase regulates the expression of tight junction protein ZO-1 in differentiating human epidermal keratinocytes. *Arch. Dermatol. Res.* 306:131-141.

Simcha, I., B. Geiger, S. Yehuda-Levenberg, D. Salomon, and A. Ben-Ze'ev. 1996. Suppression of tumorigenicity by plakoglobin: an augmenting effect of N-cadherin. *J Cell Biol*. 133:199-209.

Simons, K., and E. Ikonen. 1997. Functional rafts in cell membranes. *Nature*. 387:569-572.

Sirerol-Piquer, M.S., A. Cebrian-Silla, C. Alfaro-Cervello, U. Gomez-Pinedo, M. Soriano-Navarro, and J.M. Verdugo. 2012. GFP immunogold staining, from light to electron microscopy, in mammalian cells. *Micron*. 43:589-599.

Sivasankar, S. 2013. Tuning the kinetics of cadherin adhesion. *J Invest Dermatol*. 133:2318-2323.

Skerrow, C.J., and A.G. Matoltsy. 1974. Chemical characterization of isolated epidermal desmosomes. *J Cell Biol*. 63:524-530.

Sluysmans, S., E. Vasileva, D. Spadaro, J. Shah, F. Rouaud, and S. Citi. 2017. The role of apical cell-cell junctions and associated cytoskeleton in mechanotransduction. *Biol. Cell*. 109:139-161.

Sobolik-Delmaire, T., D. Katafiasz, and J.K. Wahl, 3rd. 2006. Carboxyl terminus of Plakophilin-1 recruits it to plasma membrane, whereas amino terminus recruits desmoplakin and promotes desmosome assembly. *J Biol Chem*. 281:16962-16970.

Sobolik-Delmaire, T., R. Reddy, A. Pashaj, B.J. Roberts, and J.K. Wahl, 3rd. 2010. Plakophilin-1 localizes to the nucleus and interacts with single-stranded DNA. *J Invest Dermatol*. 130:2638-2646.

Soeller, C., Y. Hou, I.D. Jayasinghe, D. Baddeley, and D. Crossman. 2017. Correlative Single-Molecule Localization Microscopy and Confocal Microscopy. *In* Methods in Molecular Biology. 205-217.

Sotomayor, M., and K. Schulten. 2008. The allosteric role of the Ca2+ switch in adhesion and elasticity of C-cadherin. *Biophysical journal*. 94:4621-4633.

Spindler, V., W.M. Heupel, A. Efthymiadis, E. Schmidt, R. Eming, C. Rankl, P. Hinterdorfer, T. Muller, D. Drenckhahn, and J. Waschke. 2009. Desmocollin 3-mediated binding is crucial for keratinocyte cohesion and is impaired in pemphigus. *J Biol Chem*. 284:30556-30564.

Spindler, V., and J. Waschke. 2018. Pemphigus-A Disease of Desmosome Dysfunction Caused by Multiple Mechanisms. *Front Immunol*. 9:136.

Sprague, B.L., and J.G. McNally. 2005. FRAP analysis of binding: proper and fitting. *Trends Cell Biol*. 15:84-91.

Sprenger, A., S. Weber, M. Zarai, R. Engelke, J.M. Nascimento, C. Gretzmeier, M. Hilpert, M. Boerries, C. Has, H. Busch, L. Bruckner-Tuderman, and J. Dengjel. 2013. Consistency of the proteome in primary human keratinocytes with respect to gender, age, and skin localization. *Mol Cell Proteomics*. 12:2509-2521.

Stahley, S.N., E.I. Bartle, C.E. Atkinson, A.P. Kowalczyk, and A.L. Mattheyses. 2016a. Molecular organization of the desmosome as revealed by direct stochastic optical reconstruction microscopy. *J. Cell Sci.* 129:2897-2904.

Stahley, S.N., and A.P. Kowalczyk. 2015. Desmosomes in acquired disease. *Cell Tissue Res*. 360:439-456.

Stahley, S.N., M. Saito, V. Faundez, M. Koval, A.L. Mattheyses, and A.P. Kowalczyk. 2014. Desmosome assembly and disassembly are membrane raft-dependent. *PLoS One*. 9:e87809.

Stahley, S.N., M.F. Warren, R.J. Feldman, A.L. Mattheyses, and A.P. Kowalczyk. 2016b. Super resolution microscopy reveals altered desmosome organization, endocytosis and desmosome splitting in pemphigus vulgaris epidermis. *J. Dermatol. Sci.* 84:e25.

Stahley, S.N., M.F. Warren, R.J. Feldman, R.A. Swerlick, A.L. Mattheyses, and A.P. Kowalczyk. 2015. Super-Resolution Microscopy Reveals Altered Desmosomal Protein Organization in Pemphigus Vulgaris Patient Tissue. *J Invest Dermatol*.

Stokes, D.L. 2007. Desmosomes from a structural perspective. *Curr Opin Cell Biol*. 19:565-571.

Sydor, A.M., K.J. Czymmek, E.M. Puchner, and V. Mennella. 2015. Super-Resolution Microscopy: From Single Molecules to Supramolecular Assemblies. *Trends Cell Biol.* 25:730-748.

Syed, S.E., B. Trinnaman, S. Martin, S. Major, J. Hutchinson, and A.I. Magee. 2002. Molecular interactions between desmosomal cadherins. *Biochem J*. 362:317-327.

Tam, J., G.A. Cordier, J.S. Borbely, A. Sandoval Alvarez, and M. Lakadamyali. 2014. Cross-talk-free multi-color STORM imaging using a single fluorophore. *PLoS One*. 9:e101772.

Tamarin, A., and L.M. Sreebny. 1963. An Analysis of Desmosome Shape, Size, and Orientation by the Use of Histometric and Densitometric Methods with Electron Microscopy. *J Cell Biol*. 18:125-134.

Tariq, H., J. Bella, T.A. Jowitt, D.F. Holmes, M. Rouhi, Z. Nie, C. Baldock, D. Garrod, and L. Tabernero. 2015. Cadherin flexibility provides a key difference between desmosomes and adherens junctions. *Proc Natl Acad Sci U S A*. 112:5395-5400.

Thomason, H.A., A. Scothern, S. McHarg, and D.R. Garrod. 2010. Desmosomes: adhesive strength and signalling in health and disease. *Biochem J*. 429:419-433.

Todorovic, V., J.L. Koetsier, L.M. Godsel, and K.J. Green. 2014. Plakophilin 3 mediates Rap1-dependent desmosome assembly and adherens junction maturation. *Mol Biol Cell*. 25:3749-3764.

Truong Quang, B.-A., M. Mani, O. Markova, T. Lecuit, and P.-F. Lenne. 2013. Principles of E-cadherin supramolecular organization in vivo. *Curr. Biol.* 23:2197-2207.

Tselepis, C., M. Chidgey, A. North, and D. Garrod. 1998. Desmosomal adhesion inhibits invasive behavior. *Proc Natl Acad Sci U S A*. 95:8064-8069.

Tsunoda, K., T. Ota, M. Aoki, T. Yamada, T. Nagai, T. Nakagawa, S. Koyasu, T. Nishikawa, and M. Amagai. 2003. Induction of pemphigus phenotype by a mouse monoclonal antibody against the amino-terminal adhesive interface of desmoglein 3. *J Immunol*. 170:2170-2178.

Tucker, D.K., S.N. Stahley, and A.P. Kowalczyk. 2014. Plakophilin-1 protects keratinocytes from pemphigus vulgaris IgG by forming calcium-independent desmosomes. *J Invest Dermatol*. 134:1033-1043.

Valades Cruz, C.A., H.A. Shaban, A. Kress, N. Bertaux, S. Monneret, M. Mavrakis, J. Savatier, and S. Brasselet. 2016. Quantitative nanoscale imaging of orientational order in biological filaments by polarized superresolution microscopy. *Proc Natl Acad Sci U S A*. 113:E820-828.

van Hoorn, H., R. Harkes, E.M. Spiesz, C. Storm, D. van Noort, B. Ladoux, and T. Schmidt. 2014. The nanoscale architecture of force-bearing focal adhesions. *Nano Lett*. 14:4257-4262.

Van Itallie, C.M., A.J. Tietgens, and J.M. Anderson. 2017. Visualizing the dynamic coupling of claudin strands to the actin cytoskeleton through ZO-1. *Mol. Biol. Cell*. 28:524-534.

Vicidomini, G., H. Ta, A. Honigmann, V. Mueller, M.P. Clausen, D. Waithe, S. Galiani, E. Sezgin, A. Diaspro, S.W. Hell, and C. Eggeling. 2015. STED-FLCS: An Advanced Tool to Reveal Spatiotemporal Heterogeneity of Molecular Membrane Dynamics. *Nano Lett.* 15:5912-5918.

Vielmuth, F., E. Hartlieb, D. Kugelmann, J. Waschke, and V. Spindler. 2015. Atomic force microscopy identifies regions of distinct desmoglein 3 adhesive properties on living keratinocytes. *Nanomedicine*. 11:511-520.

Vielmuth, F., M.T. Wanuske, M.Y. Radeva, M. Hiermaier, D. Kugelmann, E. Walter, F. Buechau, T.M. Magin, J. Waschke, and V. Spindler. 2018. Keratins Regulate the Adhesive Properties of Desmosomal Cadherins through Signaling. *J Invest Dermatol*. 138:121-131.

Vrabioiu, A.M., and T.J. Mitchison. 2006. Structural insights into yeast septin organization from polarized fluorescence microscopy. *Nature*. 443:466-469.

Wallis, S., S. Lloyd, I. Wise, G. Ireland, T.P. Fleming, and D. Garrod. 2000. The alpha isoform of protein kinase C is involved in signaling the response of desmosomes to wounding in cultured epithelial cells. *Mol Biol Cell*. 11:1077-1092.

Wang, F., S. Chen, H.B. Liu, C.A. Parent, and P.A. Coulombe. 2018. Keratin 6 regulates collective keratinocyte migration by altering cell-cell and cell-matrix adhesion. *J Cell Biol*. 217:4314-4330.

Weber, G. 1953. Rotational Brownian motion and polarization of the fluorescence of solutions. *Adv Protein Chem*. 8:415-459.

Weber, G., and S.R. Anderson. 1969. The effects of energy transfer and rotational diffusion upon the fluorescence polarization of macromolecules. *Biochemistry*. 8:361-371.

Weber, K., P.C. Rathke, and M. Osborn. 1978. Cytoplasmic microtubular images in glutaraldehyde-fixed tissue culture cells by electron microscopy and by immunofluorescence microscopy. *Proc. Natl. Acad. Sci. U. S. A.* 75:1820-1824.

Wegel, E., A. Göhler, B. Christoffer Lagerholm, A. Wainman, S. Uphoff, R. Kaufmann, and I.M. Dobbie. 2016. Imaging cellular structures in super-resolution with SIM, STED and Localisation Microscopy: A practical comparison. *Sci. Rep.* 6.

Whelan, D.R., and T.D. Bell. 2015. Correlative Synchrotron Fourier Transform Infrared Spectroscopy and Single Molecule Super Resolution Microscopy for the Detection of Composition and Ultrastructure Alterations in Single Cells. *ACS Chem Biol*. 10:2874-2883.

Whittock, N.V., F.J. Smith, H. Wan, R. Mallipeddi, W.A. Griffiths, P. Dopping-Hepenstal, G.H. Ashton, R.A. Eady, W.H. McLean, and J.A. McGrath. 2002. Frameshift mutation in the V2 domain of human keratin 1 results in striate palmoplantar keratoderma. *J Invest Dermatol*. 118:838-844.

Willig, K.I., S.O. Rizzoli, V. Westphal, R. Jahn, and S.W. Hell. 2006. STED microscopy reveals that synaptotagmin remains clustered after synaptic vesicle exocytosis. *Nature*. 440:935-939.

Wilson, V.G. 2014. Growth and differentiation of HaCaT keratinocytes. *Methods Mol Biol*. 1195:33-41.

Windoffer, R., M. Beil, T.M. Magin, and R.E. Leube. 2011. Cytoskeleton in motion: the dynamics of keratin intermediate filaments in epithelia. *J Cell Biol*. 194:669-678.

Windoffer, R., M. Borchert-Stuhltrager, and R.E. Leube. 2002. Desmosomes: interconnected calcium-dependent structures of remarkable stability with significant integral membrane protein turnover. *J Cell Sci*. 115:1717-1732.

Wu, Y., P. Kanchanawong, and R. Zaidel-Bar. 2015. Actin-delimited adhesion-independent clustering of E-cadherin forms the nanoscale building blocks of adherens junctions. *Dev. Cell*. 32:139-154.

Xia, S., and P. Kanchanawong. 2017. Nanoscale mechanobiology of cell adhesions. *Semin. Cell Dev. Biol.*

Xu, T., V. Pagadala, and D.M. Mueller. 2015. Understanding structure, function, and mutations in the mitochondrial ATP synthase. *Microb Cell*. 2:105-125.

Yachdav, G., E. Kloppmann, L. Kajan, M. Hecht, T. Goldberg, T. Hamp, P. Honigschmid, A. Schafferhans, M. Roos, M. Bernhofer, L. Richter, H. Ashkenazy, M. Punta, A. Schlessinger, Y. Bromberg, R. Schneider, G. Vriend, C. Sander, N. Ben-Tal, and B. Rost. 2014. PredictProtein--an open resource for online prediction of protein structural and functional features. *Nucleic Acids Res*. 42:W337-343.

Yang, T.T., J. Su, W.J. Wang, B. Craige, G.B. Witman, M.F. Tsou, and J.C. Liao. 2015. Superresolution Pattern Recognition Reveals the Architectural Map of the Ciliary Transition Zone. *Sci Rep*. 5:14096.

Yano, T., H. Kanoh, A. Tamura, and S. Tsukita. 2017. Apical cytoskeletons and junctional complexes as a combined system in epithelial cell sheets. *Ann. N. Y. Acad. Sci.*

Yap, A.S., G.A. Gomez, and R.G. Parton. 2015. Adherens Junctions Revisualized: Organizing Cadherins as Nanoassemblies. *Dev. Cell*. 35:12-20.

Yin, L., and L.J. Stern. 2014. Measurement of Peptide Binding to MHC Class II Molecules by Fluorescence Polarization. *Curr Protoc Immunol*. 106:5 10 11-12.

Yin, T., S. Getsios, R. Caldelari, L.M. Godsel, A.P. Kowalczyk, E.J. Muller, and K.J. Green. 2005. Mechanisms of plakoglobin-dependent adhesion: desmosome-specific functions in assembly and regulation by epidermal growth factor receptor. *J Biol Chem*. 280:40355-40363.

Yin, T., and K.J. Green. 2004. Regulation of desmosome assembly and adhesion. *Semin Cell Dev Biol*. 15:665-677.

Yoon, Y., K.R. Pitts, and M.A. McNiven. 2001. Studying cytoskeletal dynamics in living cells using green fluorescent protein. *Methods Mol Biol*. 161:151-163.

York, A.G., S.H. Parekh, D.D. Nogare, R.S. Fischer, K. Temprine, M. Mione, A.B. Chitnis, C.A. Combs, and H. Shroff. 2012. Resolution doubling in live, multicellular organisms via multifocal structured illumination microscopy. *Nat. Methods*. 9:749-754.

Zhong, H. 2015. Applying superresolution localization-based microscopy to neurons. *Synapse*. 69:283-294.

Zhou, X.X., and M.Z. Lin. 2013. Photoswitchable fluorescent proteins: ten years of colorful chemistry and exciting applications. *Curr Opin Chem Biol*. 17:682-690.

Zihni, C., M.S. Balda, and K. Matter. 2014. Signalling at tight junctions during epithelial differentiation and microbial pathogenesis. *J. Cell Sci.* 127:3401-3413.